Tesis Doctoral

Simulación atomística de procesos heterogéneos en superficies

Sánchez, Verónica Muriel

2010

Universidad de Buenos Aires
Facultad de Ciencias Exactas y Naturales
Departamento de Química Inorgánica, Analítica y Química Física

Simulación atomística de procesos heterogéneos en superficies

Tesis presentada para optar al título de Doctor de la Universidad de Buenos Aires en el área Química Inorgánica, Química Analítica y Química Física

Verónica Muriel Sánchez

Director de tesis:
Dr. Damián A. Scherlis

Consejero de estudios:
Dr. Galo Soler Illia

Buenos Aires, 2010

Resumen

El propósito de esta tesis puede dividirse en dos incisos. Por un lado está enfocada en la caracterización de la adsorción y la reactividad sobre superficies de óxidos, tanto en interfases sólido-gas como sólido-líquido, a partir de un tratamiento computacional de primeros principios, basado en la teoría del funcional de la densidad (DFT) en el contexto de ondas planas y pseudopotenciales. Por otro lado, nuestro objetivo es desarrollar herramientas metodológicas en el marco de DFT, apropiadas para la descripción de materiales en entornos complejos, a fin de abordar una variedad de problemas en química y en ciencia de los materiales, tales como los considerados en esta tesis. Primeramente, hemos explorado diferencias de energía libre y barreras cinéticas involucradas en la disociación de agua y metanol sobre superficies de TiO_2 en fase gaseosa. Esto se ha llevado a cabo mediante la combinación de los métodos de *Umbrella Sampling* y de dinámica molecular de *Car-Parrinello*. En otra línea, hemos examinado la ionización de funciones aminopropilo en superficies de SiO_2 sustituidas, en el marco de una colaboración computacional-experimental para determinar el comportamiento ácido-base de materiales híbridos mesoporosos. Este análisis fue realizado tanto en fase gaseosa como en presencia de una bicapa de agua, para evaluar el efecto de una capa de hidratación en los resultados. Seguidamente, introducimos un modelo de solvente continuo diseñado para la realización de simulaciones de DFT en superficies de sólidos en contacto con una solución. Tal esquema—ideado en condiciones periódicas de contorno dentro del método de *Car-Parrinello*— es el primero que permite realizar dinámica molecular de primeros principios en la interfaz sólido-líquido. Esta metodología es utilizada a continuación para caracterizar los procesos de adsorción de moléculas pequeñas en la interfase TiO_2-agua. Una via alternativa para la descripción del entorno en las simulaciones de estructura electrónica es la metodología híbrida de Mecánica Cuántica-Mecánica Clásica (conocida por las siglas QM-MM), en la cual un número limitado de átomos (el soluto) es tratado mediante mecánica cuántica, mientras que el resto del sistema (el solvente) se describe usando un campo de fuerzas clásico. Esta técnica está ampliamente difundida en aplicaciones en química relacionadas con moléculas o sistemas finitos. En esta tesis introducimos una formulación híbrida QM-MM en condiciones periódicas de contorno, concebida para la simulación de sistemas extendidos

Palabras claves: DFT, superficie de titania, QM-MM, modelo de solvente continuo, PPW, Car Parrinello, Umbrella Sampling, simulación computacional, superficie de sílica

Abstract

The purpose of this thesis is twofold: on one hand, it is aimed to characterize adsorption and reactivity on oxide surfaces both at the solid-gas and solid-liquid interfaces, from a first-principles computational standpoint, based in density functional theory (DFT) in a plane waves-pseudopotential setting. On the other hand, our objective is to develop methodological tools in a DFT framework, appropriate to describe materials in complex environments, to address a variety of problems in chemistry and materials science, such as those considered in this thesis. Firstly, we explore the free energy differences and kinetic barriers involved in the dissociation of water and methanol at TiO_2 surfaces in the gas phase. This is achieved through the combination of the Umbrella Sampling technique and the Car-Parrinello molecular dynamics method. In a different line, we examine the ionization of aminopropyl functions in substituted SiO_2 surfaces, in the context of an experimental-computational collaboration to determine the acid-base behavior of hybrid mesoporous materials. This is done both in the gas phase and in the presence of a water bilayer, to assess the effect of an hydration shell in the results. Next, we present a continuum solvent model designed to perform DFT simulations at solid surfaces in contact with a solution. Such scheme—devised in periodic boundary conditions within the Car-Parrinello method—is the first one to allow for ab-initio molecular dynamics at solid-liquid interfaces. This methodology is then applied to characterize the adsorption processes of small molecules at the TiO_2-water interface. An alternative pathway to describe the environment in electronic structure calculations is the hybrid Quantum Mechanics-Molecular Mechanics (QM-MM) methodology, in which a limited number of atoms (the solute) are treated quantum-mechanically, whereas the rest of the system (the solvent) is described using classical force-fields. This technique is widespread in chemistry applications for molecules or finite systems: in this thesis we introduce a QM-MM formulation in periodic boundary conditions, conceived for the simulation of extended systems.

Keywords: DFT, titania surface, QM-MM, continuum solvent model, PPW, Car-Parrinello, Umbrella Sampling, computer simulation, silica surface

Contents

Chapter 1
Introduction

Molecular simulation techniques constitute a valuable research tool to complement experimental observations, but also to predict physical properties and chemical reactivity under specific conditions with a degree of detail that experiments are sometimes unable to provide. On the other hand, and generally speaking, experimental conditions involve complex situations and environments, while theoretical models tend to describe simpler systems under a number of assumptions. It is essential to be well aware of these simplifications and assumptions, by the time of interpreting and assessing the reach and the limitations of the results coming from simulations. In particular, this thesis is centered on the chemical behavior of small molecules on oxide surfaces from an atomistic perspective.

There is a great amount of computational work addressing adsorption and reactivity on oxide surfaces in the gas phase. However, many of the relevant applications of oxide materials are related to heterogeneous catalysis, where the chemical reactions occur at the solid-liquid interface. The thermodynamic feasibility of these processes strongly depends on the medium, which affects the energetic balance between the products, reactants and intermediates. In the present work we consider the inclusion of the solvent in the simulation through different approaches.

Molecular simulation studies can be performed through different theories, the choice of which depends on the type of answer that is sought. This thesis is focused on surface chemistry and reactivity, which implies the transformation of a molecular entity into another one. Quantum mechanics (QM) is the theory that adequately characterizes the cleavage and formation of atomic bonds. Among the available molecular simulation methods, QM simulations (also called simulations from first-principles) are the most detailed, and consequently the computationally most demanding. In particular, we employ techniques based on density functional theory (DFT), which is today the first choice for first-principles simulations of systems comprising from a few tens up to a few hundred of atoms, because of its excellent balance between efficiency and accuracy. We utilize this methodology to study adsorption energies and configuration of small molecules upon surfaces, and also dissociation free energy profiles and finite temperature dynamics.

In many occassions the reactive processes are circumscribed to only a few atoms, surrounded by a larger matrix or environment which does not experience directly any breaking or formation of chemical bonds. In such cases, it may not be necessary to apply the QM description to the whole system, considering instead a partition in two regions, each one described at a different level of theory, but still keeping the interaction between them. By mixing these different degrees of accuracy in the description, it is possible to represent more complex environments without dramatically increasing the computational cost. In this line of thought, this thesis considers two different approaches to address solid-liquid interfaces: the continuum solvent model, and the hybrid QM-MM methodology. Before going into any detail regarding these approaches, we notice that solid-liquid interfaces are complex systems very appropriate to be divided in two regions, according to the kind of partitioning proposed above. The QM level of description must be applied to the surface atoms as well as to the molecules immersed in the liquid phase that interact directly with the surface. The rest of the system: all or most of the solvent molecules, and sometimes the atoms at deeper layers of the solid, can be characterized at a less expensive level.

The first of these approaches discussed and implemented in this thesis is the continuum solvent model, which represents the liquid phase as a continuum dielectric medium. Within this scheme the characterization of the liquid phase is considered from a macroscopical standpoint: the average solvation effect is captured by the model, but at the same time specific solute-solvent interactions and the structure of the solvent are neglected. The second approach considered is the hybrid QM-MM methodology, which combines molecular mechanics (consisting in a classical force field) and quantum mechanics. Within this approach, the QM and the MM subsystem are usually called the solute and the solvent, respectively.

While the discussion up to this point has considered surfaces in general, this thesis is mainly focused on titania and silica surfaces. Both titania and silica have a high scientific and technological impact. Titania surfaces are often found in a crystalline phase, while the amorphous phase is the most usual for silica. From the point of view of quantum-mechanics simulations in periodic boundary conditions, crystalline structures are easier to recreate than amorphous phases. The strategy followed to represent the silica surface is discussed in subsection 1.3. The adsorption and reactivity at these interfaces is studied here for a variety of small molecules and moieties, including water, hydroxide, methanol, hydrogen peroxide, carboxylic acid and the aminopropyl group.

1.1 The study of surfaces with DFT

Density functional theoretical studies constitute an important approach to describe solids and surfaces. Electronic structure simulations of surfaces have been carried out using both finite and extended models. In the former case, localized basis sets methods are employed, and surfaces are represented by a cluster of atoms, hopefully big enough to minimize the finite size effects. On the other hand, extended models require the use of methods in periodic boundary conditions, based on pseudopotentials and delocalized basis functions, typically plane waves. We consider this is the most natural and realistic approach to address periodic surfaces and materials, and therefore this is the path adopted in the present thesis. The fundamentals of the DFT methodology for extended systems is explained in detail in Chapter 2. In the following, we will give a brief glimpse on what are the models used in the context of electronic structure methods for surfaces in periodic boundary conditions. Crystalline solids and surfaces are extended systems periodically repeated in three dimensions (3D) and in two dimensions (2D), respectively. Only one unit cell is needed to characterize the system in the simulation. The mathematical formalism in periodic boundary conditions naturally produces the unit cell replication along the three directions. Since the method imposes periodicity in all axis, [1] in order to model a surface it is necessary to leave an empty space in between the structure and its periodic images along one of the directions (conventionally the z-axis, which is the one perpendicular to the surface). The model generated in this way is called a slab: it is infinite in its x and y dimensions, and exposes two faces perpendicular to the z-axis. Computational experiments like relaxations, reconstructions, or adsorption, can be done on any of these faces, or in both at the same time. The thickness of the slab is chosen so that geometrical and energetic properties, in particular the surface energy, are converged. Usually, four or five atomic layers are enough to reproduce the properties of the semi-infinite surface [1,2]. The atoms of the inner layers are frozen to their bulk positions, and the two or three outer layers are optimized.

Internal energy vs free energy

The system reactivity is extremely conditioned by temperature. The vast majority of electronic structure simulations, and in particular almost all DFT calculations of surfaces, explore adsorption and dissociation energies of optimized, equilibrium structures at zero temperature. Results of energetics at 0 K are usually taken to determine the stability or the thermodinamically favored species at room temperature, because the calculation of

[1] The mixing of periodic with non-periodic boundary conditions in different axis in electronic structure calculations would involve a complex formulation and is not usual.

reaction free energies requires first principles, expensive molecular dynamics simulations, in combination with a statistical sampling scheme. The *Car-Parrinello* molecular dynamics approach [3], to be introduced in Chapter 2, has helped significantly to the realization of finite temperature simulations of extended systems. In this thesis we investigate the free energy dissociation profiles of water and methanol on the clean surfaces of anatase(101) and rutile(110). To this end, we combine *Car-Parrinello* molecular dynamics simulations with the *umbrella sampling* [4] methodology. These results are presented in Chapter 3.

1.2 Scientific relevance and modelling of titanium dioxide

For many reasons, titanium dioxide (TiO_2) surfaces are among the most widely studied to date. This material has found applications in heterogeneous catalysis, coatings, solar cells, sensors, and, more recently, the design of biomaterials [5–8]. Its use in photo-assisted degradation of organic molecules to O_2 and H_2O has arised a lot of interest for purification or desinfection of wastewater [9, 10]. TiO_2 and silica (SiO_2) constitute the typical precursors used in the soft sol-gel synthesis technique, for the preparation of thin films and mesoporous materials [11–14]. Furthermore, TiO_2 is inexpensive and undefective faces are relatively easy to prepare, which has made of it a prototype oxide in surface science research.

Up to date, there exists a number of experimental techniques capable to provide information concerning the atomic and electronic structure of a surface, including the type of adsorption of a given species at the interface and the surface site where this adsorption takes place. Some of these techniques are: temperature programmed desorption (TPD), x-ray photoelectron spectroscopy (XPS), Low Energy Electron Difraction (LEED), scanning tunnelling microscopy (STM), atomic force microscopy (AFM), among others [15]. Crystalline and amorphous titania surfaces have been analyzed with these methods, which have revealed the nanostructure of the surface, and the configurations of molecules and atoms adsorbed on them [5,16–20]. The majority of these techniques operate in conditions of high or ultrahigh vacuum. First-principles simulations, in particular density functional theory calculations [21, 22], have played a crucial role to complement and interpret the data from experiments in vacuum. The microscopic insight provided by atomistic simulations has shed light on the structure and reactivity of solids and surfaces, explaining some experimental results as well as predicting others [5, 7, 16, 20, 23].

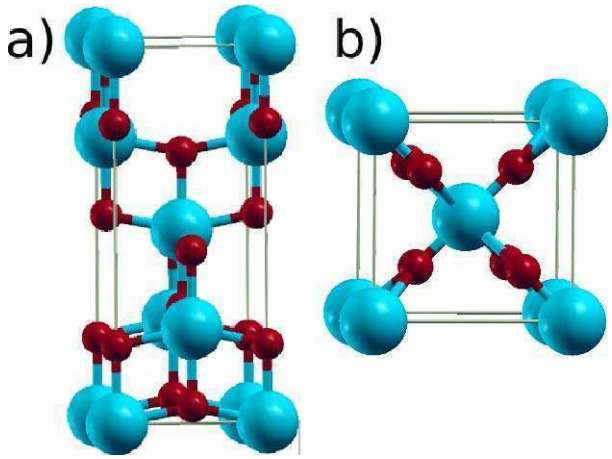

Figure 1.1. Unit cell corresponding to a)anatase and b)rutile bulk structures.

Bulk description

There are three different crystalline phases of titanium dioxide, with the corresponding crystal structures: brookite(rhombohedrical, D_{2h}^{15}-Pbca, a = 5.436 Å, b = 9.166 Å, c = 5.135 Å), anatase (tetragonal, D_{4h}^{19}-I4/amd, a = b = 3.782 Å, c = 9.502 Å) [24] and rutile(tetragonal, D_{4h}^{14}-$P4_2$/mnm, a = b = 4.584 Å, c = 2.953 Å) [25]. Anatase and rutile are the thermodinamically most stable [26], and as a consequence they have been the most exhaustively studied. One and the other are also investigated along this thesis. Figure 1.1 shows the crystal structures for anatase and rutile.

It can be seen from figure 1.1 that, in both crystals, every titanium atom is inside a octahedrical hole, exhibiting a coordination number of six. This Ti atom is sometimes denoted as Ti(6c). On the other hand, oxygen is coordinated to three neighbors, and so is known as O(3c). Before proceeding with surface calculations, the description for anatase and rutile must reproduce the bulk experimental parameters. The pseudopotential plane waves method is applied to perform the simulations of this thesis, in particular the *Quantum Espresso* implementation [27] with *ultrasoft* pseudopotentials [28] and the PW91 exchange correlation functional [29, 30]. This functional has widely proved to correctly describe energy and structure of titanium dioxide [16, 31–33]. The simulation parameters mentioned above have been applied to the computations throughout this thesis; the meaning of each one will be explained in Chapter 2. In our simulations the unit cell parameters are fixed to experimental values, whereas the optimized Ti-O bond distances were checked to reproduce experiments.

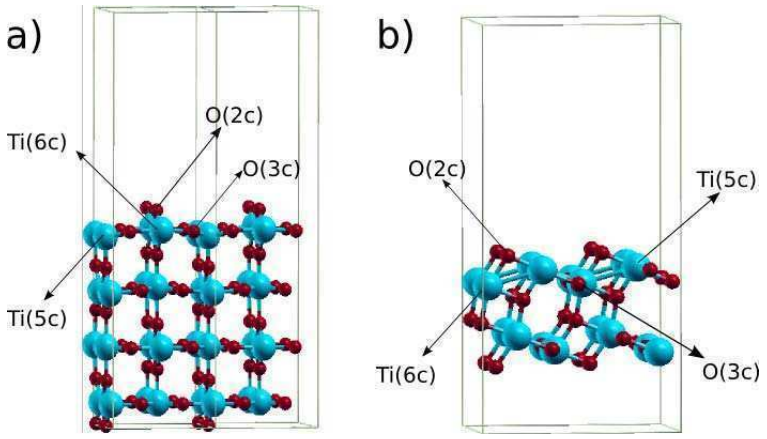

Figure 1.2. Slab models for the a) rutile (110) and b) anatase(101) surfaces, four layers deep.

Surface description

The bulk structure can be cut along different planes, leaving in each case two surfaces as a product. The resulting faces are named according to their relative orientation; Miller indices are used to name planes as well as the corresponding surfaces. For each polymorph there is one particular face involving the lowest surface energy, i.e., the most stable: experiments and calculations indicate that the (101) and (110) surfaces are the most stable for anatase and rutile, respectively [1, 2, 5, 7, 34–36].

Due to the different environment of the surface atoms respect to the bulk, these atoms usually experience some displacements to minimize the surface energy. This process is called relaxation, or reconstruction when it is accompanied by a redistribution of chemical bonds. For the previously mentioned surfaces, reconstruction is not observed, and surfaces can be represented by a minimal structure with the same pattern as the bulk unit cell, identified with the label (1x1) [5, 7, 37].

Rutile(110) and Anatase(101)

It can be seen from figure 1.2 that these surfaces exhibit two new types of atoms: Ti(5c), which is the five-coordinated, exposed titanium atom, and O(2c), usually called bridge oxygen, because it connects two Ti atoms on the surface. Both Ti(5c) and O(2c) appear as a consequence of breaking one Ti-O bond. The insaturated valence enhances reactivity on these sites, aside from causing inward and upward relaxations of the atomic positions with respect to the bulk [5, 7], to minimize the surface energy; these changes in the atomic positions are usually small, and in our calculations they were checked to be in agreement with experiments and previous simulations.

Slabs between three and seven layers have been employed to model the rutile (110)

surface [1,32,34,38,39], while the anatase (101) slab is most often built with four atomic layers [40–44]. In figure 1.2 the anatase (101) surface is represented by a (2 $\times$ 2) slab four layers deep, whereas in the case of rutile (110), a (2 $\times$ 1) surface made of four layers of atoms is shown. The supercell dimensions are 7.55 $\times$ 10.20 $\times$ 22.00 Å^3 for anatase and 6.01 $\times$ 6.48 $\times$ 24.00 Å^3 for rutile, both of them containing a total of 48 atoms [2].

Insaturated coordination of the surface atoms not only enhances surface reactivity, but also promotes the presence of defects. One of the most common deffects on titanium dioxide surfaces are a consequence of a missing O(2c) atom [5, 39, 45–47]. These are called reduced surfaces.

1.3 Modelling of silica systems

Silica constitutes one of the most common mineral materials on earth. It is used as the raw material for countless products: from all kind of commodities as desiccants, glasses, ceramics and cement, to elaborated technological articles as optical fibers and dielectrics for microelectronic devices. More specifically, applications of SiO_2 in the chemical sciences include catalysts, chemical separators, and more recently the preparation of mesoporous inorganic materials [12,13,48,49]. The flexibility of the Si-O-Si bond explains the wide variety of existing polymorphs, including quartz, cristobalite and diatomite. However, silica is generally found as an amorphous system [50].

Silica became a subject of this thesis as a result of a collaboration with a group of experimentalists working in materials synthesis and characterization [51] (see Chapter 4). Computer simulation was applied to the investigation of the acid-base equilibrium in aminopropyl functions decorating the walls of mesoporous silica and titania. To address this problem, a proper representation of the surface has to be considered. The formation of silica surfaces involves the cleavage of the Si-O bond, which, in the presence of water, leads to silanol (-Si-OH) surface groups [52]. Silanol moieties can be detected in spectroscopic experiments via the Si–OH stretching mode around 3750 cm$^-1$ [53, 54], and may be classified in two types: simple (or terminal) and geminal, denoting respectively one and two hydroxyl groups attached to a Si surface atom. The density and type of these -Si-OH groups determine most properties and reactivity of silica surfaces, therefore, model structures adopted in simulations attempt to recreate these parameters.

As it was mentioned before, silica is usually found in an amorphous phase, whose representation by simulation techniques is not straightforward. Amorphous materials are extended systems with no periodic arrangement and therefore pose a challenge to simula-

[2]Even though these surfaces can be represented by a (1x1) cell, we adopt larger supercells compatible with Γ point sampling, and to reduce lateral interactions between adsorbates and their images.

tions in both finite and periodic frameworks. Non-periodic studies with localized basis sets were carried out in small silica clusters in order to understand reactivity and the formation of silanol groups [55]. Hybrid QM-MM methods were also employed in finite models [56]. On the other hand, there are two strategies to solve this problem using a periodic approach: (1) to simulate the system including a huge number of atoms in the unit cell, so that periodicity effects are minimized, or (2) to find a proper crystal face which recreates the most important features of the amorphous surface.

The first strategy is the most accurate—providing the unit cell is large enough—but more demanding, not always within reach of first-principles calculations. A few examples of calculations on amorphous silica models in periodic boundary conditions can be found in the recent literature, in which unit cells containing around 100-120 atoms were adopted to describe the hydroxylated surface [50, 57]. Simulations of much larger amorphous structures have been performed with molecular mechanics approaches, computationally less demanding, but not able to explore reactivity [58–60].

In the second approach, the amorphous phase is replaced by a crystaline structure exhibiting similar surface properties. The β-cristobalite phase has been chosen in several ab initio studies [61–64], because the silanol density and the refractive index are similar to those present in amorphous silica. In particular, terminal silanols are well represented by the β-cristobalite (111) surface [61, 63–65], while the geminal silanols are characteristic of the (100) surface [63]. Terminal silanols account for the major part of the substituted Si atoms at the surface, and therefore the (111) face has been the most usual choice to represent the amorphous structure in DFT calculations in periodic boundary conditions [61,63–65]. In view of these results, in this thesis the amorphous silica is modelled through the β-cristobalite (111) surface. A model for this structure is shown in figure 1.3. The β-cristobalite (111) is represented by a (2 x 2) slab four layers deep, and supercell dimensions of $8.74 \times 10.08 \times 37.14$ Å^3 containing a total of 60 atoms.

1.4 Solid-liquid interfaces

The majority of the computational research cited up to this point, refers to calculations at the solid-gas interface. However, a broad range of titania (and silica) applications related to heterogeneous catalysis and electrochemistry involve the solid-liquid interfaces. The explicit inclusion of the solvent into the simulation scheme dramatically increases the cost of first-principles calculations of periodic surfaces. This implies to fill the vacuum space with a large amount of water molecules (or any other solvent) to represent the bulk liquid phase. Yet, to get a realistic description of the fluid, it is necessary to perform long molecular dynamics or extensive Monte-Carlo simulations in which the system visits all

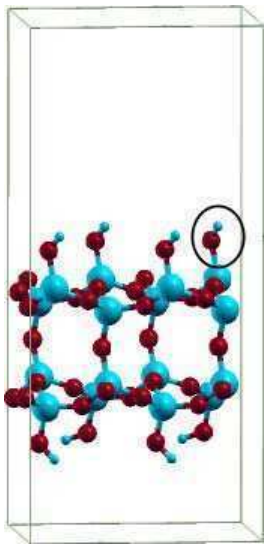

Figure 1.3. Model structure of the SiO_2 β-cristobalite (111) surface. The slab is four SiO_2 layers deep. A terminal silanol group is enclosed in a black trace.

configurations characterizing the liquid phase [66]. Given the high computational cost, this strategy is not very usual.

It is then desirable to have alternative computational approaches specially designed to perform calculations and obtain thermodynamic data at the solid-liquid interface. The need for reliable computational approaches to explore surfaces in contact with a solution becomes even more urgent when many surface techiques capable to provide atomistic information, such as XPS or surface-difraction methods (LEED) [15], are only operative under high vacuum conditions. Alternatives to the explicit solvation are the continuum (or implicit) solvent models [67, 68], in which the solvent is introduced in the simulation scheme in the form of a continuum dielectric medium represented by a permittivity function. This function takes the value of 1 (corresponding to vacuum) inside the molecule or surface, and the value of the dielectric constant of the solvent outside. This transition between the vacuum and the bulk solvent dielectric can occur smoothly [69] or abruptly [70]. Continuum models incorporate the solvent polarization effects in an average fashion, the cost of the computation becoming closer to the corresponding cost in vacuum. On the other hand, the representation of the solvent structure is omitted, disregarding any possible solute-solvent specific interactions. Still, to overcome this problem, all or part of the first solvation shells can be included explicitly; within this scheme the dielectric medium extends beyond the limits of a cluster composed by the solute plus a few solvent molecules.

The continuum model has a long tradition in quantum chemistry, and has proved to be reliable and efficient to extract properties of a large variety of molecular systems in solution [66–68]. The application of this methodology to extended systems, and in particular

to solid-liquid interfaces, has been much less common. In this thesis we develop a continuum solvent method within the Car-Parrinello approach and the pseudopotential plane waves method, to perform first-principles molecular dynamics at surfaces in contact with a solution. This implementation is presented in Chapter 5, and in the following chapter it is used to understand the interaction between small molecules and titania at the solid-water interface.

As mentioned at the openning paragraphs of the present chapter, another way to get around the high computational cost of QM calculations with explicit solvation, is to divide the system into two regions, described respectively with QM and MM Hamiltonians. A significant efficiency gain can be achieved if the solvent molecules are treated at the MM level. While this kind of hybrid methodologies has been extensively applied to molecular and biomolecular systems, adaptations involving plane waves DFT codes capable to deal with surfaces or solids in fully periodic boundary conditions for the QM and the MM parts have not been reported. The first stage in the implementation of this technique is exposed in Chapter 7.

References

[1] S. Bates, G. Kresse, and M. Gillan, *Surf. Sci.* 385, (1997), 386–394.

[2] M. Lazzeri, A. Vittadini, and A. Selloni, *Phys. Rev. B* 63, (2001), 155409.

[3] R. Car and M. Parrinello, *Phys. Rev. B* 55, (1985), 2471–2474.

[4] J. P. Torrie, G.and Valleau, *J. Comput. Phys.* 23, (1977), 187.

[5] U. Diebold, *Surf. Sci. Rep.* 48, (2003), 53–229.

[6] M. A. Henderson, *Surf. Sci. Rep.* 46, (2005), 1.

[7] C. L. Pang, R. Lindsay, and G. Thornton, *Chem. Soc. Rev.* 37, (2008), 2328–2353.

[8] F. H. Jones, *Surf. Sci. Rep.* 42, (2001), 75.

[9] A. Mills, H. Dabvies, and D. Worsley, *Chem. Soc. Rev.* 22, (1993), 417.

[10] P.-C. Maness, S. Smolinski, and W. Jacoby, *Appl. Environ. Microbiol.* 65, (1999), 4094.

[11] C. J. Brinker and G. W. Scherrer, *Sol-Gel Science, The Physics and Chemistry of Sol-Gel Processing*, Academic Press, San-Diego, CA, 1990 (**1990**).

[12] M. H. Lim, C. F. Blanford, and A. Stein, *J. Am. Chem. Soc.* 119, (1997), 4090–4091.

[13] G. J. de A. A. Soler-Illia, C. Sanchez, B. Lebeau, and J. Patarin, *Chem. Rev.* 102, (2002), 4093–4138.

[14] P. C. Angelomé and G. J. de A. A. Soler-Illia, *Chem. Mater. 2005, 17, 322-331* 17, (2005), 322–331.

[15] J. C. Vickerman, *Surface Analysis - The principal Techniques*, John Wiley & Sons (**2005**).

[16] R. Schaub, P. Thostrup, N. Lopez, E. Lægsgaard, I. Stensgaard, J. K. Nørskov, and F. Besenbacher, *Phys. Rev. Lett.* 87, (2001), 266104.

[17] F. P. Rotzinger, J. M. Kesselman-Truttmann, S. J. Hug, V. Shklover, and M. Grätzel, *J. Phys. Chem. B* 108, (2004), 5004–5017.

[18] C. yi Wang, H. Groenzin, and M. J. Shultz, *J. Am. Chem. Soc.* 127, (2005), 9736–9744.

[19] T. Hirakawa, K. Sato, A. Komano, S. Kishi, C. K. Nishimoto, N. Mera, M. Kugishima, T. Sano, H. Ichinose, N. Negishi, Y. Seto, and K. Takeuchi, *J. Phys. Chem. C* 114, (2010), 2305–2314.

[20] G. U. Rakhmatkariev, A. J. P. Carvalho, and J. P. P. Ramalho, *Langmuir* 23, (2007), 7555–7561.

[21] P. Hohenberg and W. Kohn, *Phys. Rev.* 136, (1964), 864.

[22] W. Kohn and L. J. Sham, *Phys. Rev.* 140, (1965), 1133.

[23] J.-H. Wang and M. C. Lin, *J. Phys. Chem. B,* 109, (2005), 5133–5142.

[24] G. V. Samsonov, *The Oxide Handbook*, IFI/Plenum Press, New York (**1982**).

[25] F. A. Grant, *Rev. Mod. Phys.* 31, (1959), 646.

[26] S.-D. Mo and W. Y. Ching, *Phys. Rev. B* 51, (1995), 13023.

[27] P. Giannozzi, S. Baroni, N. Bonini, M. Calandra, R. Car, C. Cavazzoni, D. Ceresoli, G. L. Chiarotti, M. Cococcioni, I. Dabo, A. D. Corso, S. de Gironcoli, S. Fabris, G. Fratesi, R. Gebauer, U. Gerstmann, C. Gougoussis, A. Kokalj, M. Lazzeri, L. Martin-Samos, N. Marzari, F. Mauri, R. Mazzarello, S. Paolini, A. Pasquarello, L. Paulatto, C. Sbraccia, S. Scandolo, G. Sclauzero, A. P. Seitsonen, A. Smogunov, P. Umari, and R. M. Wentzcovitch, *J. Phys.: Condens. Matter* 21, (2009), 395502.

[28] D. Vanderbilt, *Phys. Rev. B* 41, (1990), 7892–7895.

[29] J. P. Perdew and Y. Wang, *Phys. Rev. B* 45, (1992), 13244.

[30] J. P. Perdew and et al, *Phys. Rev. B* 46, (1992), 6671.

[31] K. M. Glassford and J. R. Chelikowsky, *Phys. Rev. B* 46, (1992), 1284.

[32] L. A. Harris and A. A. Quong, *Phys. Rev. Lett.* 93, (2004), 086105.

[33] J. Goniakowski, J. M. Holender, L. N. Kantorovich, M. J. Gillan, and J. A. White, *Phys. Rev. B* 53, (1996), 957.

[34] M. Ramamoorthy and D. Vanderbilt, *Phys. Rev. B* 49, (1994), 16721.

[35] G. E. Brown, V. E. Henrich, W. H. Casey, D. L. Clark, C. Eggleston, A. Felmy, D. W. Goodman, M. Grätzel, G. Maciel, M. I. McCarthy, K. H. Nealson, D. A. Sverjensky, M. F. Toney, and J. M. Zachara, *Chem. Rev.* 99, (1999), 77–174.

[36] A. Vittadini, M. Casarin, and A. Selloni, *Theor Chem Acc* 117, (2007), 663–671.

[37] R. Hengerer, B. Bollinger, and M. Erbudak, *Surf. Sci.* 460, (2000), 162.

[38] R. Sanchez de Armas, J. Oviedo, M. A. S. Miguel, and J. F. Sanz, *J. Phys. Chem. C* 111, (2007), 10023–10028.

[39] J. Oviedo, R. S. de Armas, M. A. S. Miguel, and J. F. Sanz, *Phys. Chem. C Lett.* 112, (2008), 17737–17740.

[40] A. Tilocca and A. Selloni, *J. Phys. Chem. B* 108, (2004), 4743.

[41] A. Tilocca and A. Selloni, *Langmuir* 20, (2004), 8379.

[42] A. Vittadini, A. Selloni, F. Rotzinger, and M. Grätzel, *Phys. Rev. Lett.* 81, (1998), 2954.

[43] A. Tilocca and A. Selloni, *J. Phys. Chem. B* 108, (2004), 19314.

[44] A. Vittadini, A. Selloni, F. Rotzinger, and M. Gratzel, *J. Phys. Chem. B* 104, (2000), 1300.

[45] A. Tilocca and A. Selloni, *J. Chem. Phys.* 119, (2003), 7445.

[46] M. A. Henderson, *Surf. Sci.* 355, (1996), 151.

[47] U. Diebold, J. Lehman, T. Mahmoud, M. Kuhn, G. Leonardelli, W. Hebenstreit, M. Schmid, and P. Varga, *Surf. Sci.* 411, (1998), 137.

[48] M. Davis, *Nature* 417, (2002), 813.

[49] T. Bakos, S. N. Rashkeev, and S. T. Pantelides, *Phys. Rev. Lett.* 88, (2002), 055508.

[50] F. Tielens, C. Gervais, J. F. Lambert, F. Mauri, and D. Costa, *Chem. Mater.* .

[51] A. Calvo, P. C. Angelomé, V. M. Sánchez, D. A. Scherlis, F. J. Williams, and G. J. A. A. Soler-Illia, *Chem. Mater.* 20, (2008), 4661–4668.

[52] L. T. Zhuravlev, *Langmuir* 3, (1987), 316.

[53] P. R. Ryason and B. G. Russell, *J. Phys. Chem.* 79, (1975), 1276.

[54] B. A. Morrow and A. J. McFarlan, *J. Non-Cryst. Solids* 120, (1990), 61.

[55] A. G. Pelmenschikov, G. Morosi, and A. Gamba, *J. Phys. Chem. A* 101, (1997), 1178–1187.

[56] M.-H. Du, A. Kolchin, and H.-P. Cheng, *J. Chem. Phys.* 119, (2003), 6418.

[57] Mischler, *J. Phys.: Condens. Matter* 17, (2005), 4005.

[58] S. H. Feuston, B. P. abd Garofalini, *J. Appl. Phys.* 68, (1990), 4830.

[59] K. Shirono and H. Daiguji, *J. Phys. Chem. C* 111, (2007), 7938–7946.

[60] R. Mancinelli, S. Imberti, A. K. Soper, K. H. Liu, C. Y. Mou, F. Bruni, and M. A. Ricci, *J. Phys. Chem. B,* 113, (2009), 16169–16177.

[61] F. Liu, S. H. Garofalini, R. D. King-Smith, and D. Varderbilt, *Phys. Rev. Lett.* 70, (1993), 2750.

[62] I.-S. Chuang and G. E. Maciel, *J. Phys. Chem. B* 101, (1997), 3052.

[63] S. Iarlori, D. Ceresoli, M. Bernasconi, D. Donadio, and M. Parrinello, *J. Phys. Chem. B* 105, (2001), 8007–8013.

[64] D. Jiang, B. Sumpter, and S. Dai, *Langmuir* 22, (2006), 5716–5722.

[65] D. Ceresoli, M. Bernasconi, S. Iarlori, M. Parrinello, and E. Tosatti, *Phys. Rev. Lett.* 84, (2000), 3787.

[66] C. J. Cramer and D. G. Truhlar, *Chem. Rev.* 99, (1999), 2161.

[67] I. N. Levine, *Química Cuántica*, Pearson Educación (**2001**).

[68] J. Tomasi, B. Mennucci, and R. Cammi, *Chem. Rev.* 105, (2005), 2999.

[69] D. A. Scherlis, J.-L. Fattebert, F. Gygi, M. Cococcioni, and N. Marzari, *J. Chem. Phys.* 124, (2006), 074103.

[70] S. Miertusˇ, E. Scrocco, and J. Tomasi, *J. Chem. Phys.* 55, (1981), 117.

Chapter 2
Methodological background

To simulate a chemical system the first thing to do is to select a proper way to describe it. In general, there are two ways to address the atomistic simulation of a molecular system: one that describes the rupture and formation of chemical bonds, where the electronic structure changes significantly, and another one used to study processes where no chemical bond is modified. The first has necessarily to deal with the quantum mechanical side of the system, in particular with the electrons, and is known as electronic structure methodology, whereas the second one treats the atoms as classical particles and is known as classical methodology.

There is also a third type of methodology known as hybrid quantum mechanics-molecular mechanics (QM-MM) where the system is divided in two regions, one of them described by quantum mechanics (QM) and the other one by molecular mechanics (MM). Both regions interact with each other throughout a proper Hamiltonian. This approach will be explained in detail in chapter 7.

2.1 Electronic structure methods

To study the physics of small particles, such as electrons, we need to resort to quantum mechanical theory. This theory establishes that every system can be described by a wave function, which contains all the information of the system. The wave function obeys the time dependent Schrödinger equation [1]:

$$i\hbar\frac{\partial\Psi\left(r,t\right)}{\partial t}=-\frac{\hbar^{2}}{2m}\nabla^{2}\Psi\left(r,t\right)+V\left(r,t\right)\Psi\left(r,t\right) \tag{2.1}$$

Ψ is the wave function for a particle which depends on position r and time t, m is the mass of the particle, ∇^2 is the Laplacian operator, $\hbar$ is the Planck constant divided by 2π, and $V\left(r,t\right)$ is the external potential.

If the external potential does not depend on time, this equation can be rewritten as:

$$E\Psi\left(r\right) = -\frac{\hbar^2}{2m}\nabla^2\Psi\left(r\right) + V\left(r\right)\Psi\left(r\right) \tag{2.2}$$

By the definition of the following Hamiltonian operator:

$$\hat{H} = -\frac{\hbar^2}{2m}\nabla^2 + V\left(r\right) \tag{2.3}$$

equation 2.2 can be written as:

$$\hat{H}\psi\left(r\right) = E\psi\left(r\right) \tag{2.4}$$

To solve this equation for a system of electrons and nuclei, firstly we need to define precisely the Hamiltonian operator. In order to simplify the problem, the *Born-Oppenheimer approximation* is generally adopted, which consists in decoupling the electron movement from that of the nuclei, considering that the mass of the proton is three orders of magnitude larger than the electron mass. Within the Born-Oppenheimer approximation the electrons adapt instantaneously to the coordinates of the nuclei, and the Hamiltonian can be described as: $\hat{H} = \hat{H}_{el} + \hat{H}_{nucl}$. In this way, $\hat{H}_{el}$ depends only parametrically on the coordinates of the nuclei. From now on, we will neglect the kinetic energy of the nuclei, and hence, for a set of N electrons in the field of M nuclei, $\hat{H}$ expressed in atomic units assumes the following form:

$$\hat{H} = -\sum_{i=1}^{N}\frac{\nabla_i^2}{2} - \sum_{i=1}^{N}\sum_{A=1}^{M}\frac{Z_A}{r_{iA}} + \sum_{i=1}^{N}\sum_{j>i}^{N}\frac{1}{r_{ij}} + \sum_{A=1}^{M}\sum_{B>A}^{M}\frac{Z_A Z_B}{R_{AB}} \tag{2.5}$$

The first term stands for the kinetic energy N electrons, the second one represents the attraction between nuclei and electrons, the third one the repulsion between electrons, and the last one the repulsion between nuclei. Even though the exact expression for the Hamiltonian can be written as pointed above, the Schrödinger equation can not be solved analytically for systems with more than one electron. To find the solution for many electrons systems, a number of approximations aside from Born-Oppenheimer's are needed. Depending on the type of approximations employed to solve the Schrödinger equation, different electronic structure methodologies have been developed ever since the consolidation of quantum mechanics. These can be divided in three groups: semiempirical, *ab initio*, and methods based on density functional theory (DFT), which are the ones employed in this thesis. An important tool to find the wave-function of the system in the context of any of these electronic structure methods is the variational principle. In particular, the variational method is usually employed to solve the DFT equations, and therefore it is going to

be explained next.

Variational method The variational theorem states that, given an approximate wave function ϕ, the ground state energy of the system E_0 verifies the following relation [1]:

$$W = \frac{\left\langle \phi \left| \hat{H} \right| \phi \right\rangle}{\langle \phi | \phi \rangle} \geq E_0 \tag{2.6}$$

When the wave-function is the exact solution to the corresponding Schrödinger equation (or, what is the same, the Hamiltonian eigenfunction) the equality arises. The more alike the approximate wave function is to the eigenfunction of $\hat{H}$, the lower the value of W. Thereafter, a strategy to find an approximate wave-function is to minimize a trial function by minimizing W. This procedure is known as the variational method.

2.1.1 *Ab initio* methods

The *ab initio* methods, also called from first principles,[1] are based only on quantum mechanics and universal constant, without resorting to any empirical assumptions or additional experimental information in the form of parameters.

Historically, the first methodology developed to compute the energies of atoms and molecules with chemical accuracy is the Hartree-Fock (HF) method [1,2]. It has settled the basis for a wide range of electronic structure methods, including density functional theory in its present format, and for that reason it is briefly discussed in this section. Hartee-Fock was preceded by the Hartree or orbital approximation, where the many electrons wavefunction of N particles is approximated as a product of one-electron functions:

$$\Psi(r_1, \ldots, r_N) = \varphi_1(r_1) \ldots \varphi_N(r_N) \tag{2.7}$$

Here φ_n are one electron spin-orbital functions and r_i are the spatial coordinates for each electron i. These spin-orbitals do not have a direct physical meaning, but the sum of their squares gives the total charge density, $\rho(\mathbf{r}) = \sum_n |\varphi_n(\mathbf{r})|^{\mathbf{2}}$. Due to the fermionic nature of the electrons, the antisymmetry principle must be satisfied. This is taken into account if this product is replaced by a determinant (called a Slater determinant) which columns contain the N one electron functions, and which rows account for the coordinates of the N electrons:

[1] Some authors reserve the term ab initio for methods related to the Hartree-Fock approximation, and the term first-principles to denote DFT methods. We will, instead, use one or the other denomination indistinctly.

$$\Psi = \frac{1}{\sqrt{N!}} \begin{vmatrix} \varphi_1(r_1) & \varphi_2(r_1) & \cdots & \varphi_N(r_1) \\ \varphi_1(r_2) & \varphi_2(r_2) & \cdots & \varphi_N(r_2) \\ \vdots & \vdots & \ddots & \vdots \\ \varphi_1(r_N) & \varphi_2(r_N) & \cdots & \varphi_N(r_N) \end{vmatrix} \tag{2.8}$$

The electronic energy E is calculated in terms of the Hamiltonian $\hat{H}$ given in equation 2.5, omitting the internuclear Coulomb term.

$$E = \left\langle \Psi \left| \hat{H} \right| \Psi \right\rangle \tag{2.9}$$

Combining equations 2.5, 2.8 and 2.9, the system energy E can be expressed as:

$$E = \sum_{i=1}^{N} H_i + \frac{1}{2} \sum_{i=1}^{N} \sum_{j=1}^{N} (J_{ij} - K_{ij}) \tag{2.10}$$

where H_i defines a one electron integrals matrix containing the electron kinetic energy and the attraction between electron i and the nuclei, J_{ij} is known as the Coulomb integral and represents the repulsion between electrons i and j, and K_{ij} is called Exchange integral which contains the interaction of two electrons as a result of the exclusion principle. Each of these matrix elements can be described as follows:

$$H_{ii} = -\frac{1}{2} \left\langle \varphi_i(r_1) \left| \nabla_1^2 \right| \varphi_i(r_1) \right\rangle - \left\langle \varphi_i(r_1) \left| \sum_{A=1}^{M} \frac{Z_A}{r_{1A}} \right| \varphi_i(r_1) \right\rangle \tag{2.11}$$

$$J_{ij} = \left\langle \varphi_i(r_1)\varphi_j(r_2) \left| \frac{1}{r_{12}} \right| \varphi_i(r_1)\varphi_j(r_2) \right\rangle \tag{2.12}$$

$$K_{ij} = \left\langle \varphi_i(r_1)\varphi_j(r_2) \left| \frac{1}{r_{12}} \right| \varphi_j(r_1)\varphi_i(r_2) \right\rangle \tag{2.13}$$

Implementation of the variational theorem requires the minimization of the energy with respect to the orbitals, which leads to a set of N equations:

$$\hat{F}(r_1) \left| \varphi_i(r_1) \right\rangle = \sum_{j=1}^{N} \epsilon_{ij} \left| \varphi_j(r_1) \right\rangle \tag{2.14}$$

where ϵ_{ij} are the Lagrange multipliers arising from the orthonormality constraint included in the minimization, $\langle \varphi_i(r_1) | \varphi_j(r_1) \rangle = \delta_{ij}$. The N spin-orbitals φ_i which solve these equations are called molecular Hartree Fock orbitals, and $\hat{F}$ is the Fock operator:

$$\hat{F}(r_1) = \hat{H}_i(r_1) + \sum_{j=1}^{N} \left[\hat{J}_j(r_1) - \hat{K}_j(r_1) \right] \tag{2.15}$$

$\hat{H}_i$, $\hat{J}_j$ and $\hat{K}_j$ operators are defined as:

$$\hat{H}_i(r_1)\varphi_i(r_1) = -\frac{1}{2}\nabla_1^2\varphi_i(r_1) - \sum_{A=1}^{N} \frac{Z_A}{r_{1A}}\varphi_i(r_1) \tag{2.16}$$

$$\hat{J}_{ij}(r_1)\varphi_i(r_1) = \left[\int dr_2 \varphi_j^*(r_2) r_{12}^{-1} \varphi_j(r_2) \right] \varphi_i(r_1) \tag{2.17}$$

$$\hat{K}_{ij}(r_1)\varphi_i(r_1) = \left[\int dr_2 \varphi_j^*(r_2) r_{12}^{-1} \varphi_i(r_2) \right] \varphi_j(r_1) \tag{2.18}$$

It is convenient to diagonalize the matrix associated with equation 2.14, to arrive to an eigenvalue problem:

$$\hat{F}(r_1) \left| \varphi_i(r_1) \right\rangle = \epsilon_i \left| \varphi_i(r_1) \right\rangle \tag{2.19}$$

where the eigenfunctions $\varphi_i(r_1)$ are the so called canonical spin-orbitals, with energies given by their eigenvalues ϵ_i. We note that these eigenvalue equations must be solved self-consistently, because the Fock operator $\hat{F}(r_1)$ depends on the orbitals $\varphi_i(r_1)$ (see equations 1.15, 1.17 and 1.18), which in turn depend on $\hat{F}(r_1)$. The procedure to solve this system consists in providing a starting guess for the orbitals to compute $\hat{F}(r_1)$, from which a new set of orbitals is obtained by diagonalizing 2.19. This iterative procedure is known as a self consistent field (SCF) calculation. When the iterative procedure converges, as a final result a group of molecular orbitals and their energies are found.

Due to the great complexity of the spin-orbitals and the iterative procedure, direct numerical solution of $\varphi_i(r)$ wave functions has been applied successfully only in the case of atoms and diatomic molecules. In order to deal with larger systems, Roothaan and Hall introduced another approximation [1, 2] in which the molecular orbitals are expressed as a linear combination of basis functions ϕ_k:

$$\varphi_i = \sum_{k=1}^{L} c_{ki}\phi_k \tag{2.20}$$

Under this approximation, the problem reduces to obtaining the matrix of the c_{ki} coefficients that minimize the energy. After some algebraic manipulation of the Hartree-Fock equations and introducing the basis expansion 2.20, the Roothaan equations can be de-

rived:

$$\sum_{k=1}^{L} c_{ki} \left(\left\langle \phi_\nu \left| \hat{F} \right| \phi_k \right\rangle - \epsilon_i \left\langle \phi_\nu | \phi_k \right\rangle \right) = 0 \tag{2.21}$$

where a set of matrix elements depending on the basis functions are defined as:

$$F_{k\nu} = \left\langle \phi_\nu \left| \hat{F} \right| \phi_k \right\rangle \tag{2.22}$$

$$S_{k\nu} = \left\langle \phi_\nu | \phi_k \right\rangle \tag{2.23}$$

Equation 2.21 can be expressed as $\mathbf{FC} = \mathbf{SC}\epsilon$, where **C** represents the coefficient matrix, and ϵ the diagonal matrix of the orbital energies. If the elements of the **F** matrix are known, it is possible to compute the coefficient matrix and the energies solving the following system:

$$\det \left(\mathbf{F} - \epsilon \mathbf{S} \right) = 0 \tag{2.24}$$

Again, the matrix **F** depends on the c_{ki} and the problem must be solved in an iterative way. First, an initial guess for the coefficients has to be provided to compute the *F*. Then the eigenvalues ϵ_i are obtained and a set of new coefficients is calculated. The procedure starts all over again, and a series of cycles is performed until the coefficient matrix remains invariable.

The Hartree-Fock method can be very accurate for certain applications, but on the other hand it systematically overestimates some molecular properties and underestimates others [1]. The HF method is not exact, essentialy because of two limitations. One lies on the quality of the basis functions: the better the basis set, the higher the accuracy of the calculation (and the lower the energy). The basis set size can be systematically increased until the energy is converged with respect to the basis, i.e., addition of extra basis functions does not produce any significant decrease in the energy. This is called the Hartree-Fock limit. But even at this limit, the energy E_{HF}^{limit} is somehow larger than the experimental value. This is inherent to the construction of the wavefunction as a single Slater determinant: the description of the exact wavefunction can only be achieved through a sum of Slater determinants (technically, an infinite sum). From a physical viewpoint, the inaccuracy can be ascribed to the way the electron-electron interaction is computed: the Coulomb integrals consider the energy of each electron in the averaged potential of all the rest, a treatment known as the mean field approximation, which ignores the instantaneous distribution of the electronic charge. In particular, this approach does not forbid the possibility of two electrons of different spin sharing the same spatial coordinates. However, the probability

of finding two electrons at the same point in space must be zero, regardless of their spins. Since this requirement is not verified in the HF approach, it is said that the electrons are uncorrelated, and this inaccuracy is called the correlation energy:

$$E_{corr} = E_{exact} - E_{HF}^{limit} \tag{2.25}$$

To improve the HF method by the inclusion of the correlation energy, post- Hartree-Fock methods were developed. To mention three important examples,[2] the Configuration Interaction method (CI), Møller-Plesset perturbation theory (MP), and Density Functional Theory (DFT), are all different approaches to the wave-function which take into account the correlation energy in some way or the other.

In the CI method, the system wave-function is expressed as a linear combination of different Slater determinants which represent several electronic configurations related to the ground and excited states. The variant including all possible excited configurations for a given basis set is called Full-CI and constitutes the most accurate approach to the correlation energy, but its computational cost diverges very fast and only very small systems are manageable at this level [2].

On the other hand, the Møller-Plesset method is based on perturbation theory, which estimates the energy and the wave-function of a system described by a Hamiltonian $\hat{H}$, from the knowledge of the solution of a similar Hamiltonian $\hat{H}^o$. Then, a perturbation $\hat{H}'$ is defined: $\hat{H}' = \hat{H} - \hat{H}^o$. Within the Møller-Plesset technique $\hat{H}$ represents the true molecular electronic Hamiltonian and $\hat{H}^o$ the HF Hamiltonian. Solutions can be achieved through this method considering corrections at different orders: the widespread MP2 scheme takes corrections to the energy and the wave-function up to second order [1,2], and provides results of an intermediate accuracy between HF and CI, being of course computationally less demanding than the later. At the same time, perturbation methods are not based on the variational principle, meaning that energies lower than the exact energy can be obtained.

Finally, the density functional methodology takes into account the correlation energy in a distinctive way. In comparison to other methods, it offers an excellent trade-off between computational cost and accuracy, and for this reason in the last two decades it became the first choice for ab initio simulations involving some tens of atoms in chemistry and physics. In particular, the simulations in this thesis are based on density functional theory. In the following section the DFT approach is examined in detail.

[2]There exists a long list of correlated methods coming from the areas of quantum chemistry and condensed matter physics, including Coupled Cluster methods (CC) [1], Time Dependent Density Functional theory (TDDFT) [3], and the GW approximation [4], among others.

2.1.2 Density Functional Theory

Thomas and Fermi were the first to propose the electronic density as the main variable of a quantum system. This idea is extremely attractive due to the simplification entailed in this new conception. While the wave function of a polielectronic system depends on the coordinates of the N particles ($\psi = \psi(r_1, ...r_N)$), the charge density is a function of the the spatial coordinates ($\rho = \rho(x, y, z)$), thus translating a problem of $3N$ variables to just 3.

Around 1960 Hohenberg and Kohn [5] introduced two theorems which provided the grounds to develop a quantum methodology based on the electron density. The first theorem states that the electronic charge density (ρ) is univocally determined by the Hamiltonian, or, more specifically, by the external potential $v(\mathbf{r})$, and viceversa, that is, a given charge density may only be associated with a particular potential.[3] Since the Hamiltonian determines univocally the wave function of the system (ψ), ρ must also determine the energy and all the other properties that are calculated from ψ. Therefore, the ground state energy can be expressed as functional of the ground state charge density: $E_0 = E_0[\rho_0]$.

The reciprocity between the external potential $v(\mathbf{r})$ and the ground state electronic density ρ_0 can be proved by reduction to the absurd [6]. To this purpose it can be assumed that two different potentials $v(\mathbf{r})$ and $v'(\mathbf{r})$ produce the same ground state density, ρ_0. As there are two different external potentials, there must be two different Hamiltonians $\hat{H}$ and $\hat{H}'$ corresponding to $v(\mathbf{r})$ and $v'(\mathbf{r})$ respectively. If we call Ψ and Ψ' the two solutions of these two Hamiltonians associated with the same electronic density, we have: $\int \cdots \int |\Psi|^2 d\mathbf{r_2} \cdots d\mathbf{r_N} = \int \cdots \int |\Psi'|^2 d\mathbf{r_2} \cdots d\mathbf{r_N} = \rho_0(\mathbf{r})$. Considering the variational principle:

$$E_0 < \langle \Psi' | \hat{H} | \Psi' \rangle = \langle \Psi' | \hat{H}' | \Psi' \rangle + \langle \Psi' | \hat{H} - \hat{H}' | \Psi' \rangle \tag{2.26}$$

Recalling that the difference between $\hat{H}$ and $\hat{H}'$ originates exclusively in the external potential, we can expand the last term in the equation above as:

$$\begin{aligned} \langle \Psi' | \hat{H} - \hat{H}' | \Psi' \rangle &= \langle \Psi' | v(\mathbf{r}) - v'(\mathbf{r}) | \Psi' \rangle \\ &= \int [v(\mathbf{r}) - v'(\mathbf{r})] \, |\Psi'|^2 \, d\mathbf{r} \\ &= \int [v(\mathbf{r}) - v'(\mathbf{r})] \, \rho_0(\mathbf{r}) \, d\mathbf{r} \end{aligned} \tag{2.27}$$

[3] In the jergon of density functional theory, the external potential is $v(\mathbf{r}) = \sum_I \frac{Z_I}{|\mathbf{r} - \mathbf{R}_I|}$, the electrostatic field of the nuclei. The other terms in the electronic Hamiltonian (the kinetic energy of the electrons and the electron-electron repulsion) are invariant from system to system, so it is really $v(\mathbf{r})$ who characterizes $\hat{H}_{el}$.

Substituting this result in equation 2.26 the following inequality is obtained:

$$E_0 < E_0' + \int [v(\mathbf{r}) - v'(\mathbf{r})]\ \rho_0(\mathbf{r})\ d\mathbf{r} \tag{2.28}$$

The above derivation can be repeated, replacing Ψ' by Ψ and $\hat{H}$ by $\hat{H}'$ in equation 2.26, in which case a different inequality is obtained:

$$E_0' < E_0 + \int [v'(\mathbf{r}) - v(\mathbf{r})]\ \rho_0(\mathbf{r})\ d\mathbf{r} \tag{2.29}$$

Combining equations 2.28 and 2.29 the following absurd relation arises:

$$E_0 + E_0' < E_0' + E_0 \tag{2.30}$$

which proves that the hypothesis of two different external potentials linked to the same ground state electronic density is incorrect.

As discussed above, the Hohenberg-Kohn theorem implies that ρ determines the system wave-function and all the molecular properties, in particular the total energy:

$$E[\rho] = T[\rho] + V_{ee}[\rho] + V_{eN}[\rho] \tag{2.31}$$

where T denotes the electronic kinetic energy, V_{ee} the potential energy due to the electrostatic repulsion between electrons, and V_{eN} the potential energy arising from the attraction between nuclei and electrons.

The second theorem is known as the variational Hohenberg-Kohn theorem. It postulates that for any ρ' which satisfies $\int \rho'(\mathbf{r})d\mathbf{r} = N$ and $\rho'(\mathbf{r}) \geq 0$ for the whole space, then $E[\rho'] \geq E_0$. The equality is verified only if ρ' is the ground state density, implying that ρ_0 minimizes the energy functional $E[\rho]$ as ψ_0 minimizes the total energy $\left\langle \psi \middle| \hat{H} \middle| \psi \right\rangle$.

This framework establishes interesting connections between the charge density and the energy, but says nothing regarding the practical procedure to compute one or the other. A few years later, in 1965, Kohn and Sham [7] set out a formulation based on a fictitious reference system of non-interacting electrons which density (ρ_s) is identical to the ground state density of the real system (ρ_0) [6]. In this approach the external potential for the non-interacting particles, v_s, induces a density $\rho_s = \rho_0$. The advantage resides in the fact that the kinetic energy $T[\rho]$ of this reference system is simple to calculate. The Hamiltonian operator $\hat{H}_s$ of such reference system can be written as:

$$\hat{H}_s = \sum [-\frac{1}{2}\nabla_i^2 + v_s(r_i)] \equiv \sum_{i=1}^{N} \hat{h}_i^{KS} \tag{2.32}$$

where $\hat{h}_i^{KS}$ is the Kohn-Sham one-electron operator. In a similar way as was proposed for

the case of the Hartree-Fock method, the wavefunction Ψ_s of the N-electrons system can be expressed as the Slater determinant of the $\hat{h}_i^{KS}$ eigenfunctions. Exploiting the variational Hohenberg-Kohn theorem, the energy functional can be minimized with respect to the one-electron functions φ^{KS} (known as the Kohn-Sham spin-orbitals), which can be calculated solving an eigenvalue problem analogous to the HF equations:

$$\hat{h}_i^{KS}\varphi_i^{KS} = \epsilon_i\varphi_i^{KS} \tag{2.33}$$

$$\Psi_s(r_1, r_2, ...r_N) = \frac{1}{\sqrt{N!}}\begin{vmatrix} \varphi_1(r_1) & \varphi_2(r_1) & \cdots & \varphi_N(r_1) \\ \varphi_1(r_2) & \varphi_2(r_2) & \cdots & \varphi_N(r_2) \\ \vdots & \vdots & \ddots & \vdots \\ \varphi_1(r_N) & \varphi_2(r_N) & \cdots & \varphi_N(r_N) \end{vmatrix} \tag{2.34}$$

The electronic density of the system can be obtained as:

$$\rho_s = \sum_i^N \left|\varphi_i^{KS}\right|^2 \tag{2.35}$$

As mentioned above, the reason for introducing a non-interacting system of electrons lies on the simplicity to compute the kinetic energy:

$$T_s = -\frac{1}{2}\langle\Psi_s|\sum_i \nabla_i^2|\Psi_s\rangle = -\frac{1}{2}\langle\varphi_i^{KS}|\sum_i \nabla_i^2|\varphi_i^{KS}\rangle \tag{2.36}$$

By calling ΔT to the difference between the kinetic energies of the fictitious and the real systems, and ΔV_{ee} to the non-classical contribution to the interaction between electrons,

$$\Delta T[\rho] = T[\rho] - T_s[\rho] \tag{2.37}$$

$$\Delta V_{ee}[\rho] = V_{ee}[\rho] - \frac{1}{2}\iint \frac{\rho(r_1)\rho(r_2)}{r_{12}}dr_1dr_2 \tag{2.38}$$

$$E_{xc}[\rho] = \Delta T[\rho] + \Delta V_{ee}[\rho] \tag{2.39}$$

then equation 2.31 can be rewritten as:

$$E[\rho] = T_s[\rho] + V_{eN}[\rho] + \frac{1}{2}\iint \frac{\rho(r_1)\rho(r_2)}{r_{12}}dr_1dr_2 + E_{xc}[\rho] \tag{2.40}$$

In principle, equation 2.40 is an exact expression for the electronic energy. The first term on the right hand side is the kinetic energy of a non-interacting system of electrons, the second amounts to the potential energy between nuclei and electrons, the third one specifies the Coulomb potential energy arising from a classical distribution of negative charge,

and the fourth one, called the exchange correlation energy functional, accounts for the contributions not considered in the previous terms. These contributions are essentially corrections considering the quantum nature of the electron-electron interaction, and the corresponding effects on their kinetic energy. In practice, the exact expression of E_{xc} as a function of the density is not known, and therefore different schemes to estimate this term have been devised [6].

Given a functional to describe $E_{XC}[\rho]$, the electronic energy in 2.40 can be written as a function of ρ and the form of the Kohn-Sham operator can be established. This leads to the Kohn-Sham (KS) equations:

$$\left[-\frac{1}{2}\nabla_1^2 - \sum_A \frac{Z_A}{r_{1A}} + \int \frac{\rho(r_2)}{r_{12}} dr_2 + v_{xc}(1)\right] \left|\varphi_i^{KS}\right\rangle = \epsilon_i^{KS} \left|\varphi_i^{KS}\right\rangle \tag{2.41}$$

where the exchange-correlation potential v_{xc} is the functional derivate of E_{xc} with respect to ρ. The sum of Coulombic interactions plus the exchange correlation potential defines the total KS potential:

$$v_{KS}(1) = -\sum_A \frac{Z_A}{r_{1A}} + \int \frac{\rho(r_2)}{r_{12}} dr_2 + v_{xc}(1) \tag{2.42}$$

so that equation 2.41 can be written as:

$$\left[-\frac{1}{2}\nabla_1^2 + v_{KS}(1)\right] \left|\varphi_i^{KS}\right\rangle = \epsilon_i^{KS} \left|\varphi_i^{KS}\right\rangle \tag{2.43}$$

Similarly to the HF orbitals, the KS orbitals can be expanded as a linear combination of basis functions as in 2.20. This leads to a new set of equations analogous to the Roothaan equations, which can be expressed in a matricial format:

$$\mathbf{h^{KS}C} = \mathbf{SC}\epsilon \tag{2.44}$$

Hence, the Kohn-Sham framework builds a path from the Hohenberg-Kohn theorems to a practical method for the calculation of a set of orbitals, the charge density, the total energy, and the other properties of the system. Also in this case the KS operator $\hat{h}_{KS}$ depends on the matrix of the coefficients $\mathbf{C}$, therefore the system 2.44 is solved in an iterative way.

The introduction of an approximate form for E_{xc} constitutes the main approximation in the KS formulation (beyond the use of a finite basis set), and consequently the accuracy of DFT methods heavily relies on the quality of the exchange-correlation functional [6]. There are many different approximations to E_{xc}. In most of them, $E_{XC}[\rho]$ is splitted into two contributions: correlation and exchange. The first kind of functionals developed was

known as the Local Density Approximation (LDA) [8], where the exchange and correlation effects are treated exclusively in a local way. The basic idea was to define $E_{xc}[\rho]$ equal to the exchange and correlation energies of an homogeneous gas of electrons of density ρ. This approximation performs well when the density does not vary sharply in space, as is the case for metals and systems with a delocalized electronic charge. For molecules, the next generation of functionals, developed in the late 80's and 90's, brought about significant improvement. The common feature about this family of functionals, known as the Generalized Gradient Approximation (GGA), is the incorporation of the gradient of the charge density ($\nabla\rho$) in the formulation, either in an empirical way,[4] or based on first-principles derivations. The inclusion of $\nabla\rho$ gave a higher flexibility to GGA [9,10], making it possible to describe more accurately the electronic density variation and localization. Within this group, the PBE [11] and the PW91 [12, 13] exchange-correlation functionals are widely used in chemistry and condensed matter simulations. In particular, the PW91 formulation is the one used in this thesis. Other important family of energy functionals incorporate the exact exchange provided by HF [14, 15], and are therefore known as hybrid functionals. Among them, B3LYP is perhaps the most frequently employed in quantum chemistry simulations. Aside from these, there has been a huge development of new functionals in recent years [4], but in general terms the performance of GGAs—considering the balance between accuracy and cost—has not been excelled. In many cases, the recent developments were desinged for high accuracy in a particular family of compounds, or for the estimation of a specific property.

2.2 Quantum mechanics for extended systems

In the previous sections, electronic structure methods were discussed in general. To represent systems that exhibit periodicity in one or more dimensions, such as solids (3D), surfaces (2D) or polymers (1D), periodic boundary conditions (PBC) must be included in the formulation, which will lead to periodic charge densities and potentials. In the following, the main concepts regarding the calculation of the electronic structure of infinitely repeated systems are going to be introduced in a DFT framework.

Before starting, though, we want to call the attention on two technical issues. In the Kohn-Sham equations 2.41, the external potential and the electronic density are:

$$v_{ext} = -\sum_{I=1}^{P} \frac{Z_I}{|\mathbf{r} - \mathbf{R}_I|} \tag{2.45}$$

[4]For this reason DFT methods were once not considered to be part of the ab initio category.

$$\rho(\mathbf{r}) = \sum_{i=1}^{N} f_i \left|\varphi(\mathbf{r})\right|^2 \tag{2.46}$$

where N is the number of electrons, and f_i are the occupation number for each one-electron eigenstates. For spin-unpolarized insulators or closed-shell molecules, $f_i = 2$ for the N/2 lowest states and $f_i = 0$ otherwise. In periodic boundary conditions, the infinite sum in 2.45 does not converge. On the other hand, the expansion of a periodic charge density requires periodic spin-orbitals, and therefore a set of periodic basis functions. These are part of the features which characterize electronic structure implementations in PBC, and mark the difference with respect to calculations of isolated systems.

2.2.1 Periodic structures, Bloch´s theorem and Brillouin zone

For any periodic structure as a perfect solid, it is always possible to identify a group of atoms which is infinitely replicated along the three directions in space. In fact, there are many ways of characterizing this group of atoms [16, 17]. However, there is a minimal choice that contains the whole symmetry of the system. This is called a *Wigner-Seitz* cell, which, together with the unit or primitive vectors that indicate the cell size, and the directions of replication, contain the information to reproduce the whole crystal. If we call $\mathbf{a}_1, \mathbf{a}_2, \mathbf{a}_3$ the primitive vectors, then the volume of the unit cell, Ω, is given by $\Omega = \mathbf{a}_1 \cdot (\mathbf{a}_2 \times \mathbf{a}_3)$. The set of integer combinations of these vectors make up a structure known as the *Bravais lattice*.

Although the *Wigner-Seitz* cell comprises the minimum group of atoms required to specify the structure of a solid, in cases in which the primitive vectors are not orthogonal, it might be preferable to describe the solid with a cubic or rectangular cell. Not all solids can be described with the minimum quantity of atoms in a cubic system, and may require the specification of the positions of additional atoms that will allow the correct representation of the solid by replication in a cubic system.

Bloch's Theorem The eigenstate ψ of a one-electron Hamiltonian $\hat{H} = -\dfrac{\hbar^2}{2m}\nabla^2 + u(\mathbf{r})$, where $u(\mathbf{r})$ is a potential with the periodicity of the lattice,[5] can be written as a function of the same periodicity times a phase factor $e^{i\mathbf{k}\cdot\mathbf{R}}$ arising from the translational symmetry. In other words, the Bloch's theorem proposes that

$$\psi_{\mathbf{k}}(\mathbf{r}) = e^{i\mathbf{k}\cdot\mathbf{r}} u_{\mathbf{k}}(\mathbf{r}) \tag{2.47}$$

with

[5] This implies that $u(\mathbf{r}) = u(\mathbf{r}+\mathbf{R})$ for all $\mathbf{R} = m_1\mathbf{a}_1 + m_2\mathbf{a}_2 + m_3\mathbf{a}_3$ in a Bravais lattice, where m_1, m_2 and m_3 are integers.

$$u_{\mathbf{k}}(\mathbf{r}) = u_{\mathbf{k}}(\mathbf{r} + \mathbf{R}) \tag{2.48}$$

The wave vector **k** is going to be introduced in the next section. The eigenstates $\psi_{\mathbf{k}}$ are also known as the Bloch functions. Equations 2.47 and 2.48 imply that

$$\psi_{\mathbf{k}}(\mathbf{r} + \mathbf{R}) = e^{i\mathbf{k}\cdot\mathbf{R}}\psi_{\mathbf{k}}(\mathbf{r}) \tag{2.49}$$

It can be seen that the probability density is periodic in the lattice ($|\psi_{\mathbf{k}}(\mathbf{r})|^2 = |\psi_{\mathbf{k}}(\mathbf{r} + \mathbf{R})|^2$), even if the wave function is not necessarily periodic because of the phase factor.

Brillouin zone There is a minimum set of **k** vectors which satisfy $e^{i\mathbf{k}\cdot\mathbf{a}_i} = 1$, giving rise to a wave function in equation 2.47 that is in phase in all the replicas of the unit cell. Vectors belonging to this particular set, denoted $\mathbf{b}_i$, are known as *primitive reciprocal lattice vectors*. They must satisfy the relation $\mathbf{a}_i \cdot \mathbf{b}_j = 2\pi\delta_{ij}$, from which the definition of the reciprocal vectors can be obtained:

$$\mathbf{b}_1 = 2\pi\frac{\mathbf{a}_2 \times \mathbf{a}_3}{\Omega};\ \ \mathbf{b}_2 = 2\pi\frac{\mathbf{a}_3 \times \mathbf{a}_1}{\Omega};\ \ \mathbf{b}_3 = 2\pi\frac{\mathbf{a}_1 \times \mathbf{a}_2}{\Omega} \tag{2.50}$$

This set of vectors define a primitive cell volume $\Omega_R = \mathbf{b}_1 \cdot (\mathbf{b}_2 \times \mathbf{b}_3) = (2\pi)^3/\Omega$ in the reciprocal space. The region circunscribed in this volume receives the name of *first Brillouin zone* or simply Brillouin zone (BZ). It can be seen that reciprocal vectors contained in the first BZ are enough to determine all possible electronic wave functions satisfying 2.47. Given the fact that $u_{\mathbf{k}}$ is periodic, it can be replaced in equation 2.47 by the Fourier series expansion:

$$\psi_{\mathbf{k}}(\mathbf{r}) = e^{i\mathbf{k}\cdot\mathbf{r}}\sum_{\mathbf{G}} C_{\mathbf{k}+\mathbf{G}}e^{i\mathbf{G}\cdot\mathbf{r}} \tag{2.51}$$

where $\mathbf{G} = n_1\mathbf{b}_1 + n_2\mathbf{b}_2 + n_3\mathbf{b}_3$ are all the reciprocal lattice vectors. In principle, any **k** vector is allowed in an infinite system, but wave vectors outside the BZ can be expressed as $\mathbf{k}' = \mathbf{k} + \mathbf{G}_0$, with **k** inside the BZ, and the expression for $\psi_{\mathbf{k}'}(\mathbf{r})$

$$\psi_{\mathbf{k}'}(\mathbf{r}) = e^{i\mathbf{k}'\cdot\mathbf{r}}\sum_{\mathbf{G}} C_{\mathbf{k}'+\mathbf{G}}e^{i\mathbf{G}\cdot\mathbf{r}} \tag{2.52}$$

turns out to be equal to $\psi_{\mathbf{k}}(\mathbf{r})$. As a result, we have that an infinite solid (with an infinite number of electrons) can be mapped in a unit cell containing a finite number of electrons and an infinite number of **k** vectors in the BZ. Since nearby **k** vectors carry very similar information, the number of **k** vectors can be reduced.

Brillouin zone sampling From equation 2.49, the general expression for the electronic density associated with a single electronic state $\psi_{\mathbf{k}}$ of the periodic potential is:

$$\rho(\mathbf{r}) = \sum_{\mathbf{k}\epsilon BZ} \omega_{\mathbf{k}} \left|\psi_{\mathbf{k}}(\mathbf{r})\right|^2 \tag{2.53}$$

where the sum runs over all the **k** vectors inside the BZ and the weight factor $\omega_{\mathbf{k}}$ depends on the symmetry of the unit cell. In the same way, the energy and all molecular properties depend on $\psi_{\mathbf{k}}$ for **k** points. Since **k** is a continuous index, the summation 2.53 becomes an integral. In practical computational approaches, however, it is only feasible to solve $\psi_{\mathbf{k}}$ for a finite number of wave vectors, and the full BZ integral is replaced by a sum over a finite set of **k**-points [4], a technique called Brillouin zone sampling. The number and locations of the **k**-points included in the sum depend on the nature of the system, and in general is proportional to Ω_R, i.e., inversely proportional to the size of the cell. It is common to replace the unit cell by the so called supercell, which is composed by more than one unit cell, thus reducing the number of **k**-points required in the BZ sampling. For metals, a fine sampling is typically needed to reproduce the main features of the electronic structure (the eigenvalues $\psi_{\mathbf{k}}$ may vary significantly along the reciprocal space), while semiconductors and insulatores may get a satisfactory description with a sampling on a few selected **k**-points. A standard procedure consists in sampling the eigenfunctions in a regular grid in the reciprocal space, which density is increased until the energy or any other properties are converged. This scheme is called the Monkhorst-Pack grid sampling [18]. In some cases, when large supercells are employed, a single **k**-point may suffice to obtain reasonable results. A sampling limited to **k**=(0,0,0) is known as Γ-point sampling.[6]

As a consequence of the Bloch´s theorem, the Kohn-Sham equations (see expression 2.41) in a periodical external potential can be written as:

$$\left\{-\frac{1}{2}\nabla^2 + v_{ext}(\mathbf{r}) + \int \frac{\rho(\mathbf{r}')}{|\mathbf{r}-\mathbf{r}'|} d\mathbf{r} + v_{xc}[\rho]\right\} \varphi_i^{(\mathbf{k})}(\mathbf{r}) = \varepsilon_i^{(\mathbf{k})} \varphi_i^{(\mathbf{k})}(\mathbf{r}) \tag{2.54}$$

where now a set of coupled KS equations have to be solved, one for each **k**-point included in the BZ. The coupling between different **k**-points results from the electronic density, which is calculated as a BZ average. By replacing $\psi_{\mathbf{k}}$ in equation 2.53 by the sum over the set of occupied electronic states, we obtain:

$$\rho(\mathbf{r}) = \sum_{\mathbf{k}\epsilon BZ} \omega_{\mathbf{k}} \sum_{i=1}^{N_{\mathbf{k}}} f_i^{(\mathbf{k})} \left|\varphi_{\mathbf{k}}^{(\mathbf{k})}(\mathbf{r})\right|^2 \tag{2.55}$$

where $N_{\mathbf{k}}$ is the number of electronic states occupied at each **k**-point, and $f_i^{(\mathbf{k})}$ is the occu-

[6] Conventionally, the coordinates origin in reciprocal space is known as the Γ-point.

pation number of band *i* at wave vector $\mathbf{k}$.[7] For systems with a band gap (insulators and semiconductors), $N_{\mathbf{k}}$=N and $f_i^{(\mathbf{k})} = 1$ independently of *i* and $\mathbf{k}$.

2.2.2 Pseudopotentials

The following part of the discussion will be focused on two technical but important questions arisen at the beginning of this section and related to the periodic setting: (1) the way to represent the external potential, $v_{ext}(\mathbf{r})$, and (2) the appropriate basis set to describe accurately the physics of the system. It turns out that these two questions are linked. It would not be a good idea to choose a basis set without answering first how the strong interaction between nuclei and electrons will be represented, or putting this the other way around, the better way to represent this interaction would depend on the basis set that is going to be used.

In the history of solid state methods, different approaches were employed to describe the electronic states of materials, depending on their nature. For metals, where electrons can be thought as not strongly bound to the ions, a free electron model which includes just the kinetic energy in the electronic Hamiltonian (the *Sommerfeld model* [16]) was among the first quantum-mechanical treatments proposed for solids. This approximation was successful to reproduce qualitatively some general features of metals, as in the case of the dependence of the thermal capacity with temperature. In this framework, plane waves functions were the solutions to the Schrödinger equation in the periodic boundary conditions.

The next step, applicable to weakly bound electrons, where the external potential of the nuclei is very small with respect to the kinetic energy, was to consider this potential as a perturbation [16]. Within this approach the PBC are satisfied through the Bloch´s theorem and electronic bands and gaps emerge as a consequence of the potential. This model accounts for the general behavior of metals and can describe reasonably well some semiconductors.

On the other side, for strongly bound electrons such as insulators, the *Tight-Binding model* was developed [19]. In general terms, combinations $\chi_{k,l}$ of localized basis functions,[8] which in turn satisfy the Bloch's theorem, are proposed to expand the solutions of the electronic Hamiltonian, $\psi_{\mathbf{k}} = \sum_l c_{\mathbf{k},l}\chi_{\mathbf{k},l}$. In the spirit of the HF method, the energies and the $c_{\mathbf{k},l}$ coefficients are obtained by solving a non-linear eigenvalue problem. A basic approximation of the method is to neglect most off-diagonal elements in the Hamiltonian matrix, which reduces significantly the number of integrals and calculations. In this

[7] Bands are defined by the eigenvalues ε_i as a function of $\mathbf{k}$.

[8] These combinations are called Bloch sums and have the form of $\chi_{k,l}(\mathbf{r}) = \sum_{\mathbf{n}} e^{i\mathbf{k}\mathbf{n}\mathbf{R}}\phi_l(\mathbf{r} - \mathbf{n}\mathbf{R})$, where $\mathbf{R}$ are the lattice vectors and ϕ_l are localized basis functions.

way systems of thousands of electrons become tractable, but the description deteriorates with delocalization. Tight-binding models perform well in solids with localized electrons, whereas the free-electron or nearly free-electron models provide reasonable descriptions of metals. In between these two extremes, more elaborate treatments are needed.

Bloch's theorem and the models discussed above suggest that the natural basis functions to expand the eigenstates of the Hamiltonian in a periodic potential are plane waves. It is then indispensable to find an appropriate form for the external potential that would allow to solve computationally equation 2.54 when the electronic states are expanded in plane waves.

The electronic states can be classified in three categories: (1) *core states*, which are highly localized and not involved in chemical bonds, (2) *valence states*, which are extended and responsible of chemical bonding, and (3) *semi-core states*, which are localized and polarizable but in general do not contribute directly to the chemical bond.

Considering that the core states are not fundamental to chemical bonding, and that for most applications an accurate representation of the core region is not strictly necessary, only valence states are considered. On the same reasoning, there is no crucial information lost if the inner part of the valence wave function is replaced by a smooth, nodeless pseudo-wavefunction. The advantage in this framework is the decrease in the number of basis functions (or plane waves) needed in the Fourier series expansion of the electronic states (equation 2.51). The strong, point-charge potential originated by the nuclei is replaced inside the core region by a *pseudopotential* that is smooth and nodeless, and which solution is the pseudo-wavefunction mentioned above. Consistently, the full nuclear charge is replaced by an effective charge which must be equal to the valence charge. This pseudopotential (PS) is constructed aiming to reproduce as accurately as possible the bonding properties of the true potential.

Pseudopotential theory The origin of this methodology is inspired in the work of Philips and Kleinman [20], where it is shown that a nodeless (not orthogonal to the core states φ_c) smooth wave function $\tilde{\varphi}_v$ can be constructed by combining the core and the true valence wave functions (φ_v):

$$|\tilde{\varphi}_v\rangle = |\varphi_v\rangle + \sum_c \alpha_{cv} |\varphi_c\rangle \tag{2.56}$$

where $\alpha_{cv} = \langle\varphi_c|\tilde{\varphi}_v\rangle \neq 0$. This pseudo-wave function satisfies the modified Schrödinger equation:

$$\left[\hat{H} + \sum_c (\varepsilon_v - \varepsilon_c) |\varphi_c\rangle \langle\varphi_c|\right] |\tilde{\varphi}_v\rangle = \varepsilon_v |\tilde{\varphi}_v\rangle \tag{2.57}$$

where $\hat{H}$ is the Hamiltonian involving the kinetic plus the potential energy, $\hat{H} = \hat{T} + \hat{V}$. This potential represents the electrostatic interaction between the electron and the nucleus: $\hat{V} = -\frac{Z_c}{r}$, where Z_c is the ionic charge. At this point it is useful to rename the operator on the left hand side of equation 2.57 as a pseudopotential $\hat{V}_{PS}$,

$$\hat{V}_{PS} = -\frac{Z_c}{r} + \sum_c (\varepsilon_v - \varepsilon_c) \left|\varphi_c\right\rangle \left\langle\varphi_c\right| \tag{2.58}$$

The core atomic wavefunctions are the spherical harmonics $Y_{lm}(\theta, \phi)$ times a radial function. Then, the pseudopotential $\hat{V}_{PS}$ can be written in a more general form as [4]:

$$\hat{V}_{PS}(\mathbf{r}) = \sum_{l=0}^{\infty} \sum_{m=-l}^{l} v_{PS}^{l}(r) \left|lm\right\rangle \left\langle lm\right| = \sum_{l=0}^{\infty} v_{PS}^{l}(r) \hat{P}_l \tag{2.59}$$

where $|lm\rangle$ represent the spherical harmonics Y_{lm}. When $\hat{V}_{PS}$ acts on a specific electronic wave function, the projector operators $\hat{P}_l$ select the different angular components of the wave function which are then multiplied by the pseudopotential $v_{PS}^{l}(r)$. If l_{max} is the number of occupied core states, then the effect of the ionic core on all the valence wavefunctions of angular momenta greater than l_{max} must be the same, and $\hat{V}_{PS}$ can be expressed as a sum of two contributions which resemble the form in 2.58. These two contributions are normally known as *local* (containing the radial dependence) and *non-local* (discriminating between angular momenta):

$$\hat{V}_{PS} = \sum_{l=0}^{\infty} v_{PS}^{loc}(r) \hat{P}_l + \sum_{l=0}^{l_{max}} \left[v_{PS}^{l}(r) - v_{PS}^{loc}(r)\right] \hat{P}_l = v_{PS}^{loc}(r) \hat{I} + \sum_{l=0}^{l_{max}} \Delta v_{PS}^{l}(r) \hat{P}_l \tag{2.60}$$

The local contribution ($v_{PS}^{loc}(r)$) is an average potential representing the screened Coulomb interaction. The non-local part ($\sum_l \Delta v_{PS}^{l} \hat{P}_l$) acts differently on the various angular components of the wavefunction, to represent the exchange effect of the implicit core states. The short ranged Δv_{PS}^{l} functions are confined to the core region, since at longer distances the nuclei must appear as point charge, irrespective of the angular component.

So far, we discussed two major points of the PS theory: (i) core electrons are removed from the calculations, and the interaction of the valence electrons with the nucleus plus core states (which we call the pseudocore) are replaced by a screened potential, which accounts for the orthonormality of valence and implicit core states. (ii) the full nuclei-electron interaction, including the orthogonality of the valence functions with respect to the core states, is replaced by a softer and nodeless pseudopotential. The absence of nodes inside the core region reduces the size of the Fourier expansion of the pseudo-wavefunction, which is also nodeless and matches the all-electron wavefunction beyond

a cut-off radius. Even if both wavefunctions differ inside the core region, the pseudo-wavefunction accurately captures the bonding properties of the true solution. Figure 2.1 shows the all-electron and the pseudo-wavefunctions obtained for silicon [21]. Difference in softness for each kind of function can be appreciated. In what follows, the technical aspects of how pseudopotentials are constructed is outlined.

Construction of pseudopotentials There is no single recipe to build a pseudopotential. In the past, PS were generated by fitting experimental energy bands [22, 23]. The main problem about these PS was that they were created to reproduce a specific solid structure and were not accurate to model the same atomic species in a different environment. The aptitude of a PS to represent a given atom in different environments is called *transferability*.

A pseudopotential must fulfill the following requirements: (1) beyond a certain distance both the all-electron and the pseudo wavefunctions must exhibit the same decay, and (2) the pseudo-wave function has to be an eigenstate of the pseudo-Hamiltonian with the same eigenvalue of the all-electron wave function. Then, given a pseudo-wavefunction, the PS can then be constructed through the inversion of the radial Schödinger equation. This is done for a *reference* configuration which in general is the neutral atom configuration, but it could also be an ionized electronic configuration that represents better the atom in the desired, solid environment [21].

An additional requirement which can be added to the construction scheme, is for the pseudo-wavefunction to preserve the norm inside the cutoff radius. Pseudopotentials of this kind are known as *norm-conserving*, first introduced in 1979 [24]. This extra requirement ensures, through the Friedel sum rule [23, 25], that a PS created in a specif environment can be exported to other environment without a significant loss in accuracy, because the variation of the pseudo-wave function resulting from the environmental change reproduces the variation of the all-electron wave function. In other words, the norm conservation ensures *transferability*. However, a disadvantage of *norm-conserving* PS is its *hardness*, which means that a relatively large amount of plane waves is required to represent the electronic wave functions ψ in the core region [26, 27].

Looking to reduce the hardness imposed by the norm-conserving condition, Vanderbilt [28] developed in the 90's a new smooth and highly transferable family of PS which is conventially called *ultrasoft*. These pseudopotentials do not conserve the norm, but in exchange the mathematics around their construction is quite complicated, and beyond the scope of this thesis. Within this approach, the corresponding wavefunctions exhibit a much smoother variation around the core region, which allows for a significant decrease in the required basis set size, typically reduced by a half or a thirth. For this reason, ultrasoft PS

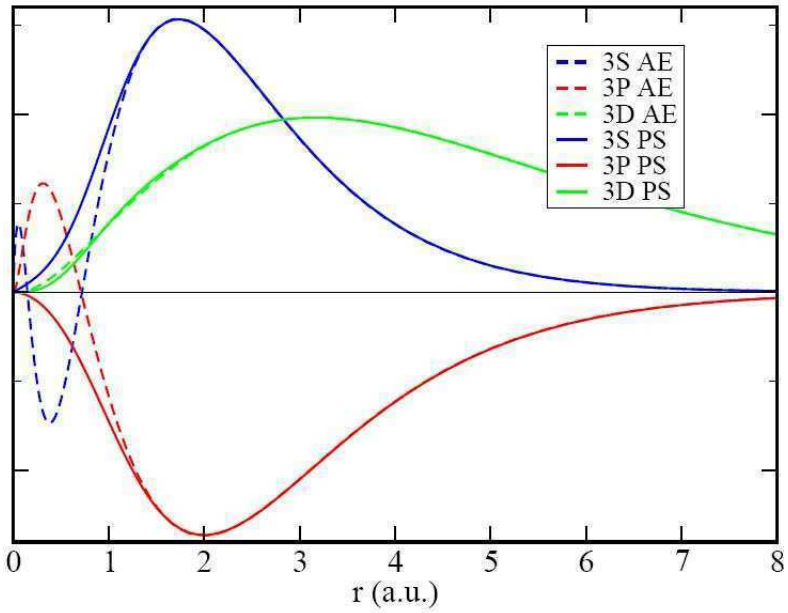

Figure 2.1. All-electron wavefunctions (AE) and pseudo-wavefunctions (PS) obtained for the silicon atom. The 3D state is an excited wavefunction. Data taken from *P. Gianozzi Notes*, reference [21].

were adopted in the calculations of this thesis.

2.2.3 Plane Wave basis sets

Bloch´s theorem establishes that the eigenstates $\psi_{\mathbf{k}}(\mathbf{r})$ of a Hamiltonian $\hat{H} = \hat{T} + \hat{U}$ have the form

$$\psi_{\mathbf{k}}(\mathbf{r}) = e^{i\mathbf{k}\cdot\mathbf{r}} u_{\mathbf{k}}(\mathbf{r}) \tag{2.61}$$

where $u(\mathbf{r}) = u(\mathbf{r} + \mathbf{R})$ for $\mathbf{R}$ in a Bravais lattice. On the other hand, any periodic function in the real space can be expressed as a sum:

$$u_{\mathbf{k}}(\mathbf{r}) = \sum_{\mathbf{G}} C_{\mathbf{k}}(\mathbf{G}) e^{i\mathbf{G}\cdot\mathbf{r}} \tag{2.62}$$

where the $\mathbf{G}$ vectors are the reciprocal lattice vectors ($\mathbf{G} = n_1\mathbf{b}_1 + n_2\mathbf{b}_2 + n_3\mathbf{b}_3$), and $C_{\mathbf{k}}(\mathbf{G})$ the Fourier coefficients. Combining these last two equations, the wave function can be expressed as:

$$\psi_{\mathbf{k}}(\mathbf{r}) = \frac{e^{i\mathbf{k}\cdot\mathbf{r}}}{\sqrt{\Omega}} \sum_{\mathbf{G}=0}^{\infty} C_{\mathbf{k}}(\mathbf{G}) e^{i\mathbf{G}\cdot\mathbf{r}} \tag{2.63}$$

where $1/\Omega$ was added as a normalization factor. In this way, the plane waves (PW) basis functions can be singled out,

$$\phi_{\mathbf{G}} = \frac{1}{\sqrt{\Omega}} e^{i\mathbf{G}\cdot\mathbf{r}} \tag{2.64}$$

so that $\{\phi_{\mathbf{G}}\}$ conforms an orthonormal basis set, $\langle\phi_{\mathbf{G}}|\phi_{\mathbf{G}'}\rangle = \delta_{\mathbf{G},\mathbf{G}'}$. For a polielectronic system, if we label with the index *j* each of the eigenstates, equation 2.63 becomes:

$$\psi_{\mathbf{k},j}(\mathbf{r}) = e^{i\mathbf{k}\cdot\mathbf{r}} \sum_{\mathbf{G}=0}^{\infty} C_{j\mathbf{k}}(\mathbf{G})\phi_{\mathbf{G}}(\mathbf{r}) = \sum_{\mathbf{G}=0}^{\infty} C_{j\mathbf{k}}(\mathbf{G})\phi_{\mathbf{G}}^{\mathbf{k}}(\mathbf{r}) \tag{2.65}$$

where in the last expression the phase factor $e^{i\mathbf{k}\cdot\mathbf{r}}$ was incorporated to the basis functions. Now, if we insert this basis in the integral form of the Kohn-Sham equations (2.44), we arrive to the following set of equations:

$$\sum_{\mathbf{G}'} (H_{\mathbf{G},\mathbf{G}'}^{(\mathbf{k})} - \varepsilon_j^{(\mathbf{k})} S_{\mathbf{G},\mathbf{G}'}^{(\mathbf{k})}) c_j^{(\mathbf{k})}(\mathbf{G}') = 0 \tag{2.66}$$

where $S_{\mathbf{G},\mathbf{G}'} = \delta_{\mathbf{G},\mathbf{G}'}$, and $H_{\mathbf{G},\mathbf{G}'}^{(\mathbf{k})} = T_{\mathbf{G},\mathbf{G}'}^{(\mathbf{k})} + V_{\mathbf{G},\mathbf{G}'}^{(\mathbf{k})}$. We note that there is one of these equations for every possible value of **G**, j, and **k**. The matrix elements of the kinetic and potential operators assume in atomic units the following form:

$$T_{\mathbf{G},\mathbf{G}'}^{\mathbf{k}} = -\left\langle \phi_{\mathbf{G}}^{k} | \frac{1}{2}\nabla^2 | \phi_{\mathbf{G}'}^{k} \right\rangle = \frac{1}{2}|\mathbf{k}+\mathbf{G}|^2 \delta_{\mathbf{G},\mathbf{G}'} \tag{2.67}$$

$$V_{\mathbf{G},\mathbf{G}'}^{\mathbf{k}} = \left\langle \phi_{\mathbf{G}}^{k} | \hat{V} | \phi_{\mathbf{G}'}^{k} \right\rangle = \frac{1}{\Omega}\int V(\mathbf{r}) e^{-i(\mathbf{G}-\mathbf{G}')\cdot\mathbf{r}} d\mathbf{r} = \tilde{V}(\mathbf{G}-\mathbf{G}') \tag{2.68}$$

In this way, the kinetic energy is a diagonal matrix in a PW representation. On the other hand, the elements of the potential energy operator matrix, $\tilde{V}(\mathbf{G}-\mathbf{G}')$, are the Fourier transforms of the potential in real space, which can have different functional forms depending on the pseudopotential method. Therefore, the Kohn-Sham equations 2.66 can be reduced to:

$$\sum_{\mathbf{G}'} \left(\frac{1}{2}|\mathbf{k}+\mathbf{G}|^2 \delta_{\mathbf{G},\mathbf{G}'} + \tilde{V}(\mathbf{G}-\mathbf{G}') \right) C_{j\mathbf{k}}(\mathbf{G}') = \varepsilon_{j\mathbf{k}} C_{j\mathbf{k}}(\mathbf{G}) \tag{2.69}$$

PW energy cutoff The number of **G**′ reciprocal lattice vectors entering the expansion 2.63 are in principle infinite, but in practice the sum must contain a finite number of terms. The Fourier coefficients $C_{\mathbf{k}}(\mathbf{G})$ can be computed from the scalar product of the corresponding basis element and the eigenfunction:

$$C_{j\mathbf{k}}(\mathbf{G}) = \int_{\Omega} \phi_{\mathbf{G}}^{\mathbf{k}*}(\mathbf{r})\psi_{\mathbf{k},j}(\mathbf{r})d\mathbf{r} = \frac{1}{\sqrt{\Omega}} \int_{\Omega} e^{-i(\mathbf{k}+\mathbf{G})\cdot\mathbf{r}}\psi_{\mathbf{k},j}(\mathbf{r})d\mathbf{r} \tag{2.70}$$

from where it is seen that the coefficients of the wavefunctions tend to decrease with increasing $|\mathbf{k}+\mathbf{G}|$. Then, it is reasonable to select the **G** vectors in the PW expansion so that the kinetic energy of the basis functions be lower than a given energy cutoff E_{cut}:

$$|\mathbf{k}+\mathbf{G}|^2 < E_{cut} \tag{2.71}$$

This truncation leads to an error in the computed physical quantities, which can be variationally reduced as the E_{cut} is increased. All the periodic functions, such as electronic density (ρ), the external potential (v_{ext}(**r**)), or the other components of the Kohn-Sham potential, can be represented as Fourier series with a PW basis set. As shown in equation 2.53, the electronic density is constructed by squaring the wavefunction in the real space, and consequently the number of **G** vectors in the expansion of ρ is twice as many, $|\mathbf{G}| = 2G_{cut}$. Then, the energy cutoff fot the expansion of the charge density is $E_D = 4E_{cut}$.

Advantages and disadvantages of plane waves One of the major advantages of this kind of basis set is the fact that the kinetic term in the one-electron Hamiltonian is diagonal in reciprocal space, and therefore straightforward to calculate, while the potential is local in real space, independent of the **k** vector of the BZ. It has to be mentioned that the algorithm that transforms functions from reciprocal to real space and viceversa, known as *Fast Fourier Transform* technique, is extremely efficient in terms of computational cost. Other advantages lie on the simplicity gained in the calculation of the energy and its derivates, such as the forces. Aside from the numerical advantages, PW represent all space with same accuracy, at variance with localized basis, which impose a bias toward the regions where they are centered. Plane waves are extended in all space, and so are the natural basis for periodic systems. Finally, a remarkable virtue is that they are free from the basis set superposition error (BSSE) [29, 30], which is inherent to localized basis set such as gaussians.

When systems with low dimensionality, such as surfaces, polymers or molecules, are described within this framework, the direction where the system is not periodic is filled with vacuum in the unit cell in order to avoid the interaction between replicas. In such cases there is a loss of computational resources in describing the vacuum. One the other hand, systems with regions in which the wave functions vary rapidly need a great amount of PW basis functions to describe properly the high-frequency modes. At last, in principle no charged systems can be represented in this framework due to the divergent Coulomb interaction between replicas, although this limitation actually arises from the periodical

symmetry rather than from the nature of the basis. This problem, however, is avoided through the addition of a compensating background charge.

2.2.4 The pseudopotential plane wave method

In this section we will examine the practical implementation of the previous artifacts in an efficient electronic structure method for extended systems, known generically as the pseudopotential plane wave method (PPW) [4, 31]. Within this framework the KS equations expanded in plane waves are given by expression 2.69, with the potential replaced by $v_{KS}[\rho]$ as defined in 2.42:

$$\sum_{\mathbf{G}'} \left(\frac{1}{2} |\mathbf{k} + \mathbf{G}|^2 \delta_{\mathbf{G},\mathbf{G}'} + v_{KS}[\rho](\mathbf{G} - \mathbf{G}') \right) C_{j\mathbf{k}}(\mathbf{G}') = \varepsilon_{j\mathbf{k}} C_{j\mathbf{k}}(\mathbf{G}) \tag{2.72}$$

This replacement introduces the need for a self-consistent solution, because the KS potential $v_{KS}[\rho]$ depends on the electronic density and therefore on $C_{j\mathbf{k}}$. In a DFT-pseudopotential framework the KS potential is written as:

$$\hat{v}_{KS}[\rho] = \left\{ v_{PS}^{loc}(\mathbf{r}, \mathbf{R}) + v_H[\rho(\mathbf{r})] + v_{XC}[\rho(\mathbf{r})] \right\} \hat{I} + \sum_{l=0}^{l_{max}} \Delta v_{PS}^{l}(r) \hat{P}_l \tag{2.73}$$

The first term on the right hand side of the above equation, $v_{PS}^{loc}(\mathbf{r}, \mathbf{R})$, represents the local pseudopotential contribution with **R** referring to the atomic positions. The second term $v_H[\rho(\mathbf{r})]$ denotes the Hartree or Coulombic potential, which, as will be discussed, is a function of ρ. $v_{XC}[\rho(\mathbf{r})]$ accounts for the exchange correlation, which is also function of ρ. Both, the second and third terms, arise from the electron-electron interaction. $\Delta v_{PS}^{l}(r)$ is the non-local part of the pseudopotential, which is neither local in reciprocal space nor in real space.

Energy functional The energy per unit cell can be partitioned in the following terms:

$$E_{KS}[\rho] = T_e[\rho] + E_H[\rho] + E_{XC}[\rho] + E_{ii} + E_{PS}^{nl} + E_{PS}^{loc}[\rho] \tag{2.74}$$

where $T_e[\rho]$ represents the kinetic energy, $E_H[\rho]$ the electrostatic repulsion between electrons, and $E_{XC}[\rho]$ the exchange correlation energy . E_{ii} is the ion-ion interaction, i.e., the electrostatic repulsion between the pseudo-cores (ions). $E_{PS}^{loc}[\rho]$ and E_{PS}^{nl} account for the electron-ion attraction.

Due to the long-range decay of electrostatic interactions, the Coulomb energy of a non-neutral arrange of periodic charges diverges. For this reason, $E_H[\rho]$, $E_{PS}^{loc}[\rho]$ and E_{ii} diverge if they are calculated separately. A converged value can be obtained only when the

electrostatic energy is computed for the overall neutral system of ions and electrons. The electrostatic contribution is:

$$E_{es}[\rho] = E_H[\rho] + E_{PS}^{loc}[\rho] + E_{ii}$$
$$= \frac{1}{2}\iint \frac{\rho(\mathbf{r})\rho(\mathbf{r'})}{|\mathbf{r}-\mathbf{r'}|}d\mathbf{r}d\mathbf{r'} + \sum_{s=1}^{N_s}\sum_{l=1}^{P_s}\int \rho(\mathbf{r})v_{PS}^{loc,s}(|\mathbf{r}-\mathbf{R}_I|)d\mathbf{r} + \frac{1}{2}\sum_{I=1}^{P}\sum_{J=1,J\neq I}^{P}\frac{Z_I Z_J}{|\mathbf{R}_I-\mathbf{R}_J|} \quad (2.75)$$

where $\rho(\mathbf{r})$ is the electronic charge distribution, s runs over the atomic species, N_s is the total number of species, P_s is the number of atoms for the s atomic species, and P is the total number of ions. $v_{PS}^{loc,s}$ is the local part of the pseudopotential for each s species. Z_I is the ionic charge and $\mathbf{R}_I$ its location. For computational convenience, in computer implementations the electronic charge is often taken as positive and the ionic charge as negative.

In order to arrive to the final equations in PBC, an auxiliary continuous charge distribution $\rho_\alpha(\mathbf{r})$ associated with the nuclear subsystem is added to the Hartree energy term and substructed from the other two. In this way, a total neutral charge density is defined, $\rho_T(\mathbf{r}) = \rho_\alpha(\mathbf{r}) + \rho(\mathbf{r})$, and the electrostatic energy can be rewritten as:

$$E_{es}[\rho] = \frac{1}{2}\iint \frac{\rho_T(\mathbf{r})\rho_T(\mathbf{r'})}{|\mathbf{r}-\mathbf{r'}|}d\mathbf{r}d\mathbf{r'} + \int \rho(\mathbf{r})\left(\sum_{s=1}^{N_s}\sum_{l=1}^{P_s} v_{PS}^{loc,s}(|\mathbf{r}-\mathbf{R}_I|)d\mathbf{r} - \int \frac{\rho_\alpha(\mathbf{r'})}{|\mathbf{r}-\mathbf{r'}|}\right)d\mathbf{r}$$
$$+\frac{1}{2}\left(\sum_{I=1}^{P}\sum_{J=1,J\neq I}^{P}\frac{Z_I Z_J}{|\mathbf{R}_I-\mathbf{R}_J|} - \iint \frac{\rho_\alpha(\mathbf{r})\rho_\alpha(\mathbf{r'})}{|\mathbf{r}-\mathbf{r'}|}d\mathbf{r}d\mathbf{r'}\right) \quad (2.76)$$

Introducing the following definitions:

$$\tilde{E}_H[\rho] = \frac{1}{2}\iint \frac{\rho_T(\mathbf{r})\rho_T(\mathbf{r'})}{|\mathbf{r}-\mathbf{r'}|}d\mathbf{r}d\mathbf{r'} \quad (2.77)$$

$$\tilde{E}_{PS}^{loc}[\rho] = \int \rho(\mathbf{r})\left(\sum_{s=1}^{N_s}\sum_{l=1}^{P_s} v_{PS}^{loc,s}(|\mathbf{r}-\mathbf{R}_I|)d\mathbf{r} - \int \frac{\rho_\alpha(\mathbf{r'})}{|\mathbf{r}-\mathbf{r'}|}\right)d\mathbf{r} \quad (2.78)$$

$$\tilde{E}_{ii} = \frac{1}{2}\left(\sum_{I=1}^{P}\sum_{J=1,J\neq I}^{P}\frac{Z_I Z_J}{|\mathbf{R}_I-\mathbf{R}_J|} - \iint \frac{\rho_\alpha(\mathbf{r})\rho_\alpha(\mathbf{r'})}{|\mathbf{r}-\mathbf{r'}|}d\mathbf{r}d\mathbf{r'}\right) \quad (2.79)$$

the electrostatic energy turns out to be the sum of all three, $E_{es}[\rho] = \tilde{E}_H[\rho] + \tilde{E}_{PS}^{loc}[\rho] + \tilde{E}_{ii}$. The first of these terms can be expressed as a sum in reciprocal space using the following relation arising from the convolution theorem:

$$\int \frac{\rho_T(\mathbf{r'})}{|\mathbf{r}-\mathbf{r'}|} d\mathbf{r'} = \sum_{\mathbf{G}} \tilde{\rho}_T(\mathbf{G}) \frac{4\pi}{G^2} e^{i\mathbf{G}\cdot\mathbf{r}} \tag{2.80}$$

where $\tilde{\rho}_T(\mathbf{G})$ is the Fourier transform of $\rho(\mathbf{r})$. The divergent term of $\mathbf{G} = 0$ is avoided thanks to the electroneutrality of the system, $\tilde{\rho}_T(\mathbf{G} = 0) = \dfrac{Q_T}{\Omega}$, and as a consequence equation 2.77 becomes:

$$\tilde{E}_H[\rho] = \frac{1}{2} \iint \frac{\rho_T(\mathbf{r})\rho_T(\mathbf{r'})}{|\mathbf{r}-\mathbf{r'}|} d\mathbf{r} d\mathbf{r'} = \frac{\Omega}{2} \sum_{\mathbf{G}\neq\mathbf{0}} \frac{4\pi}{G^2} \tilde{\rho}_T(\mathbf{G}) \tilde{\rho}_T(\mathbf{\text{-}G}) \tag{2.81}$$

To work out expression 2.78, we resort to the convolution theorem again, which states that

$$\int \rho(\mathbf{r}) v_{PS}^{loc,s}(|\mathbf{r}-\mathbf{R}_I|) d\mathbf{r} = \Omega \sum_{\mathbf{G}} e^{i\mathbf{G}\cdot\mathbf{R}_I} \tilde{v}_{PS}^{loc,s}(G) \tilde{\rho}(-\mathbf{G}) \tag{2.82}$$

If we define an atomic structure factor for each species s,

$$S_s(\mathbf{G}) = \sum_{I=1}^{P_s} e^{-i\mathbf{G}\cdot\mathbf{R}_I^s} \tag{2.83}$$

where $\mathbf{R}_I^s$ are the positions of the atoms belonging to that species (and P_s, as before, the number of atoms of each species), then we can get $\tilde{E}_{PS}^{loc}[\rho]$ as a function of $\mathbf{G}$ by combining expressions 2.81, 2.82 and 2.83:

$$\tilde{E}_{PS}^{loc}[\rho] = \Omega \sum_{\mathbf{G}} \left[\sum_{s=1}^{N_s} S_s(\mathbf{G}) \tilde{v}_{PS}^{loc,s}(G) - \frac{4\pi}{G^2} \tilde{\rho}_\alpha(\mathbf{G}) \right] \tilde{\rho}(-\mathbf{G}) \tag{2.84}$$

The $\mathbf{G} = 0$ term requires careful consideration. It does not diverge, but it is not zero as it was for equation 2.81. First, we notice that $S_s(0) = P_s$ and $\tilde{\rho}_\alpha(0) = -Q/\Omega$, with Q the total electronic charge. As $\tilde{\rho}_\alpha(G)$ is multiplied by $4\pi/G^2$, we expand $\tilde{\rho}_\alpha(G)$ around $\mathbf{G} = 0$ up to terms of G^2: $\tilde{\rho}_\alpha(G) = \tilde{\rho}_\alpha(0) + \tilde{\rho}''_\alpha(0)$, where $\tilde{\rho}''_\alpha(0)$ is the second derivative evaluated at $\mathbf{G} = 0$. Then, the $\mathbf{G} = 0$ term of equation 2.84 can be written as:

$$\lim_{G\to 0} \left[\Omega \sum_{s=1}^{N_s} P_s \tilde{v}_{PS}^{loc,s}(G) + \frac{4\pi Q}{G^2} \right] \tilde{\rho}(G) - 2\pi\Omega \tilde{\rho}''_\alpha(0) \tilde{\rho}(0) \tag{2.85}$$

Moreover, noting that $v_{PS}^{loc,s}(r) = -Z_s/r$ for $r > r_c$, the Fourier transform of the local part of the PS can be expressed as

$$\begin{aligned}\tilde{v}_{PS}^{loc,s}(G) =& \frac{1}{\Omega}\int_{\Omega} v_{PS}^{loc,s}(r)e^{-i\mathbf{G}\cdot\mathbf{r}}d\mathbf{r} \\ =& \frac{1}{\Omega}\left[\int_{\Omega_c} v_{PS}^{loc,s}(r)e^{-i\mathbf{G}\cdot\mathbf{r}}d\mathbf{r} + \int_{\Omega-\Omega_c} v_{PS}^{loc,s}(r)e^{-i\mathbf{G}\cdot\mathbf{r}}d\mathbf{r}\right] \\ =& \frac{1}{\Omega}\left[\int_{\Omega_c} v_{PS}^{loc,s}(r)e^{-i\mathbf{G}\cdot\mathbf{r}}d\mathbf{r} - \int_{\Omega-\Omega_c} \frac{Z_s}{r}e^{-i\mathbf{G}\cdot\mathbf{r}}d\mathbf{r}\right] \end{aligned} \tag{2.86}$$

where Ω_c is the volume of the pseudized region. Adding and substracting $1/\Omega\int_{\Omega_c} Z_s/re^{-i\mathbf{G}\cdot\mathbf{r}}d\mathbf{r}$ we have

$$\tilde{v}_{PS}^{loc,s}(G) = \frac{1}{\Omega}\left[\int_{\Omega_c}\left(v_{PS}^{loc,s}(r) + \frac{Z_s}{r}\right)e^{-i\mathbf{G}\cdot\mathbf{r}}d\mathbf{r} + -\int_{\Omega}\frac{Z_s}{r}e^{-i\mathbf{G}\cdot\mathbf{r}}d\mathbf{r}\right] \tag{2.87}$$

The second term of the rigth hand side of 2.87 is the Fourier transform of $-Z_s/r$ and equals $-4\pi Z_s/\Omega G^2$. Then, if the integral on Ω_c in 2.87 is denoted by $\Delta\tilde{v}_{PS}^{loc,s}$ for $\mathbf{G} = 0$, the term corresponding to $\mathbf{G} = 0$ in equation 2.84 can be written as:

$$\sum_{s=1}^{N_s} P_s\Delta\tilde{v}_{PS}^{loc,s}\tilde{\rho}(0) + \lim_{G\to 0}\left[-\sum_{s=1}^{N_s} P_s Z_s + Q\right]\frac{4\pi}{G^2}\tilde{\rho}(0) - 2\pi\Omega\tilde{\rho}_{\alpha}''(0)\tilde{\rho}(0) \tag{2.88}$$

The sum of the charge of each species times the number of atoms per species amounts to the total charge, and therefore the second term in equation 2.88 must vanish, thus getting rid of the divergence for $\mathbf{G} = 0$. At last, substituting $\tilde{\rho}(0)$ by Q/Ω, equation 2.78 achieves its final expression:

$$\begin{aligned}\tilde{E}_{PS}^{loc}[\rho] = \Omega\sum_{\mathbf{G}\neq\mathbf{0}}\left[\sum_{s=1}^{N_s} S_s(\mathbf{G})\tilde{v}_{PS}^{loc,s}(G) - \frac{4\pi}{G^2}\tilde{\rho}_{\alpha}(\mathbf{G})\right]\tilde{\rho}(-\mathbf{G}) \\ + \frac{Q}{\Omega}\sum_{s=1}^{N_s} P_s\Delta\tilde{v}_{PS}^{loc,s} - 2\pi Q\tilde{\rho}_{\alpha}''(0)\end{aligned} \tag{2.89}$$

Ewald sum Equation 2.79 involves the computation of the Coulomb energy of a periodic arrange of point-like particles. Since this non-neutral summation diverges in PBC, a usual procedure is to include in the sum the ionic auxiliary distribution $\rho_{\alpha}(\mathbf{r})$, so as to impose neutrality, that is, the self-interaction of the density $\rho_{\alpha}(\mathbf{r})$ is substracted to the ionic interaction to exactly cancel out the total charge. In 1917, Ewald developed a mathematical scheme to compute this infinite sum [32]. The idea behind the Ewald method is to screen the long-range Coulomb interactions between the point-like particles by surrounding each of them by a diffusive charge distribution of the opposite sign, so that the total charge of this cloud exactly cancels each point charge. The advantage of this scheme lies on the fact

that the interactions between the point-like particles decay more rapidly due to the screening of the diffuse charge distribution. This can be simply a gaussian distribution ($\rho_{gauss,\alpha}$). Then, an equivalent distribution but of opposite charge ($-\rho_{gauss,\alpha}$) must be included in the sum in order to counteract the effect of $\rho_{gauss,\alpha}$. A possible definition for the auxiliary gaussian charge is:

$$\rho_{gauss,\alpha}(\mathbf{r}) = -\frac{\eta^3}{\pi^{3/2}} \sum_{I=1}^{P} Z_I e^{-2\eta^2|\mathbf{r}-\mathbf{R}_I|^2} \tag{2.90}$$

where $1/\eta$ is a cutoff distance. With this definition, each term in the sum 2.90 contributes with a charge Z_I. The corresponding Fourier transform is:

$$\tilde{\rho}_{gauss,\alpha}(\mathbf{G}) = -\frac{1}{\Omega} e^{-G^2/8\eta^2} \left(\sum_{s=1}^{N_s} Z_s S_s(\mathbf{G}) \right) \tag{2.91}$$

Then the electrostatic interaction of $\rho_{gauss,\alpha}$ and the point charges Z_I can be calculated as:

$$\frac{1}{2} \sum_I \int \frac{\rho_{gauss,\alpha}(\mathbf{r})}{|\mathbf{R}_I - \mathbf{r}|} d\mathbf{r} Z_I = \frac{1}{2\Omega} \sum_{\mathbf{G}} \frac{4\pi}{G^2} e^{G^2/4\eta^2} \left| \sum_s Z_s S_s(\mathbf{G}) \right|^2 \tag{2.92}$$

where the integral on the left hand side represents the electrostatic potential of the gaussian distribution. This electrostatic energy includes the interaction between the cloud of charge Z_I and the point charge Z_I located at the center of the gaussian, which we call E_{self}, and which turns out to be independent of the atomic positions $\mathbf{R}_I$.

$$E_{self} = \frac{\eta}{\sqrt{\pi}} \sum_{I=1}^{P} Z_I^2 \tag{2.93}$$

Eventually, this self-interaction term needs to be substructed from the energy. There is also the electrostatic interaction of the point charges screened by the gaussians of opposite sign. This screening kills the long-range tails of the point charge potential, giving instead a short-ranged interaction. Such a screened electrostatic potential is:

$$\phi_{short-range} = \frac{Z_I}{r} - \int \frac{\rho_{gauss,\alpha}(\mathbf{r})}{|\mathbf{R}_I - \mathbf{r}|} d\mathbf{r} = \frac{Z_I}{r} - \frac{Z_I}{r} erf(\sqrt{2\eta} r) = \frac{Z_I}{r} erfc(\sqrt{2\eta} r) \tag{2.94}$$

from which the corresponding electrostatic energy can be calculated:

$$E_{short-range} = \frac{1}{2} \sum_{I=1}^{P} \sum_{J \neq 1}^{P} Z_I Z_J \left[\sum_{m=-\infty}^{\infty} \frac{erfc(|\mathbf{R}_I + mL - \mathbf{R}_J|\eta)}{|\mathbf{R}_I + mL - \mathbf{R}_J|} \right] \tag{2.95}$$

where the m index accounts for the cell number. The short-ranged nature of this interaction ensures that the sum converges in very few terms: typically, only first neighbours need to be considered. As a result, the electrostatic energy associated with the point charges interaction contains sums in both real and reciprocal space:

$$E_{ii} = \frac{1}{2}\sum_{I=1}^{P}\sum_{J\neq 1}^{P} Z_I Z_J \left[\sum_{m=-\infty}^{\infty} \frac{erfc(|\mathbf{R}_I + mL - \mathbf{R}_J|\eta)}{|\mathbf{R}_I + mL - \mathbf{R}_J|}\right]$$
$$+\frac{1}{2\Omega}\sum_{\mathbf{G}} \frac{4\pi}{G^2} e^{G^2/4\eta^2} \left|\sum_s Z_s S_s(\mathbf{G})\right|^2 - \frac{\eta}{\sqrt{\pi}}\sum_{I=1}^{P} Z_I^2 \tag{2.96}$$

Yet, this expression diverges because it corresponds to a non-neutral charge distribution. Therefore, it is combined with the self-interaction energy of the auxiliary charge density $\rho_\alpha(\mathbf{r})$, so that now the definition in 2.79 makes sense:

$$\frac{1}{2}\iint \frac{\rho_\alpha(\mathbf{r})\rho_\alpha(\mathbf{r'})}{|\mathbf{r}-\mathbf{r'}|} d\mathbf{r} d\mathbf{r'} = \frac{\Omega}{2}\sum_{\mathbf{G}\neq\mathbf{0}} \frac{4\pi}{G^2}\tilde{\rho}_\alpha(\mathbf{G})\tilde{\rho}_\alpha(\mathbf{-G}) \tag{2.97}$$

$$\tilde{E}_{ii} = \frac{1}{2}\sum_{I=1}^{P}\sum_{J\neq 1}^{P} Z_I Z_J \left[\sum_{m=-m_{max}}^{m_{max}} \frac{erfc(|\mathbf{R}_I + mL - \mathbf{R}_J|\eta)}{|\mathbf{R}_I + mL - \mathbf{R}_J|}\right]$$
$$+\frac{1}{2\Omega}\sum_{\mathbf{G}\neq\mathbf{0}} \frac{4\pi}{G^2}\left[e^{G^2/4\eta^2}\left|\sum_s Z_s S_s(\mathbf{G})\right|^2 - \Omega^2|\tilde{\rho}_\alpha(\mathbf{G})|^2\right]$$
$$-\frac{\eta}{\sqrt{\pi}}\sum_{l=1}^{P} Z_I^2 - \frac{\pi Q^2}{2\Omega\eta^2} - 2\pi\Omega\tilde{\rho}''_\alpha(0)\tilde{\rho}_\alpha(0) \tag{2.98}$$

If ρ_α is the same as $\rho_{\alpha,gauss}$, then $\tilde{\rho}_\alpha(\mathbf{G}) = -1/\Omega e^{-G^2/8\eta^2}\left(\sum Z_s S_s(\mathbf{G})\right)$, and the middle term on the right hand side of the last equation vanishes. In conclusion, gathering all the contributions 2.81, 2.89 and 2.98, the following expression is achieved for the total electrostatic energy:

$$E_{es}[\rho] = \frac{\Omega}{2}\sum_{\mathbf{G}\neq 0}\frac{4\pi}{G^2}\tilde{\rho}_T(\mathbf{G})\tilde{\rho}_T(-\mathbf{G}) + \Omega\sum_{\mathbf{G}\neq 0}\sum_{s=1}^{N_s} S_s(\mathbf{G})\tilde{u}_{PS}^{loc,s}(G)\tilde{\rho}(-\mathbf{G})$$
$$+\frac{1}{2}\sum_{I=1}^{P}\sum_{J\neq 1}^{P} Z_I Z_J \left[\sum_{m=-m_{max}}^{m_{max}} \frac{erfc(|\mathbf{R}_I + mL - \mathbf{R}_J|\eta)}{|\mathbf{R}_I + mL - \mathbf{R}_J|}\right]$$
$$-\frac{\eta}{\sqrt{\pi}}\sum_{I=1}^{P} Z_I^2 - \frac{Q}{\Omega}\left(\sum_{s=1}^{N_s} P_s \Delta\tilde{v}_{PS}^{loc,s} + \frac{\pi Q}{2\eta^2}\right) \tag{2.99}$$

where the function $u_{PS}^{loc,s}$ is equal to the local pseudopotential plus the potential of the

ionic charge:

$$u_{PS}^{loc,s}(r) = v_{PS}^{loc,s}(r) - \frac{Z_I}{r} erf(\sqrt{2\eta} r) \tag{2.100}$$

$$\tilde{u}_{PS}^{loc,s} = \tilde{v}_{PS}^{loc,s}(G) + \frac{4\pi}{G^2}\frac{Z_s}{\Omega} e^{-G^2/8\eta^2} \tag{2.101}$$

In this treatment special attention was payed to the electrostatic interaction due to the known divergence of Coulomb interactions in infinite systems. The electrostatic energy accounts for three of the six terms in equation 2.74: $E_H[\rho]$, $E_{PS}^{loc}[\rho]$ and E_{ii}. The kinetic energy term, on the other hand, can be computed in terms of the PW coefficients $C_{i\mathbf{k}}(\mathbf{G})$:

$$T_e[\rho] = \sum_{\mathbf{k}\epsilon BZ} \omega_{\mathbf{k}} \sum_{i=1}^{N_{\mathbf{k}}} f_i^{(\mathbf{k})} \sum_{\mathbf{G}} |\mathbf{k}+\mathbf{G}|^2 |C_{i\mathbf{k}}(\mathbf{G})|^2 \tag{2.102}$$

where $N_{\mathbf{k}}$ is the number of electronic states occupied at each **k**-point, and $f_i^{(\mathbf{k})}$ is the occupation number of band *i* at wave vector **k**. Finally, the exchange correlation term is calculated by numerically integrating the exchange correlation energy density in real space:

$$E_{XC}(\mathbf{G}) = \frac{\Omega}{N_R} \sum_{n=1}^{N_R} \rho(\mathbf{r}_n) \epsilon_{XC}[\rho(\mathbf{r}_n)] \tag{2.103}$$

where N_R indicates the number of mesh points, and r_n are the spatial coordinates associated with each point.

Derivation of a final expression for the non-local pseudopotential energy is arduous because of its dependence on the angular momentum. In principle it can be computed in real or in reciprocal space, depending on the specific electronic structure computational package. The mathematics behind this contribution is complicated and is considered beyond the scope of this thesis.

The PPW methodology presented in this section is implemented in several computational packages, such as the *PWscf-Quantum Espresso* [33] and the *VASP* [34–36] codes. In recent years it has become the main tool to study extended systems as solids and surfaces from first-principles.

2.3 Born Oppenheimer Molecular Dynamics

The PPW electronic method can be used to follow the evolution of an atomistic system in real time. First-principles molecular dynamics (MD) can then be performed under the *Born-Oppenheimer* (BO) approximation:

$$M\frac{d^2\mathbf{R}(t)}{dt^2} = -\nabla\varepsilon(\mathbf{R}) \tag{2.104}$$

where $\mathbf{R}$ represents the atomic coordinates, and $\varepsilon(\mathbf{R})$ the adiabatic *potential energy surface* (PES). The points on this surface (or the values of $\varepsilon(\mathbf{R})$) are computed quantum-mechanically for a fixed configuration of the nuclei, $\{\mathbf{R}_I\}$. In doing this, it is assumed that the electronic degrees of freedom adapt instantaneously to the nuclear coordinates $\{\mathbf{R}_I\}$. This is equivalent to decouple the electronic and ionic coordinates, defining an electronic wavefunction with a parametrical dependence on the nuclear coordinates. In this framework, the atoms are treated as classical objects following a Newtonian dynamics, but subject to the quantum-mechanical forces of the electrons. Such is the adiabatic or *Born Oppenheimer* approximation [4, 31], which has proved to be highly accurate to describe the molecular dynamics of most atomistic systems. The approximation declines for light nuclei at low temperatures, where the De Broglie wave lengths of the nuclei may not be negligible compared to that of the electrons.

Geometry minimizations (or geometry optimizations) consist in finding the atomic coordinates that minimize the system energy. For the initial atomic configuration, in the context of density functional theory, the KS equations are solved through a variational scheme and the PW coefficients are obtained. The forces are calculated and the coordinates are updated according to a minimization algorithm, to start a new calculation of the energy. This cycle proceeds until the forces are negligible and the energy is minimized, reaching the minimum of the PES and the optimized geometry, solution of the stationary problem $\nabla\varepsilon_n(\mathbf{R}) = 0$. On the other hand, Born-Oppenheimer molecular dynamics (BO-MD) consists in evolving the atomic coordinates according to the classical equations of motion 2.104. For each geometry configuration the KS equations are equally solved to obtain the energy and forces, which in this case are used to feed equation 2.104 and generate trajectories of the atoms in space and time. Normally, to sample a meaningful time window, many more configurations (and electronic structure minimization cycles) are involved in a molecular dynamics simulation than in the optimization of a geometry. The typical numbers of steps in a single MD simulation can be of several thousands. First-principles MD simulations are costly, but useful to study mechanisms and to understand chemical processes involving rupture and/or creation of chemical bonds.

Equation 2.104 can be expressed in terms of the electronic wavefunctions $\psi(\mathbf{R})$ thanks to the Hellmann-Feynman theorem [37, 38],

$$M\frac{d^2\mathbf{R}(t)}{dt^2} = -\left\langle \psi(\mathbf{R}) \left| \frac{\partial \hat{H}}{\partial \mathbf{R}_I} \right| \psi(\mathbf{R}) \right\rangle \tag{2.105}$$

where $\mathbf{R}$ represents the classical nuclear configuration, and:

$$\left\langle \psi(\mathbf{R})|\hat{H}|\psi(\mathbf{R})\right\rangle = E_{KS}[\rho](\mathbf{R}) = T_R[\rho] + \frac{1}{2}\int \frac{\rho(\mathbf{r})\rho(\mathbf{r'})}{|\mathbf{r}-\mathbf{r'}|}d\mathbf{r}d\mathbf{r'} + E_{XC}[\rho]$$
$$+\sum_{I=1}^{P}\int \rho(\mathbf{r})v_{ext}(\mathbf{r}-\mathbf{R}_I)d\mathbf{r} + \frac{1}{2}\sum_{I=1}^{P}\sum_{J\neq I}^{P}\frac{Z_I Z_J}{|\mathbf{R}_I-\mathbf{R}_J|} \tag{2.106}$$

The forces on the nuclear coordinates of atom I are obtained by derivation. Since the first three terms in equation 2.106 do not have an explicit dependence on R_I, only the two last have to be considered in the derivative:

$$\mathbf{F}_I = -\int \rho(\mathbf{r})\frac{\partial v_{ext}(\mathbf{r}-\mathbf{R}_I)}{\partial \mathbf{R}_I}d\mathbf{r} + \sum_{J\neq I}^{P} Z_I Z_J \frac{\mathbf{R}_I-\mathbf{R}_J}{|\mathbf{R}_I-\mathbf{R}_J|^3} \tag{2.107}$$

The most common technique algorithm to evolve (or to numerically integrate) the equations of motion 2.104, is the *Verlet Algorithm*.

Verlet algorithm Once the forces acting on all particles have been computed, the Newton's equations can be integrated. Several algorithms were developed to do this, the simplest and most widely used being the *Verlet Algorithm* [39, 40]. This algorithm is based on the Taylor expansion of the coordinates **r** of a particle around time *t*,

$$\mathbf{r}(t+\Delta t) = \mathbf{r}(t) + \mathbf{v}(t)\Delta t + \frac{\mathbf{F}(t)}{2M}\Delta t^2 + \frac{\Delta t^3}{3!}\frac{d\mathbf{r}}{dt^3} + \mathcal{O}(\Delta t^4) \tag{2.108}$$

where $\mathbf{v}$ is the particle velocity, M its mass, $\mathbf{F}$ the force, and Δt is the integration step, known as the time-step. Similarly,

$$\mathbf{r}(t-\Delta t) = \mathbf{r}(t) - \mathbf{v}(t)\Delta t + \frac{\mathbf{F}(t)}{2M}\Delta t^2 - \frac{\Delta t^3}{3!}\frac{d\mathbf{r}}{dt^3} + \mathcal{O}(\Delta t^4) \tag{2.109}$$

Summing these two equations,

$$\mathbf{r}(t+\Delta t) + \mathbf{r}(t-\Delta t) = 2\mathbf{r}(t) + \frac{\mathbf{F}(t)}{M}\Delta t^2 + \mathcal{O}(\Delta t^4)$$

or:

$$\mathbf{r}(t+\Delta t) \approx 2\mathbf{r}(t) - \mathbf{r}(t-\Delta t) + \frac{\mathbf{F}(t)}{M}\Delta t^2 \tag{2.110}$$

This last approximation leads to an error of 4*th* order in Δt. The velocity, on its part, can be calculated as:

$$\mathbf{v}(t) = \frac{\mathbf{r}(t+\Delta t) - \mathbf{r}(t-\Delta t)}{2\Delta t} + \mathcal{O}(\Delta t^2) \tag{2.111}$$

This expression for the velocity, with an error of a higher order than the one for the

coordinates, is usually only needed for the calculation of the kinetic energy.

The time step is a crucial parameter in a molecular dynamics simulation and has to be carefully selected. If it is too small, the atoms will move too slowly and the simulation will take more time than actually needed. On the other hand if the time step is too large, the integration of the Newton's equation would be not accurate enough, and the energy of the system will diverge after some time. In a microcanonical ensemble, the total energy (kinetic plus potential) must be conserved: therefore the time step can be chosen in a preliminary tests so that energy conservation is verified.

2.4 Car-Parrinello Molecular Dynamics

In 1985, Car and Parrinello [41] proposed a different approach to perform quantum molecular dynamics. Its implementation is known today as the Car Parrinello molecular dynamics (CPMD) scheme [42], which rapidly acquired a great relevance because in many cases it can outperform BO-MD. The idea behind this approach was to exploit the quantum-mechanical adiabatic time scale separation of slow nuclear and fast electronic motions, to transform it into a classical-mechanical adiabatic separation in energy scale. In this way, the energy of the electronic subsystem $\left\langle \varphi_i(\mathbf{r})|\hat{H}|\varphi_i(\mathbf{r})\right\rangle$ is a function of the atomic positions $(\mathbf{R}_I)$ and can be considered to be a functional of some wavefunction $\varphi_i(\mathbf{r})$. In classical dynamics, forces on the nuclei are obtained as a derivation of a Lagrangian with respect to the nuclear positions. Similarly, within CPMD, forces on the orbitals $\varphi_i(\mathbf{r})$ are obtained from the derivation of the CP Lagrangian with respect to these orbitals, thus considered as classical objects. The CPMD Lagrangian assumes the following form:

$$\mathcal{L}_{CP} = \frac{1}{2}\sum_{I=1}^{P} M_I \dot{\mathbf{R}}^2 + \mu \sum_{i=1}^{N} f_i \int |\dot{\varphi}_i(\mathbf{r})|^2 d\mathbf{r} - E_{KS}[\varphi_i(\mathbf{r})](\mathbf{R}) + \sum_{i=1}^{N} f_i \sum_{i=1}^{N} \Lambda_{ij} \left(\int \varphi_i^*(\mathbf{r})\varphi_j(\mathbf{r}) d\mathbf{r} - \delta_{ij} \right) \tag{2.112}$$

where the first and second terms represent the nuclear kinetic energy and the electronic kinetic energy, respectively. The third term is the potential energy of the electrons, and the last contribution arises from an orthonormality constraint applied to the electronic orbitals. Such a constraint is necessary because the dynamics may affect the orthonormality of the $\varphi_i(\mathbf{r})$. μ is known as the fictitious electronic mass, and consists in an adjustable parameter that is tunned to achieve conservative molecular dynamics.

Car-Parrinello equations of motion As it was already mentioned, the equations of motions are obtained from the partial derivates of the CPMD Lagrangian:

$$\frac{d}{dt}\left(\frac{\partial \mathcal{L}_{CP}}{\partial \dot{\mathbf{R}}_I}\right) = -\frac{\partial \mathcal{L}_{CP}}{\partial \dot{\mathbf{R}}_I} \tag{2.113}$$

$$\frac{d}{dt}\left(\frac{\partial \mathcal{L}_{CP}}{\partial \dot{\varphi}_i^*(\mathbf{r})}\right) = -\frac{\partial \mathcal{L}_{CP}}{\partial \dot{\varphi}_i^*(\mathbf{r})} \tag{2.114}$$

Each of these relations leads to the following equations of motion:

$$M_I \ddot{\mathbf{R}}_I = -\frac{\partial E_{KS}[\varphi_i(\mathbf{r})](\mathbf{R})}{\partial \mathbf{R}_I} \tag{2.115}$$

$$\mu \ddot{\varphi}_i(\mathbf{r},t) = -\frac{\partial E_{KS}[\varphi_i(\mathbf{r})](\mathbf{R})}{\partial \varphi_i^*(r)} + \sum_{j=1}^{N} \Lambda_{ij}\varphi_j(\mathbf{r},t) \tag{2.116}$$

These equations must be integrated in time, analogously to equation 2.104, which can be done using an integration technique such as the already discussed *Verlet Algorithm*. In the case of the electronic dynamics, where orbitals must satisfy the orthogonalization condition, and additional algorithm has to be used to force the constraint. This is typically achieved by means of the *SHAKE algorithm* [43].

CPMD performance As it can be seen from equation 2.112, both nuclei and electrons are said to evolve at their own physical temperature, proportional to $\propto \sum_I M_I \dot{\mathbf{R}}_I$ and to $\propto \sum_i \langle \dot{\varphi} | \dot{\varphi} \rangle$ respectively. In the CPMD scheme the conservative quantity during a molecular dynamics simulation in a microcanonical system is: $E_{cons} = K_e + K_n + E_{KS}$, where the first two terms are the kinetic energy of the electronic wavefunctions (not to be confused with $T[\rho]$ of equation 2.31) and of the nuclei. The payoff in the Car-Parrinello approach is in avoiding the need to reach the Born-Oppenheimer (BO) surface for each geometry step. If the starting electronic configuration is already on the BO surface and K_e is kept small during the dynamics, then the oscillations around the BO surface are going to be small too, ensuring that the electronic states be near the BO surface at each step. Actually, two conditions must be satisfied to remain close to the BO surface during a CP molecular dynamics [44]: (1) $K_e \ll K_n$, and (2) the energy exchange between nuclei and orbitals must be minimum. In particular, these two requirements are related. K_e depends on the fictitious mass (μ) and on E_{KS} as a consequence of the nuclei motion which dragg the orbitals with them. On the other hand, the orbitals influence on the nuclei dynamics, through damping it.

The μ parameter controls the energy transfer between nuclei and electrons and also controls the time step. A larger value of μ allows the use of a higher time step. On the other hand, a larger fictitious mass closes the gap between K_e and K_n, incrasing the chances of energy exchange between nuclei and electrons. In consequence, the μ parameter has to be selected carefully, the optimal choice depending on the system.

Within the Car Parrinello approach, quantum molecular dynamics can be performed at a cost which is typically below the cost involved in BO-MD, though this depends on the particular system and implementation. Specifically, this is usually the case for extended systems. The CP method in combination with the PPW scheme has entailed a significant contribution to the field of molecular simulation in condensed matter chemistry and physics. This scheme can also be adapted to perform geometry optimizations through a damping molecular dynamics approach [45]. However, the computational efficiency in this case may not be as good as that of the BO scheme, and the CPMD is not widely used for geometry optimization.

References

[1] I. N. Levine, *Química Cuántica*, Pearson Educación (**2001**).

[2] A. Szabo and N. S. Ostlund, *Modern Quantum Chemistry: Introduction to Advanced Electronic Structure Theory*, Dover Publications (**1996**).

[3] E. Runge and E. K. U. Gross, *Phys. Rev. Lett.* 52 (12), (1984), 997.

[4] J. Kohanoff, *Electronic Structure Calculations for Solids and Molecules - Theory and computational methods*, Cambridge University Press (**2006**).

[5] P. Hohenberg and W. Kohn, *Phys. Rev.* 136, (1964), 864.

[6] R. G. Parr and W. Yang, *Density-Functional Theory of atoms and molecules*, Oxford University Press (**1989**).

[7] W. Kohn and L. J. Sham, *Phys. Rev.* 140, (1965), 1133.

[8] S. J. Vosko, L. Wilk, and M. Nusair, *Can. J. Phys.* 58, (1980), 1200.

[9] A. D. Becke, *Phys. Rev. B* 38, (1988), 3098.

[10] C. Adamo, A. di Matteo, and V. Barone, *Adv. Quantum. Chem.* 36, (1999), 45.

[11] J. P. Perdew, K. Burke, and M. Ernzerhof, *Phys. Rev. Lett.* 77, (1996), 3865.

[12] J. P. Perdew and Y. Wang, *Phys. Rev. B* 45, (1992), 13244.

[13] J. P. Perdew and et al, *Phys. Rev. B* 46, (1992), 6671.

[14] A. Becke, *J. Chem. Phys.* 98, (1993), 1372.

[15] A. Becke, *J. Chem. Phys.* 98, (1993), 5648.

[16] N. W. Ashrcoft and N. D. Mermin, *Solid State Physics*, Brooks/Cole (**1976**).

[17] W. A. Harrison, *Solid State Theory*, Dover Publications. Inc (**1980**).

[18] H. J. Monkhorst and J. D. Pack, *Phys. Rev. B* 13 (12), (1976), 5188–5192.

[19] J. C. Slater and G. F. Koster, *Phys. Rev.* 94, (1954), 1498.

[20] Philips and Kleinman, *Phys. Rev.* 116, (1959), 287–294.

[21] P. Gianozzi, *Notes on pseudopotential generation- Tutorial on "Simulating matter at the nano-scale using DFT, pseudopotentials and planewaves"*, Centre Européen de Calcul Atomique et Moléculaire (**2006**).

[22] J. A. Appelbaum and D. R. Hamman, *Phys. Rev. B* 8, (1973), 1777–1780.

[23] W. C. Topp and J. J. Hopfield, *Phys. Rev. B* 7, (1973), 1295–1303.

[24] D. R. Hammann, M. Schlüter, and C. Chiang, *Phys. Rev. Lett.* 43, (1979), 1494–1497.

[25] R. W. Shaw and J. W. A. Harrison, *Phys. Rev.* 163, (1967), 604–611.

[26] N. Troullier and J. L. Martins, *Phys. Rev. B* 43, (1991), 1993–2006.

[27] A. M. Rappe, R. M., Kaxiras, E., and J. D. Joannopoulos, *Phys. Rev. B* 41, (1990), 1227–1230.

[28] D. Vanderbilt, *Phys. Rev. B* 41, (1990), 7892–7895.

[29] H. B. Jansen and P. Ross, *Chem. Phys. Lett.* 3, (1969), 140.

[30] B. Liu and A. D. McLean, *J. Chem. Phys.* 59, (1973), 4557.

[31] R. M. Martin, *Electronic Structure Basic Theory and Practical Methods*, Cambriddge University Press (**2004**).

[32] D. Frenkel and B. Smit, *Understanding Molecular Simulation: From Algorithms to Applications*, Academic Press (**2002**).

[33] P. Giannozzi, S. Baroni, N. Bonini, M. Calandra, R. Car, C. Cavazzoni, D. Ceresoli, G. L. Chiarotti, M. Cococcioni, I. Dabo, A. D. Corso, S. de Gironcoli, S. Fabris, G. Fratesi, R. Gebauer, U. Gerstmann, C. Gougoussis, A. Kokalj, M. Lazzeri, L. Martin-Samos, N. Marzari, F. Mauri, R. Mazzarello, S. Paolini, A. Pasquarello, L. Paulatto, C. Sbraccia, S. Scandolo, G. Sclauzero, A. P. Seitsonen, A. Smogunov, P. Umari, and R. M. Wentzcovitch, *J. Phys.: Condens. Matter* 21, (2009), 395502.

[34] G. Kresse and J. Hafner, *Phys. Rev. B* 47, (1993), 558.

[35] G. Kresse and J. Furthmüller, *Phys. Rev. B* 54, (1996), 11169.

[36] G. Kresse and J. Furthmüller, *Comput. Mater. Sci.* 6, (1996), 15.

[37] R. P. Feynman, *Phys. Rev.* 56, (1939), 340–343.

[38] Hellmann, *Einführung in die Quantenchemie*, Leipxig,Deuticke (**1937**).

[39] L. Verlet, *Phys. Rev.* 159, (1967), 98–103.

[40] A. Leach, *Molecular Modelling: Principles and Applications*, Pearson Education Limited (**1999**).

[41] R. Car and M. Parrinello, *Phys. Rev. B* 55, (1985), 2471–2474.

[42] D. Marx and J. Hutter, *Modern Methods and Algorithms of Quantum Chemistry:*, J. Grotendorst, John Von Neumann Insitute for Computing (**2000**).

[43] J. P. Ryckaert, G. Ciccotti, and H. J. C. Berendsen, *J. Comput. Phys.* 23, (1977), 327–341.

[44] P. Tangney and S. Scandolo, *J. Chem. Phys.* 116, (2002), 14–24.

[45] F. Tassone, F. Mauri, and R. Car, *Phys. Rev. B* 50, (1994), 561.

Chapter 3

Dissociation free energy profiles for water and methanol on TiO_2 surfaces

In response to the huge interest in understanding surface reactivity of titania, theoretical studies based on DFT in periodic boundary conditions have been devoted to investigate the interaction and also the reaction pathways of small molecules on a variety of TiO_2 faces [1–8]. A great amount of simulations have addressed the adsorption of inorganic species as water or hydrogen peroxide, and also of organic compounds such as methanol or formic acid, as it will be referred in Chapter 6. All this work has contributed priceless information regarding the structure and the energetics of adsorption processes on TiO_2. The vast majority of these studies, however, have involved static calculations at zero temperature. Only in very few cases, finite temperature statistical sampling or special pathway-scanning techniques have been employed to obtain reaction free energies or kinetic barriers [9–11]. These thermodynamic variables are among the most relevant quantities involved in chemical processes at constant temperature and pressure, because they determine the equilibrium and the kinetic parameters ruling the reaction. Thereafter our purpose is twofold. On the one hand, we intend to establish the values of the kinetic barriers and the reaction free energies for key processes in the context of the surface chemistry of TiO_2. On the other, we seek to assess how the energies obtained at 0 K—which amount to the majority of the published data—compare to the free energies collected at room temperature. [1]

Along this research direction, we combine Car-Parrinello [13] molecular dynamics simulations with the umbrella sampling [14] methodology to investigate the dissociation free energy profiles of water and methanol on clean faces of TiO_2. Examples abound regarding the utilization of this method to investigate chemical reactions in vacuum or in biological environments, however, we are unaware of previous applications to study the reactivity of interfaces. In particular, we consider the dissociation of water on rutile (110) and anatase

[1] The results presented in this chapter have been summarized in an article appeared in the Journal of Physical Chemistry C, see reference [12].

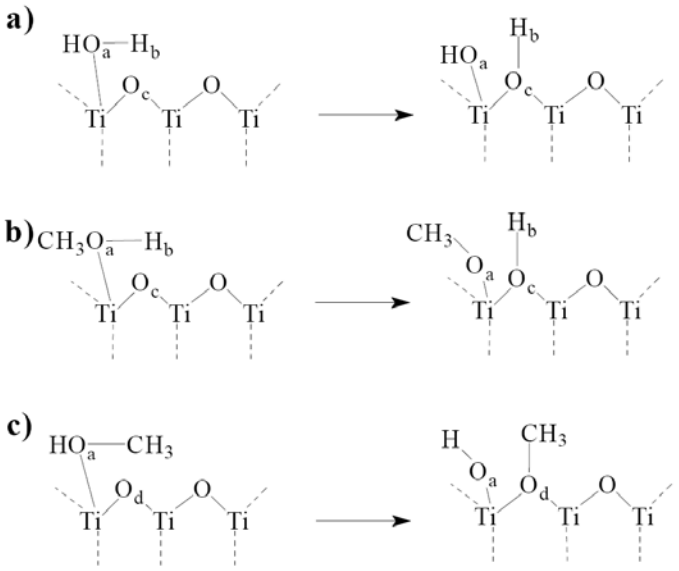

Figure 3.1. Schematics representing the dissociation of (a) the O-H bond in water, (b) the O-H bond in methanol, and (c) the C-O bond in methanol.

(101), and for this last surface we also examine the dissociation of methanol through the rupture of the O-H and the C-O bonds. These processes are schematized in Figure 3.1.

3.1 Molecular dynamics in the canonical ensemble: Nosé-Hoover thermostat

In order to introduce the umbrella sampling technique employed in this chapter, a few concepts regarding molecular dynamics simulations at constant temperature will be covered in in this section. As discussed in sections 2.3 and 2.4, the molecular dynamics technique enables to simulate the evolution of a system with time. So far, only the microcanonical framework was considered, where the number of particles, the total energy, and the volume of the system remain constant along the calculation (NVE ensemble). Molecular dynamics simulations in this chapter are carried in the canonical system, in which the fixed variables are the same as in the microcanonical system, but now the temperature is conserved instead of the energy (NVT ensemble). To this end the temperature must be controlled or thermostated [15]. In a molecular dynamics run, the temperature of the system is related to the particle velocities through the average kinetic energy ($\langle K \rangle$) according to:

$$\langle K \rangle = \frac{3}{2} N k_B T = \frac{1}{M} \sum_{j=1}^{M} \frac{1}{2} \sum_{i,j}^{N} \dot{x_i}^2 m_i \tag{3.1}$$

where N denotes the number of particles, k_B the Boltzmann constant, T the temperature, M the number of steps or configurations visited along the dynamics, and $\dot{x}_i$ and m_i the velocity and the mass of particle i, respectively.

One popular thermostating procedure is to couple the molecular system to a heat bath through the Nosé method [16]. In this approach, an extra degree of freedom corresponding to the heat bath is added to the system. A kinetic energy and a potential energy representing the heat bath are included in the Hamiltonian, allowing the energy to flow between the heat bath and the atoms. Lately, this scheme was reformulated by Hoover [17], becoming what is known as the Nosé-Hoover thermostat, which is the method we use along the simulations of the present chapter. Within the Nosé-Hoover thermostat, a velocity dependent friction term is introduced in the equations of motion:

$$m_i\ddot{x}_i = F_i - m_i\dot{x}_i\lambda \tag{3.2}$$

where $\ddot{x}_i$ and F_i denote the acceleration and the force acting on particle i, respectively. λ is the friction term which obeys its own equation of motion:

$$Q\ddot{\lambda} = 2\left[\sum_i \frac{1}{2}m_i\dot{\lambda}^2 - \frac{1}{2}gk_BT\right] \tag{3.3}$$

As a result, the kinetic energy of the nuclei fluctuates about the mean value $(1/2)gk_BT$, where g is the number of degrees of freedom associated with the nuclear coordinates, and T is the desired physical temperature of the simulation. The inertial parameter Q in equation 3.3, that can be viewed as the "mass of the bath ", controls the time scale of the thermal fluctuations. It must be noted that a simulation performed using the Nosé-Hoover thermostat also conserves energy if the thermostat potential, $gk_BT\lambda$, and kinetic energy, $(1/2)Q\lambda^2$, are considered.

3.2 Calculation of the free energy: the *Umbrella Sampling* technique

The free energy along a specific reaction coordinate is an extremely valuable piece of information, since in this profile, kinetic, energetic and mechanistic features of the reaction are enclosed. This free energy profile can be calculated through the following relation:

$$A(\xi) = -k_BT\ln g(\xi) + constant \tag{3.4}$$

where $A(\xi)$ represents the free energy and ξ the reaction coordinate. The function $g(\xi)$ is the probability distribution, which can be evaluated from a molecular dynamics run by

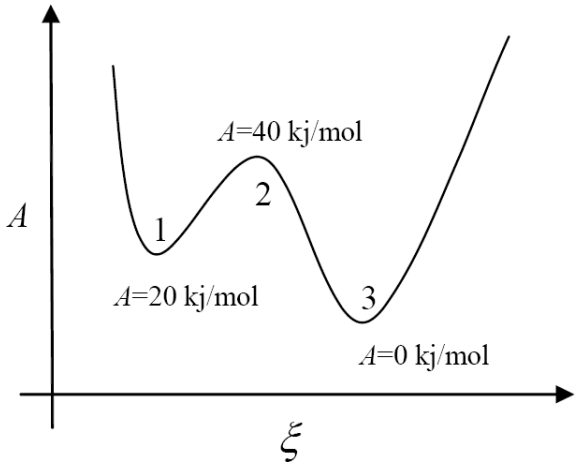

Figure 3.2. Representation of the energy as a function of the reaction coordinate

constructing a histogram registering the relative frequency in which configurations were visited along the reaction coordinate. To this end, the domain of ξ must be partitioned in small windows covering all the accessible configurations (each configuration is associated to a value of ξ). This gives an estimate to the probability density as a function of the reaction coordinate, from which the free energy profile can be calculated according to equation 3.4. However, to obtain a fair estimation of $g(\xi)$ ensuring an accurate statistical sampling, the system must visit every ξ value a considerable number of times. This will be generally the case only in shallow potential energy surfaces. Instead, unstable regions of the energy landscape, such as point (2) in Figure 3.2, will be difficult to access. When energy barriers of a few kT are present, performing long molecular dynamics may not be sufficient to recover a reliable distribution function, due to an unbalanced sampling of the different ξ points. To clarify this concept, we analyze the reaction scheme in Figure 3.2: in a molecular dynamics simulation, zones (1) and (2) would be visited 10^4 and 10^8 times less than zone (3). [2] In fact, for this energy profile the probability of reaching zone (1) is even reduced by the barrier (2), hence in a molecular dynamics simulation of a few thousand of steps, we may not have the chance to ever reach zone (1), remaining trapped in zone (3). Extending the total sampling times will not be of help, since an increase of more than 4 orders of magnitude would be needed, unfeasible in any practical case. Consequently, equation 3.4 is not the most common path to evaluate the free energy profile along a reaction coordinate.

In order to precisely determine the free energy values along the whole reaction coordinate, the potential energy surface can be modified according to:

[2] Probabilities calculated considering the Boltzmann factor $e^{-\Delta E/kT}$.

$$V'(\xi) = V(\xi) + V_W(\xi) \tag{3.5}$$

where $V(\xi)$ and $V_W(\xi)$ represent the potential energy of the system and an additional potential, respectively. By selecting the correct $V_W(\xi)$, it is possible to bias the apparent energy landscape and get access to a suitable amount of data for every point along the reaction coordinate, specially for those that were more rarely visited (shown as number (2) and (3) in figure 3.2). From statistical thermodynamics [18] it can be deduced that every average system property $\langle Q \rangle$ of the original system can be calculated conforming to:

$$\langle Q \rangle = \frac{\langle Q \rangle_W}{\langle W(\xi) \rangle_W} \tag{3.6}$$

where the subscript W denotes the modified system and $W(\xi)$ is defined as:

$$W(\xi) = e^{-V_W(\xi)/kT} \tag{3.7}$$

The functional form of $V_W(\xi)$ is:

$$V_W(\xi) = \frac{1}{2} k_u (\xi - \xi_0)^2 \tag{3.8}$$

Combining equations 3.8 and 3.5 the total energy of the system within the DFT framework can be written:

$$E_{tot} = E_{KS} + \frac{1}{2} k_u (\xi - \xi_0)^2 \tag{3.9}$$

where E_{tot} represents the total energy of the system and E_{KS} the Kohn-Sham energy. Considering equations 3.6, 3.7 and 3.8, the probability distribution as a function of ξ can be recovered from the biased sampling:

$$P(\xi) = \frac{P_W(\xi)}{e^{-1/2k_u(\xi-\xi_0)^2}} \tag{3.10}$$

where $P_W(\xi)$ is the distribution function evaluated in the modified potential. Inserting this result in equation 3.4, the free energy of the system can be calculated as:

$$A(\xi) = -k_B T ln(P_W(\xi)) - \frac{1}{2} k_u (\xi - \xi_0)^2 + constant \tag{3.11}$$

Within this approach the free energy profile in the original potential is calculated from a biased sampling. This method is known as the *Umbrella Sampling* technique [14].

The implementation of this scheme involves adjusting two parameters, ξ and k_u, which would make possible to sample the whole reaction coordinate in a proper way. Generally it is not possible to sample the whole reaction coordinate with only one pair of values for

ξ and k_u, therefore the problem is divided in different reaction coordinate windows that are sampled separately using a pair of parameters for each one. Then these pieces are assembled all together, so that the value of $A(\xi)$ at the border of every window matches the value of $A(\xi)$ at the contiguous window. This is equivalent to choose the values of the constants appearing as the last term in eq 3.11 so that $A(\xi)$ be continuous along the full profile.

It is important to notice that, to apply the methodology, a reaction coordinate has to be proposed in advance. In this thesis the *Umbrella Sampling* technique was coupled to *Car-Parrinello* [13] molecular dynamics in the *Quantum Espresso* [19] package and different reaction coordinates were studied as exposed in section 3.5.

3.3 Specif knowledge of the system

According to DFT calculations by Harris and Quong, water adsorbs molecularly on rutile (110) below monolayer coverage [5]. The barrier to dissociation was assumed to be very small, as suggested by TPD (Temperature Programmed Desorption) experiments showing that a fraction of the molecules belonging to the first layer dissociated at 160 K [20]. In fact, spontaneous dissociation had been previously reported in molecular dynamics trajectories at 500 K [21]. In later works, the internal energy barrier was computed on the same surface trough different approaches. Lindan and Zhang applied a constrained optimization scheme to find an energy barrier of 8.3 kcal/mol at a coverage of half a monolayer [10]. Oviedo et al., on the other hand, estimated a value of 6.9 kcal/mol using the Nudged Elastic Band (NEB) method [11].[3] For methanol on rutile (110), static DFT calculations rendered dissociative adsorption more favorable than molecular adsorption by just 4 kcal/mol [24]. On anatase (101), electronic structure studies indicate that molecular adsorption predominates for both water and methanol [3, 6, 7, 25]. Barrier to dissociation was studied for the case of water on an oxygen vacancy: a free energy barrier of 2.8 kcal/mol was obtained through the blue moon ensemble method [9].

3.4 Computational Settings

All calculations were performed using density functional theory in periodic boundary conditions as implemented in the Quantum-Espresso package [19]. The Kohn-Sham orbitals and charge density were expanded in plane-waves basis sets up to a kinetic energy cutoff of 25 Ry and 200 Ry, respectively. The Perdew-Wang (PW91) approach to the exchange-

[3]The NEB method performs a search of the reaction pathway between given initial and final states and provides an estimate of the internal energy profile [22, 23].

correlation energy [26, 27] and Vanderbilt ultrasoft pseudopotentials [28] were adopted to compute the total energies and forces. Geometry optimizations were performed at the Born-Oppenheimer approximation, while molecular dynamics simulations were carried out within the Car-Parrinello method [13] using a Nóse Hoover [17] thermostat at 300 K and a time step of 0.17 fs. Reciprocal space sampling was restricted to the Γ-point.

The anatase (101) surface was represented by a (2×2) slab four layers deep, whereas in the case of rutile (110), a (2×1) surface made of four layers of atoms was adopted. The supercell dimensions were 7.55 × 10.20 × 22.00 ^{3} for anatase and 6.01 × 6.48 × 24.00 ^{3} for rutile, both of them containing a total of 48 atoms excluding the adsorbates.

Application of the umbrella sampling approach requires a specific reaction path to be decided in advance (see section 3.2). A series of molecular dynamics runs were performed for different values of ξ_0 along the selected reaction coordinate, covering the full pathway between reactants and products, in steps of 0.1 - 0.2 . The force constant k_u was tuned for appropriate sampling. A histogram was produced for each value of ξ_0, reflecting the (logarithmic) probability distribution of ξ along the whole trajectory. For each ξ_0, simulation times varying from 1 to 4 ps were necessary to get converged distributions, depending on k_u and the width of the spanned ξ-space. Every histogram was then weighted by the exponential factor $e^{-\frac{1}{2}k_u(\xi-\xi_0)^2}$ as exposed in equation 3.10, to extract a piece of curve representing the free energy around ξ_0. Finally, the free energy profile was constructed by matching these pieces corresponding to adjacent values of ξ_0 [14, 29].

3.5 Results and Discussion

3.5.1 Water dissociation on rutile (110) and anatase (101)

On rutile (110), energy minimizations yield the molecular state of water as the most stable. In agreement with previous results [5], we find it is only 3.4 kcal/mol below the dissociated state, in which a proton is transferred to a bridge oxygen atom on the surface (see Figure 3.1a). This difference is close to the chemical accuracy of density functional theory, and it has been shown that is quite sensitive to surface coverage and slab thickness [5]. For those reasons, the adsorption mode of water on rutile (110) has been a matter of controversy in the literature until recently [5, 30]. To investigate the free energy associated with the break of the O-H bond, we proposed the following reaction coordinate:

$$\xi = |\mathbf{r}(O_a) - \mathbf{r}(H_b)| - |\mathbf{r}(O_a) - \mathbf{r}(O_c)| \tag{3.12}$$

where $\mathbf{r}(O_a)$, $\mathbf{r}(O_c)$ and $\mathbf{r}(H_b)$ refer, respectively, to the spatial coordinates of the water oxygen atom, the bridge oxygen atom of the surface, and the transferred proton (Fig-

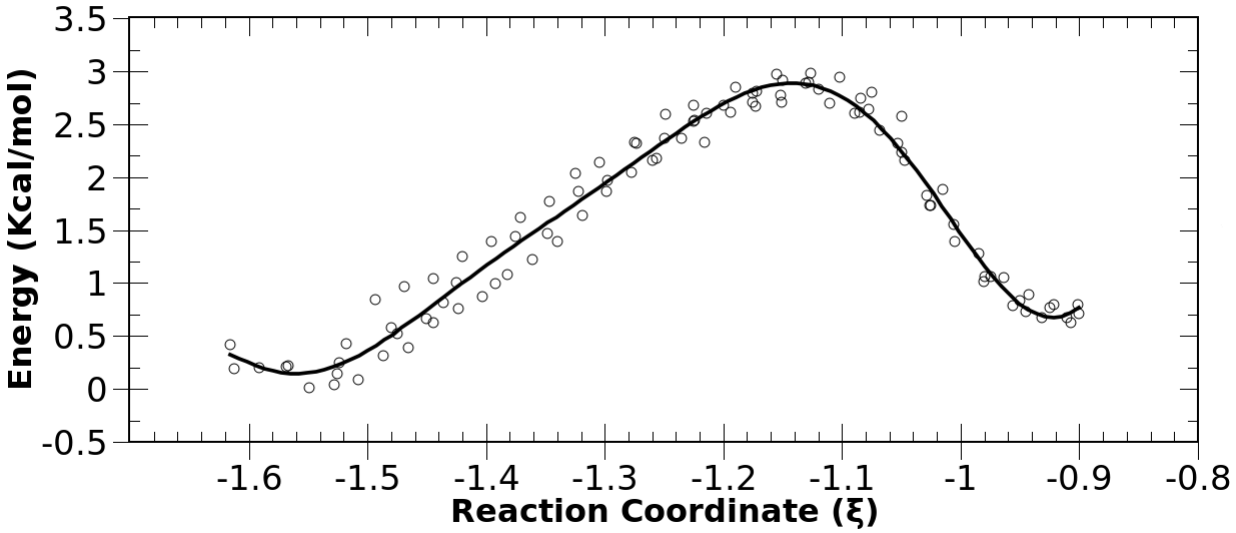

Figure 3.3. Free energy profile for the dissociation of H_2O on rutile (110).

ure 3.1a). The first term on the right hand side of equation 3.12 induces the rupture of the O_a-H_b bond consistently with the increase of the reaction coordinate, whereas the second term directs the hydroxyl group toward the bridge atom O_c. With this choice, which of course is not unique, ξ varies from around -1.6 to -0.9 as the reaction evolves from the molecular (reactant) to the dissociative (product) state. This kind of reaction coordinate has been already employed in the study of simple reaction pathways through restrained minimization techniques [31] or umbrella sampling simulations [32, 33]. Figure 3.3 displays the free energy as a function of ξ. The dissociation free energy is only 0.4 kcal/mol, which gives an equilibrium constant of nearly 0.5. In turn, the activation free energy to dissociate the proton turns out to be 2.7 kcal/mol or ca. 4 kT, significantly lower than the barriers estimated previously on the basis of zero temperature calculations [10, 11]. Our results suggest that molecular and dissociated water would coexist on the undefective (110) surface, exhibiting a fast dissociation-recombination behavior at room temperature. Such conclusions are consistent with TPD spectra [20] and with spontaneous dissociation observed during molecular dynamics at 500 K [21]. A positive entropic contribution can be estimated from the difference between the reaction energy at zero temperature (assuming it to be a reasonable approximation to the reaction enthalpy and disregarding its temperature dependence) and the free energy at 300 K. This data is collected in Table 3.1.

In the case of water on anatase (101), two H-bonds arise between the adsorbed molecule and the two closest bridge oxygen atoms of the surface. The internal energy turns out to be 12.2 kcal/mol lower for molecular adsorption than for the dissociative path. A similar

Table 3.1. Reaction internal energies (ΔE), reaction free energies (ΔG), activation free energies ($\Delta G^{\ddagger}$) and entropies (ΔS) involved in the dissociation of water and methanol.

	ΔE kcal/mol	ΔG kcal/mol	$\Delta G^{\ddagger}$ kcal/mol	ΔS J K^{-1} mol^{-1}
rutile (110)				
$H_2O \rightarrow OH + H$	3.4	0.4	2.7	42
anatase (101)				
$H_2O \rightarrow OH + H$	12.2	6.7	10.5	77
$CH_3OH \rightarrow CH_3O + H$	7.3	8.5	13.6	-17
$CH_3OH \rightarrow CH_3 + OH$	6.2	7.2	60.3	-14

structure and energy difference were found by Vittadini et al. [3]. In Figure 3.4, the reaction coordinate corresponding to reactants is slightly more negative than in rutile, because the distance from H_2O to the bridge atom in anatase is longer. Umbrella sampling analysis yields a reaction free energy of 6.7 kcal/mol (Figure 3.4 and Table 13.1). This leads to a dissociation entropy of 77 J K^{-1} mol^{-1}, more positive than for rutile (110), even though in both surfaces the reactions involve breaking and forming of the same bonds. The activation energy to go from the dissociated to the molecular state is also larger than on rutile (3.8 kcal/mol versus 2.3 kcal/mol), reflecting the longer distances between the surface sites in the (101) face.

Inspection of the trajectories at 300 K reveals that most of the time the water molecule maintains simultaneously the two hydrogen bonds evinced in the geometry optimization. This behavior is illustrated in Figure 3.5, where the distances between the H_2O protons and the oxygen sites on the TiO_2 surface are monitored during 5 ps of dynamics. In the lower panel the identity of the oxygen atoms is inverted with respect to the upper panel. At the beginning of the simulation, water hydrogen atoms labeled H1 and H2 are bonded to atoms O1 and O2 of the interface, respectively. These bonds tend to subsist with some interruptions during the first 1.5 ps of dynamics; then the molecule flips and the interactions are exchanged, to produce bonds H1-O2 and H2-O1. Finally, at around 4.5 ps the original connectivity is restored.

3.5.2 Methanol dissociation on anatase (101)

The same reaction coordinate as introduced in equation 3.12 was used to examine dissociation of the O-H bond in methanol on the anatase surface. In this case, $\mathbf{r}(O_a)$ represents the position of the methanol oxygen atom. Table 3.1 shows that the internal reaction energy is slightly lower than for the dissociation of water on the same surface. This result

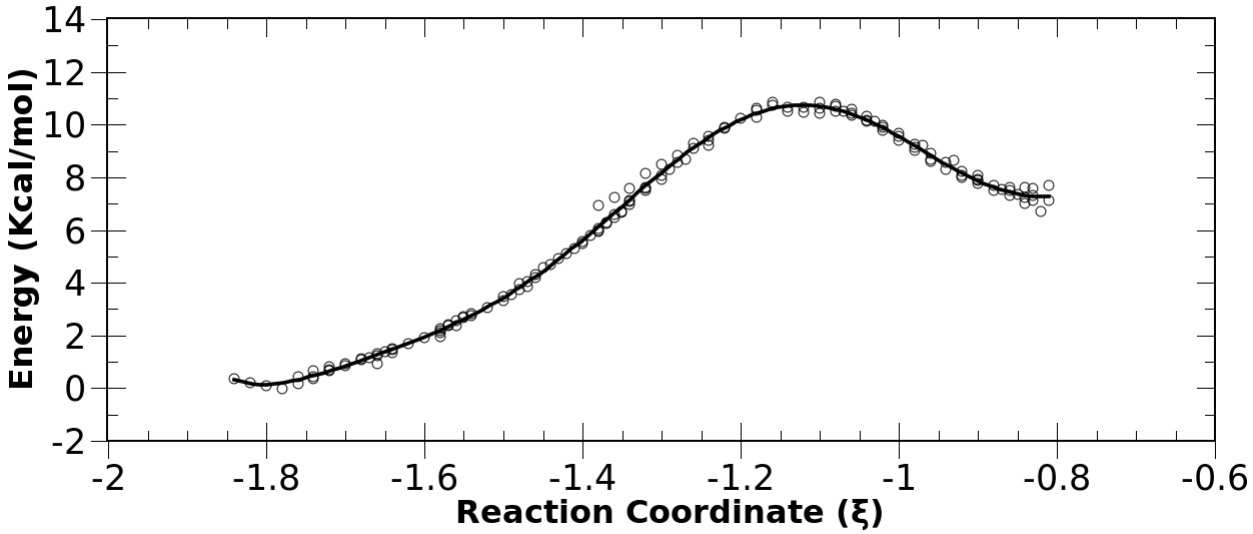

Figure 3.4. Free energy profile for the dissociation of H_2O on anatase (101).

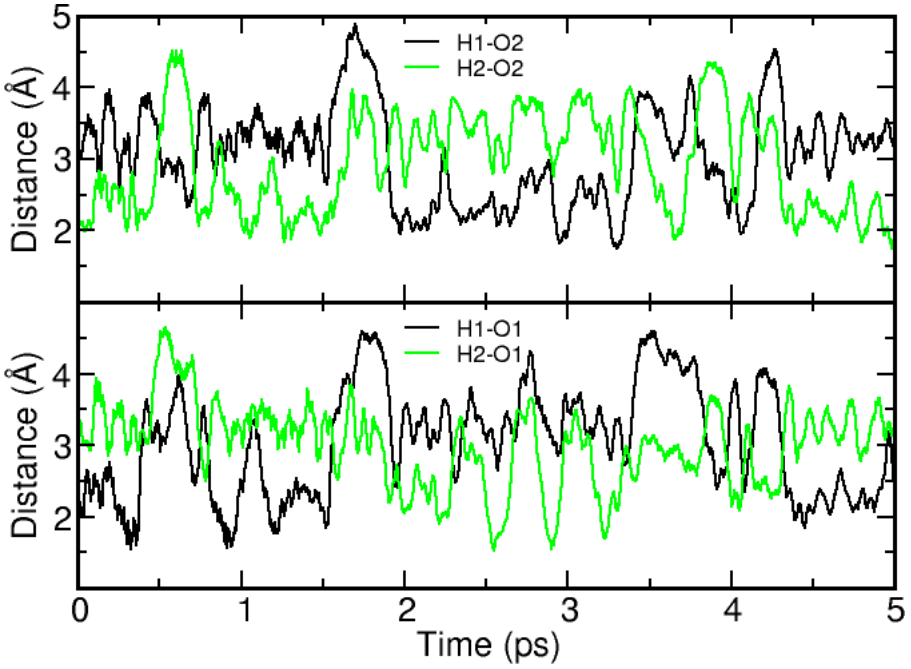

Figure 3.5. Time evolution of the distances from the hydrogen atoms H1 and H2 of the H_2O molecule to the oxygen atoms O1 and O2 on the surface, according to Car-Parrinello molecular dynamics of water on anatase (101). H-bonding interactions H1-O1 and H2-O2 alternate every few picoseconds with H1-O2 and H2-O1.

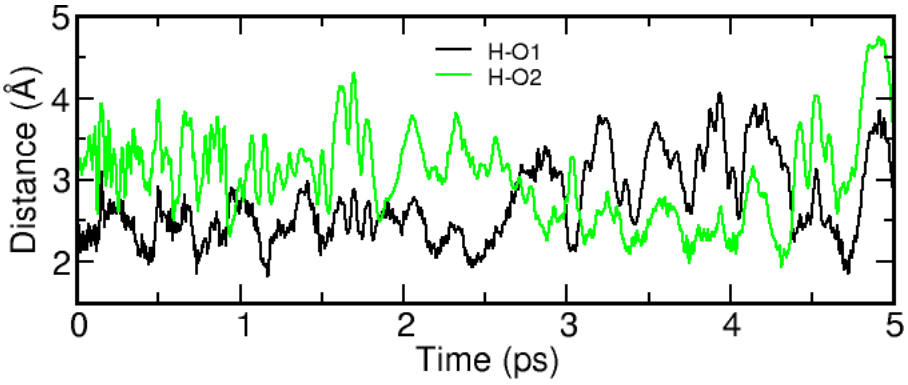

Figure 3.6. Time evolution of the distances from the hydrogen atoms of the methanol molecule to the oxygen atoms O1 and O2 on the surface, according to Car-Parrinello molecular dynamics of water on anatase (101). Hydrogen bonds form alternatively with O1 and O2.

is consistent with the larger proton acidity in methanol as compared to water, and is in agreement with previous calculations [25].

The molecular dynamics simulations show that the OH group forms short-living H-bonds rapidly alternating between two equidistant oxygen atoms of the surface. Figure 3.6 depicts the evolution of the interatomic distances between the proton and such oxygen atoms at 300 K. It can be seen that the molecule spends most of the simulation time H-bonded to either oxygen site: as soon as the distance to one of the O atoms increases, the other decreases.

From the thermodynamical analysis, ΔG turns out to be larger than ΔE (Figure 3.7 and Table 3.1), and so, conversely to the case of water, we find a negative dissociation entropy for this reaction. We note that in spite of being a dissociative process, the number of chemical bonds remains constant when evolving from reactants to products, and therefore the sign of ΔS is not an obvious question. Even so, the difference in the sign of ΔS for the dissociation of water in comparison to methanol is certainly intriguing, since in both cases a O-H bond is broken and a proton is transferred to a bridge oxygen site of the surface. As will be shown below, the entropy change for the rupture of methanol across the C-O bond is also negative. These results suggest that the methanol adsorbed on the surface, at variance with H_2O, exhibits an excess molecular entropy (in comparison with the dissociated species), which is lost regardless of the dissociation mechanism. The source of this entropy might be attributed to the rotation of the methyl group: this mode is lost upon dissociation, since the radicals CH_3-O or CH_3 are more strongly bound to the surface. We recall, as discussed above, that for both water and methanol there are two accessible, degenerate H-bonded stable configurations, which are visited at intervals of 1 - 2 ps. This itineracy of the hydroxyl moiety might involve an entropic contribution which is lost with the molecular rupture, but should be equally present in both adsorbates.

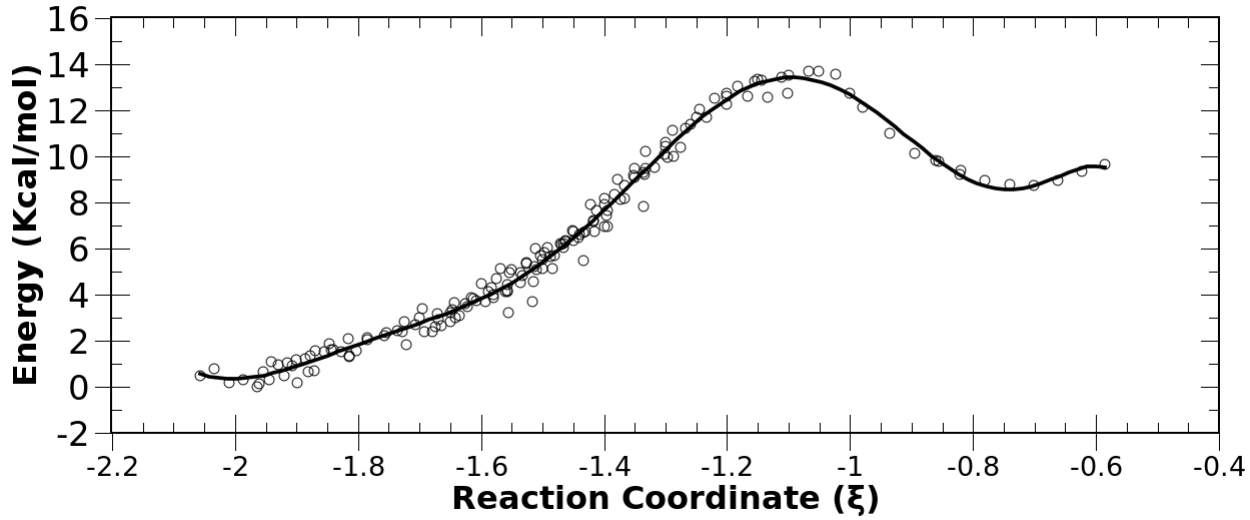

Figure 3.7. Free energy profile for the dissociation of methanol across the O-H bond on rutile (110).

Alternatively, we have considered the dissociation of methanol through breaking the C-O bond. To this end, a reaction coordinate depending on the positions of four nuclei was chosen:

$$\xi = |\mathbf{r}(O_a) - \mathbf{r}(C)| - |\mathbf{r}(O_d) - \mathbf{r}(C)| - |\mathbf{r}(O_a) - \mathbf{r}(Ti)| \tag{3.13}$$

where $\mathbf{r}(O_a)$, $\mathbf{r}(C)$, $\mathbf{r}(O_d)$ and $\mathbf{r}(Ti)$ refer, respectively, to the spatial coordinates of the methanol oxygen atom, the methanol carbon atom, the bridge oxygen atom of the surface, and the five-coordinate titanium atom to which the hydroxyl is bound (Figure 3.1). Given the large activation barrier to break the C-O_a bond (see below), the use of a reaction coordinate analogous to that in equation 3.12 implemented for the dissociation of the O-H bond, led in the present case to the rupture of the Ti-O_a link, which offers a lower dissociation barrier. For this reason, it was necessary to include the Ti-O_a distance in the choice of ξ, to force the C-O_a breaking while preserving the Ti-O_a bond. This reaction coordinate assumes that C-O_a dissociation proceeds concertedly with the formation of the C-O_d bond. Under this definition, ξ is approximately -4.0 for reactants and -0.5 for products.

Table 3.1 indicates that the internal and free energy differences for this reaction are comparable to (or slightly smaller than) those found when the O-H bond is broken. However, the barrier to dissociation is huge, of nearly 60 kcal/mol (Figure 3.8), due to the strength of the C-O bond that needs to be disrupted. The formation of a new C-O link with the surface energetically compensates, to some extent, the original one; but the activation

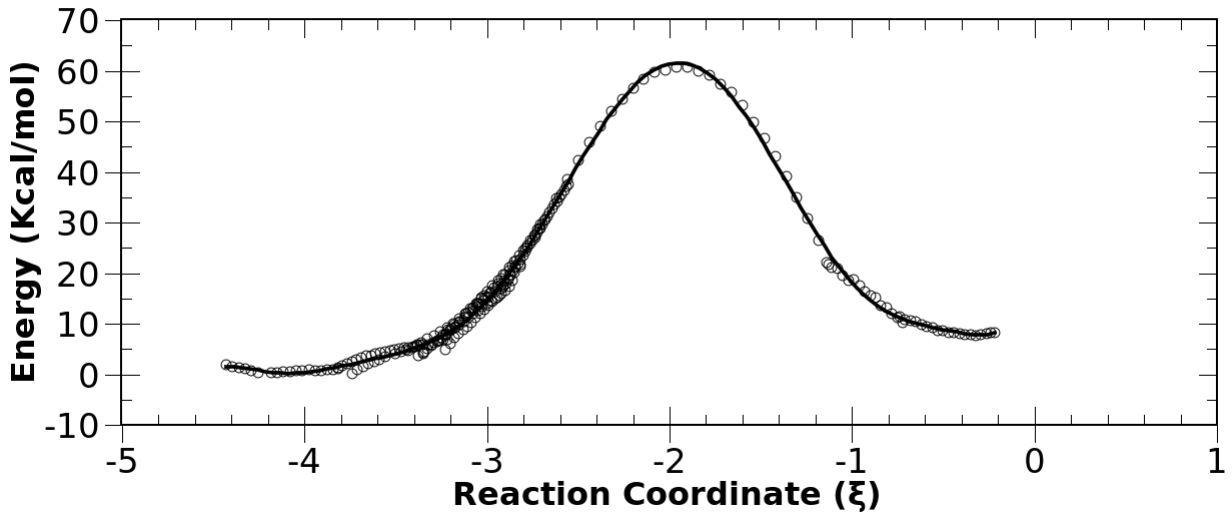

Figure 3.8. Free energy profile for the dissociation of methanol across the C-O bond on anatase (101).

barrier could never be surmounted in the absence of a catalytic agent.

As a final remark, it is worth noting that the (negative) entropic term for this reaction is surprisingly close to that corresponding to the dissociation across the O-H bond (-14 J K^{-1} mol^{-1} versus -17 J K^{-1} mol^{-1}). This reinforces the notion that most of the entropy change in both reactions comes from the disappearance of the methanol molecule.

3.6 Conclusions

In this chapter we have reported and discussed activation and free energies for the dissociation of water and methanol on perfect titania surfaces. In spite of the relevance of these processes in the context of surface reactivity of TiO_2, to the best of our knowledge, estimates of the free energies involved had not been published before. Our results show, consistently with previous simulations at zero temperature, that on anatase (101) molecular adsorption of water and methanol are strongly favored. Spontaneous dissociation of these molecules on anatase would only be feasible in the presence of defects, as demonstrated by other authors [9]. In the case of rutile (110), the stability of the dissociated and the molecular forms of water becomes comparable. Thus, both are likely to coexist on the surface, displaying a fast, reversible interconversion.

It can be observed that for most of the cases examined in this study, the entropic term contributed less than 3 kcal/mol—in absolute value—to the reaction free energies at 300

K. Only for major value of ΔE a larger entropic term was found. This result constitutes, to some extent, and at least for simple dissociative processes with lower ΔE values, a validation of the widespread use of energies at 0 K to assess the adsorption mode at room temperature. The entropic effect, however, might play a role to the point of altering the relative trends predicted by the computations at zero temperature. This is the case of CH_3OH and H_2O on anatase (101): the ΔE values suggest methanol should dissociate more easily than water, which turns out to be false when the entropy is considered.

The umbrella sampling technique proved to be an efficient, valuable tool to compute activation barriers and reaction free energies for dissociative processes at interfaces. Whereas this technique exhibits the disadvantage that tentative pathways must be provided beforehand, this requirement has little impact on elementary reactions as those proposed here, where simplicity rules out the chance of alternative routes. Yet, we do not imply the application of the umbrella sampling method is restricted to these kind of basic processes. With the exploration of a proper set of reaction coordinates judiciously selected, we envision it could become an extremely useful instrument to look into many kinds of surface chemistry problems, from catalytic transformations to vacancy diffusion.

3.7 Appendix

This section compiles, for each reaction studied, the histograms representing the probability distributions according to the umbrella sampling molecular dynamics simulations, for all combinations of ξ_0 and k_u employed. On the side of each graph, the values of ξ_0 are given in Å and the values of k_u in kcal/mol $\times$ Å^2. Note that the repetition of pairs (ξ_0; k_u) in the same system corresponds to two trajectories started from different initial configurations.

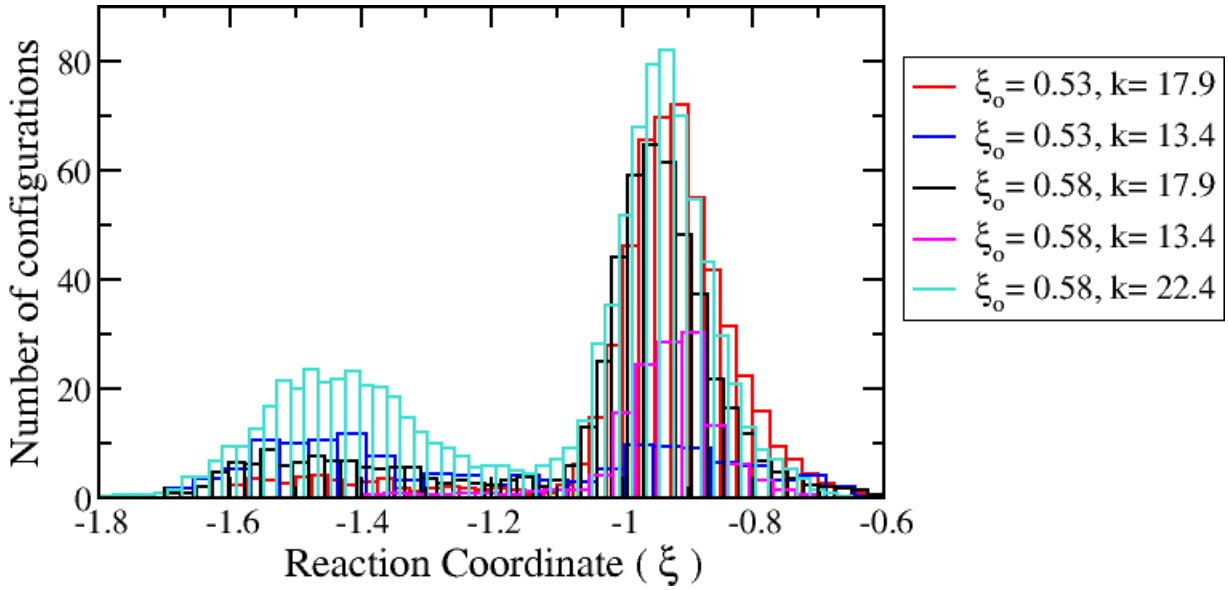

Figure 3.9. Probability distributions obtained via the umbrella sampling method for the dissociation of water on rutile (110).

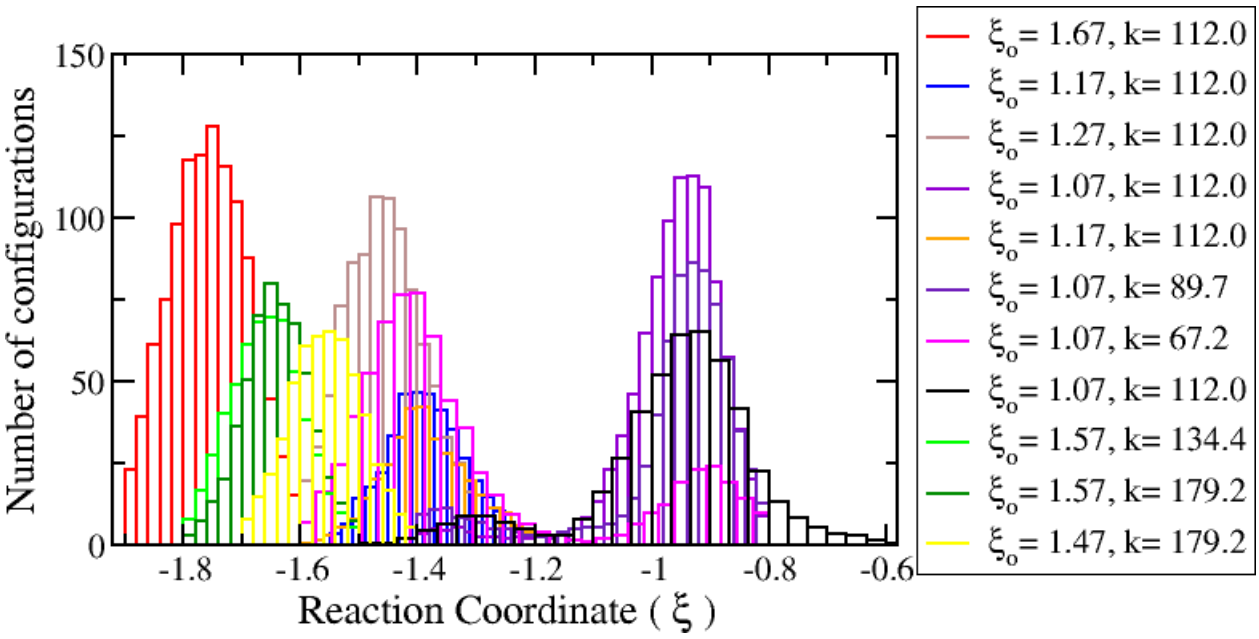

Figure 3.10. Probability distributions obtained via the umbrella sampling method for the dissociation of water on anatase (110).

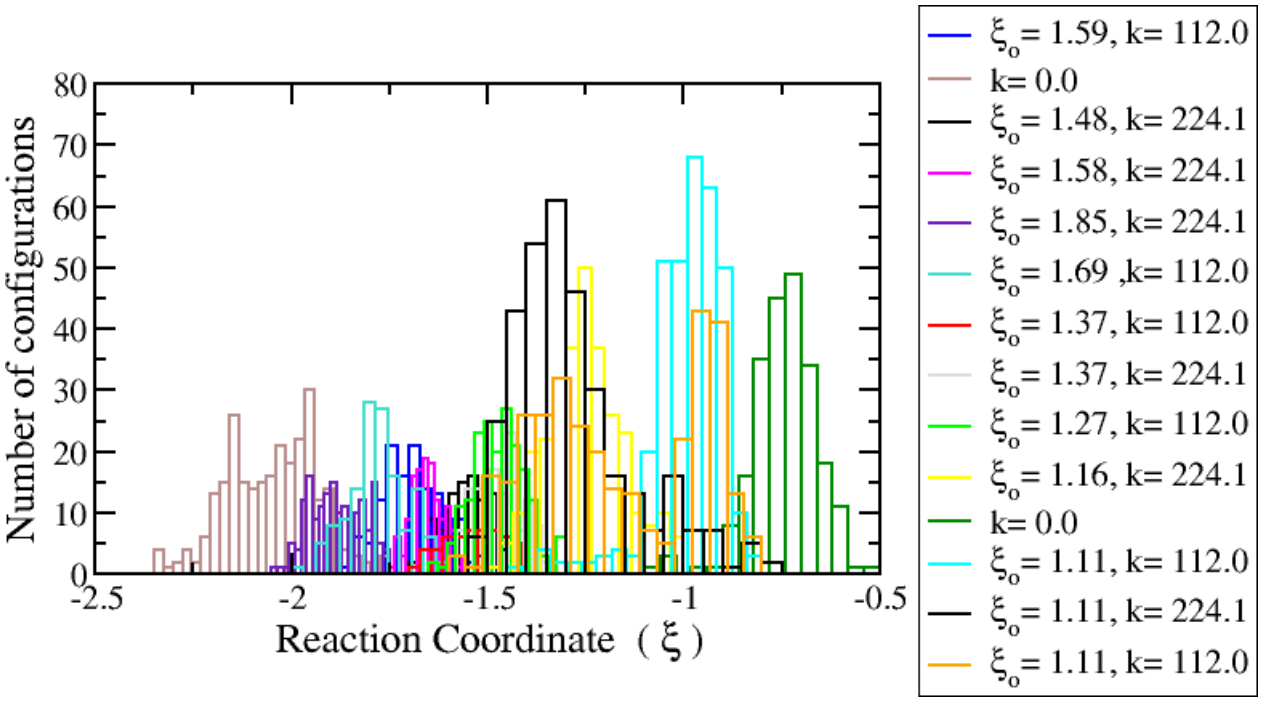

Figure 3.11. Probability distributions obtained via the umbrella sampling method for the dissociation of methanol across the O-H bond on anatase (101).

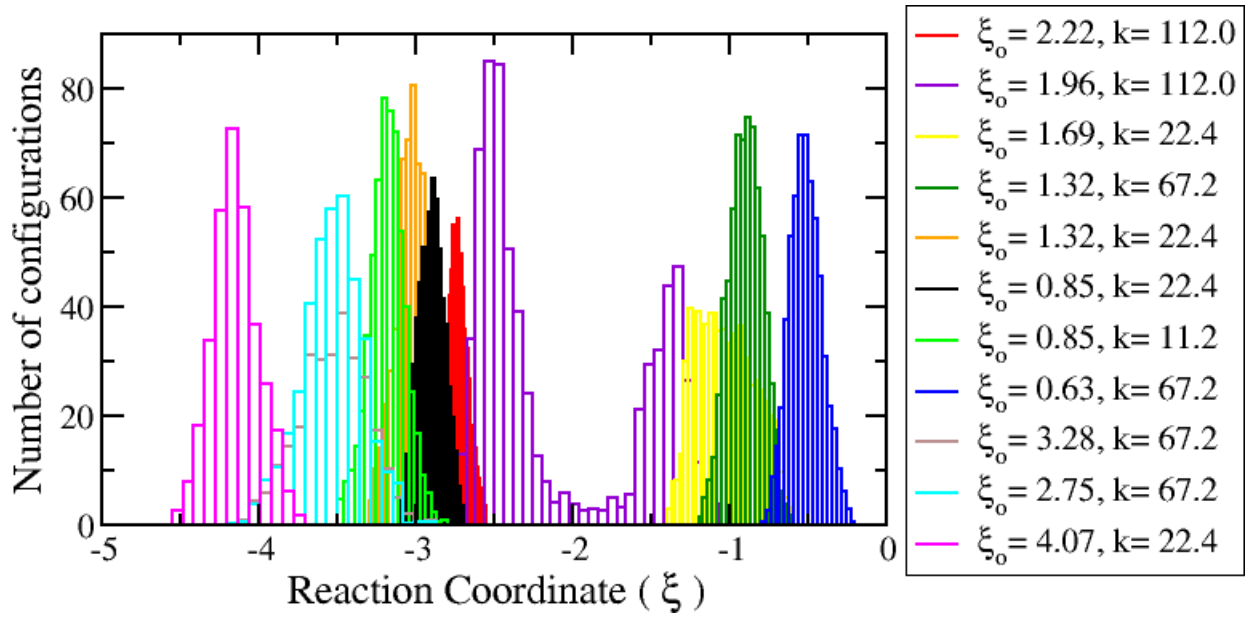

Figure 3.12. Probability distributions obtained via the umbrella sampling method for the dissociation of methanol across the C-O bond on anatase (101).

References

[1] S. Bates, G. Kresse, and M. J. Gillan, *Surf. Sci.* 409, (1998), 336.

[2] A. Selloni, A. Vittadini, and M. Gratzel, *Surf. Sci.* 219, (1998), 402–404.

[3] A. Vittadini, A. Selloni, F. Rotzinger, and M. Grätzel, *Phys. Rev. Lett.* 81, (1998), 2954.

[4] U. Diebold, *Surf. Sci. Rep.* 48, (2003), 53–229.

[5] L. A. Harris and A. A. Quong, *Phys. Rev. Lett.* 93, (2004), 086105.

[6] A. Tilocca and A. Selloni, *J. Phys. Chem. B* 108, (2004), 4743.

[7] A. Tilocca and A. Selloni, *Langmuir* 20, (2004), 8379.

[8] C. L. Pang, R. Lindsay, and G. Thornton, *Chem. Soc. Rev.* 37, (2008), 2328–2353.

[9] A. Tilocca and A. Selloni, *J. Chem. Phys.* 119, (2003), 7445.

[10] P. J. D. Lindan and C. Zhang, *Phys. Rev. B* 72, (2005), 075439.

[11] J. Oviedo, R. S. de Armas, M. A. S. Miguel, and J. F. Sanz, *Phys. Chem. C Lett.* 112, (2008), 17737–17740.

[12] V. M. Sánchez, J. A. Cojuloun, and D. A. Scherlis, *J. Phys. Chem. C* 114, (2010), 11522–11526.

[13] R. Car and M. Parrinello, *Phys. Rev. B* 55, (1985), 2471–2474.

[14] J. P. Torrie, G.and Valleau, *J. Comput. Phys.* 23, (1977), 187.

[15] T. K. Woo, P. Margl, P. E. Blöch, and T. Ziegler, *J. Phys. Chem. A* 106, (2002), 1173–1182.

[16] S. Nosé, *Mol. Phys.* 52, (1984), 255.

[17] W. G. Hoover, *Phys. Rev. A* 31, (1985), 1695.

[18] D. Chandler, *Introduction to statistical mechanics*, Oxford University press (**1986**).

[19] P. Giannozzi, S. Baroni, N. Bonini, M. Calandra, R. Car, C. Cavazzoni, D. Ceresoli, G. L. Chiarotti, M. Cococcioni, I. Dabo, A. D. Corso, S. de Gironcoli, S. Fabris, G. Fratesi, R. Gebauer, U. Gerstmann, C. Gougoussis, A. Kokalj, M. Lazzeri, L. Martin-Samos, N. Marzari, F. Mauri, R. Mazzarello, S. Paolini, A. Pasquarello, L. Paulatto, C. Sbraccia, S. Scandolo, G. Sclauzero, A. P. Seitsonen, A. Smogunov, P. Umari, and R. M. Wentzcovitch, *J. Phys.: Condens. Matter* 21, (2009), 395502.

[20] R. L. Kurtz, R. Stockbauer, T. E. Madey, E. Román, and J. L. de Segovia, *Surf. Sci.* 218, (1989), 178.

[21] P. J. D. Lindan, N. M. Harrison, J. M. Holender, and M. J. Gillan, *Chem. Phys. Lett.* 261, (1996), 246.

[22] G. Mills, H. Jnsson, and G. K. Schenter, *Surf. Sci.* 324, (1995), 305.

[23] G. Henkelman, B. P. Uberuaga, and H. Jnsson, *J. Chem. Phys.* 113, (2000), 9901.

[24] S. Bates and M. J. Gillan, *J. Phys. Chem. B* 102, (1998), 2017.

[25] A. Tilocca and A. Selloni, *J. Phys. Chem. B* 108, (2004), 19314.

[26] J. P. Perdew and Y. Wang, *Phys. Rev. B* 45, (1992), 13244.

[27] J. P. Perdew and et al, *Phys. Rev. B* 46, (1992), 6671.

[28] D. Vanderbilt, *Phys. Rev. B* 41, (1990), 7892–7895.

[29] D. Frenkel and B. Smit, *Understanding Molecular Simulation: From Algorithms to Applications*, Academic Press (**2002**).

[30] R. Schaub, P. Thostrup, N. Lopez, E. Lægsgaard, I. Stensgaard, J. K. Nørskov, and F. Besenbacher, *Phys. Rev. Lett.* 87, (2001), 266104.

[31] V. M. Sánchez, A. Crespo, J. S. Gutkind, and A. G. Turjanski, *J. Phys. Chem. B* 110, (2006), 18052.

[32] D. E. Bikiel, F. Di Salvo, M. C. González Lebrero, F. Doctorovich, and D. A. Estrin, *Inorg. Chem.* 44, (2005), 5286.

[33] M. C. González Lebrero and D. A. Estrin, *J. Chem. Theory Comput.* 3, (2007), 1405.

Chapter 4

Proton transfer in aminopropyl functionalized SiO_2 and TiO_2 surfaces

4.1 Introduction

The capability to synthesize reproducible mesoporous materials of controlled size and structure constitutes one of the most innovative developments among the recent achievements in the field of material chemistry [1–4]. The diameter of the pores, their connectivity, and the possibility of attaching biological or organic functions, are all tunable features along the synthetic route. Mesoporous matrices exhibit unprecedented surfaces areas (100 – 1000 m^2 $g^{-}1$) and can be based on a variety of inorganic compounds, such as silica and titania. Hybrid mesoporous materials made of inorganic oxides functionalized with organic molecules [2, 5] constitute very interesting assemblies, which chemistry is determined by the nature of the organic functions decorating the mesopore. The field of hybrid mesoporous materials is nowadays expanding very fast. Mesoporous hybrid thin films (MHTFs) present a great interest for their potential in domains such as optics, electronics, chemical sensing, catalysis, separation, and so forth [6–8]. The introduction of organic or metallo-organic functions on the surface of pores is a step forward toward the creation of complex chemical systems with tuned reactivity [9–11], including the possibility of accommodating molecular functions with a well-defined location in space [12, 13]. Several organic functions have been introduced in both silica and nonsilica matrices [5, 14]. In particular, amino groups (-NH_2) are interesting because of the possibility of creating pH-responsive charged surfaces with perm-selective properties, biomolecule binding, or creation of enzyme-like surface sites for advanced catalysis [15–17].

In particular in this chapter we focused on the speciation of amino-propyl groups as a function of pH in silica and titania matrices, i.e., the ratio between the -NH_2 and -NH_3^+ (ammonium) species. Experimental work on the acidic behavior of amino functionalized groups [18,19], and in particular experimental data obtained in the groups of G. Soler Illia and F. Williams, suggested the possibility of modulating the -NH_2 group acidity through the

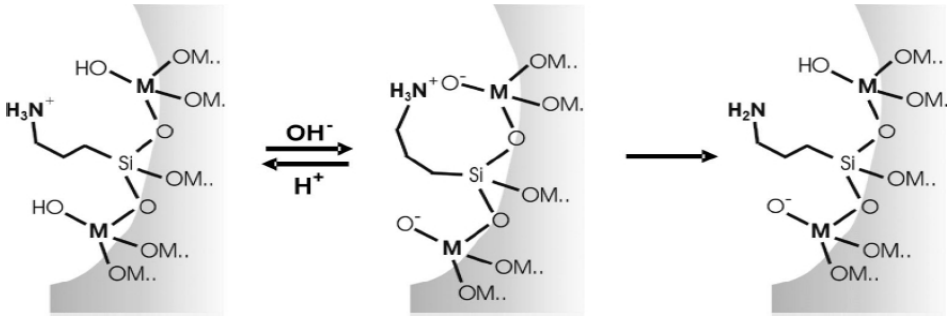

Figure 4.1. Proposed model for the speciation and interactions of the surface groups as a response to pH, according to experiments and simulations.

negative oxygen atoms, present at the surface for pHs above the isoelectric point[1] of the oxide [21]. This idea is depicted in Figure 4.1. The intermediate step was proposed considering data reported in the literature, where titration measurements on aminopolysiloxane gels and powders in equilibrium with an aqueous solution have established that ammonium is the major species, either forming an ion pair with counterions at low pH, or interacting with Si-O^- sites at hig pH values [22].

Ab initio calculations of the silica and titania surfaces with amino-propyl functions were performed, in order to complement X-ray photoelectron spectroscopy (XPS) and other experimental data obtained in the group of G. Soler Illia, aiming to determine whether the ammonium-amino ratio is controlled by the acidic surface groups. To this end, the silica and titania surfaces were modelled through the β-cristobalite (111) and anatase (101) faces, respectively[2].

The experimental syntethic route to obtain the aminopropyl functionalized MHTFs utilizes tetraethoxysilane (TEOS) and $TiCl_4$ as inorganic precursors and APTES ($(CH_3CH_2O)_3Si(CH_2)_3NH_2$) to introduce the amino function [21]. Therefore, to simulate these systems we introduce the APTES in replacement of one silanol group (-Si-OH) in the case of silica, and of one Ti(5c) surface atom in the case of titania. Consistently with the synthetic route, the titania surface was modelled as an hydroxilated surface. The model structures are depicted in Figure 4.2.

Our simulations were performed in vacuum and in the presence of two water monolayers, to examine the amino-ammonium equilibrium at the surface under different environments. Molecular dynamics simulations at room temperature were carried out to assess the possibility of proton transfer from the ammonium to the surface. Eventually, counterions were explicitly included in the simulation, to evaluate their effect on the ionization of the

[1]The isoelectric point, or pH_{iep}, is the pH value at which the surface charge is zero because equals amounts of positive and negative charges are present [20].

[2]Details about these surface structures were given in Chapter 1

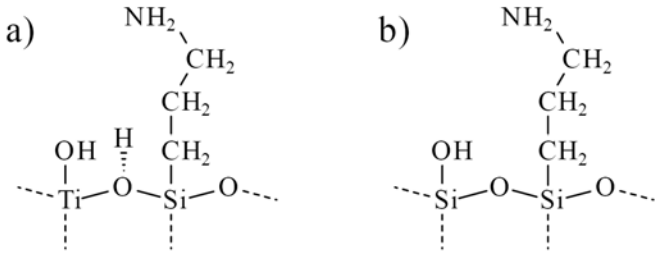

Figure 4.2. Scheme of aminopropyl functionalized surfaces: (a)titania and (b)silica. APTES replaces a surface Ti atom in (a), and a silanol group in (b).

amino-propyl group. In combination with experiments, the present simulations provide a complete picture of the surface behavior [3].

4.2 Methodology

Density Functional Theory (DFT) calculations were carried out within both the Born-Oppenheimer and the Car-Parrinello [23] approaches, using the parallel codes included in the Quantum-ESPRESSO package [24], which is based on DFT, periodic-boundary conditions, plane-wave basis sets, and pseudopotentials to represent the ion-electron interactions. The Kohn-Sham orbitals and charge density were expanded in plane waves up to a kinetic energy cutoff of 25 and 200 Ry, respectively. The Perdew-Wang (PW91) approach to the exchange-correlation energy [25,26] and Vanderbilt ultrasoft pseudopotentials [27] were adopted to compute the total energies and forces. In our simulations the Ti and Si oxide surfaces were modeled using, respectively, anatase(101) and β-cristobalite (111) slabs, four layers deep. Molecular dynamics simulations were carried out within the Car-Parrinello method [23] in a microcanonical ensemble, at around 300K and using a time step of 0.17 fs. Reciprocal space sampling was restricted to the Γ-point.

4.3 Experimental analysis: surface chemistry as a function of pH

In the context of the XPS technique, X-Rays are emitted from the source and penetrate into the surface to a depth of the order of a micrometer, interacting with the core electrons of the sample [28]. The specific energy value required to remove a core electron with respect

[3]These results have been compiled in an article published in the journal Chemistry of Materials, see reference [21].

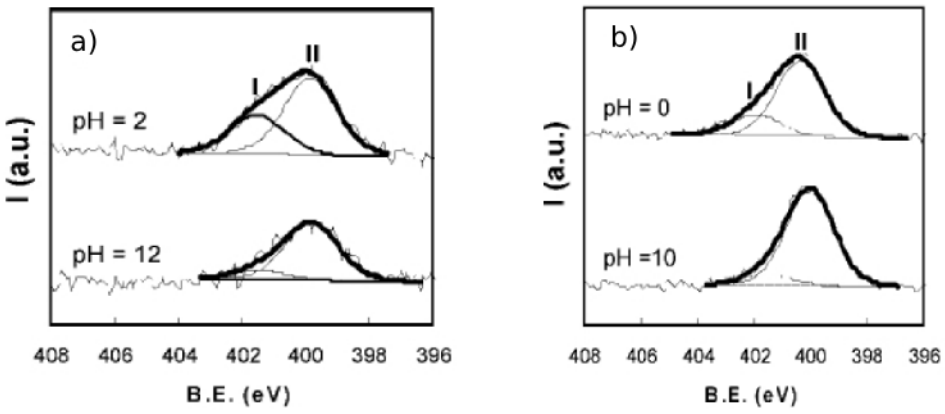

Figure 4.3. XPS N 1s spectra of (a) TiO_2 and (b) SiO_2 hybrid films submitted to extreme pH values (indicated in each curve). Fitted peaks I and II resulting of signal deconvolution are shown in thin lines.

to the Fermi level is called Binding Energy (BE), and is characteristic of each particular atom. Therefore, every peak obtained in the XPS spectra is related to a specific type of atom.

Along this work, XPS measurements were used to identify the chemical speciation of the aminopropyl functional surface groups. This experimental data was obtained in the laboratory of F. Williams and G. Soler Illia [21]. We note that XPS measurements probe not only the N-containing functional groups attached to the topmost layer, but also nitrogenated functional groups inserted in the top layers of the solid matrix.

Figure 4.3 shows representative N 1s XPS spectra for aminopropyl functionalized films of mesoporous silica and titania in extreme pH conditions. In both cases, the N 1s XPS signal contains two components at $\sim$402 and $\sim$400 eV in the BE spectrum (peaks I and II, respectively). On the basis of their BE position and behavior with pH, both peaks can be attributed to ammonium (Peak I, -NH_3^+ at 402 eV) and amino (Peak II, -NH_2 at 400 eV) species in agreement with previous reported values [29].

Figure 4.4 shows the integrated peak area ratio R = [-NH_3^+]/[-NH_2] as a function of pH for SiO_2 and TiO_2 films. Measurements performed on Si-supported thin films (full symbols) or on powder scratched films, presenting all possible orientations (open symbols) lie on the same curve. Observing this graphic, two trends can be immediately distinguished: (a) R decreases as the pH increases for all systems, and (b) the pH dependence of R changes with the chemical nature of M. These trends will be separately discussed below.

The first observation reflects the acidic character of the -NH_3^+ groups in TiO_2 and SiO_2 films: as pH increases, the fraction of protonated amino groups (and therefore R) decreases, due to proton release from ammonium. Two differences can be observed with respect to soluble ammonium salts: (i) the speciation changes from ammonium to amine

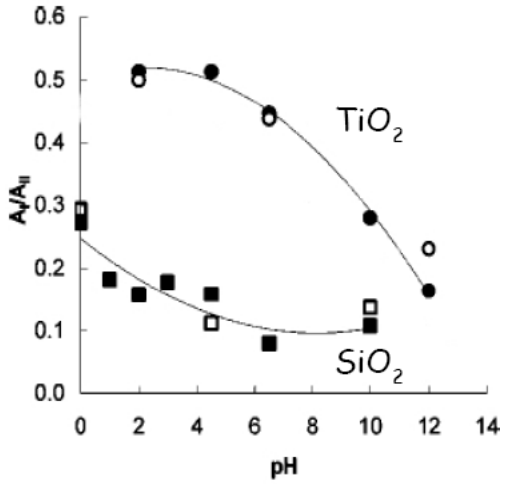

Figure 4.4. Evolution of the R = A_I/A_{II} peak intensity ratio with pH. Squares, M = Si; and circles, M = Ti. Closed symbols represent XPS analysis on deposited films; open symbols, analysis on scratched films. Curves in the Figure are a guideline to the eye.

take place at relatively low pH values (ca. 1-2 for SiO_2 and 6-8 for TiO_2), and the acidity of the ammonium group is higher compared to soluble propylammonium, with a pKa value of 10.71; (ii) the R value changes in a broader pH range than the one corresponding to ammonium-amino in solution. These differences between propylamonium surface acidity with respect to the one exhibited in solution can be explained as a result of the variation in the chemical environment. The existence of surface charged groups as well as the ultra high vacuum conditions at which the XPS data was collected, may influence the relative stability of the -NH_3^+ group with respect to -NH_2.

The second point to discuss is the different pH dependences of R with the chemical nature of M. According to Figure 4.4, the effective acidity of the ammonium group in these mesoporous matrices is greater for SiO_2 than for TiO_2. This seems to correlate with the surface acidity of the corresponding MO_2 oxides. Although surface pKa values present a large variability, isoelectric point values (pH_{iep}) of the -M-OH surface groups can be an indicator to understand this trend. Silica and titania surfaces have reported pH_{iep} values of 2 and of 6-7, respectively [30]. Higher pH_{iep} values imply less acidic hydroxyl surface groups (-M-OH), i.e., the interface becomes negatively charged at higher pH.

4.4 Molecular Modelling

To get a microscopic insight into the state of the aminopropyl functions, DFT calculations were carried out on the model structures of the substituted SiO_2 β-cristobalite (111) and TiO_2 anatase (101) surfaces described above. Geometry relaxations started from zwitteri-

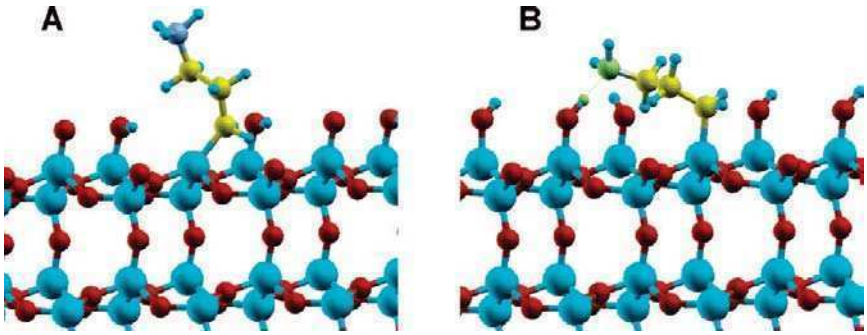

Figure 4.5. Initial (A) and relaxed (B) structures of a aminopropyl substitued SiO_2 surface, as obtained from DFT calculations in vacuum. The optimized geometry (B) exhibits a hydrogen bond between the M-OH and the -NH2 functional groups. Atoms involved in the H-bond are depicted in green.

onic configurations for the aminopropyl moiety, show that the -NH_3^+ function collapses on the surface to irreversibly transfer a proton to a neighboring M-O^- group (see Figure 4.5).

According to this result, the amino must be the predominant species at high pH values, when the surface is negatively charged because of the ionization of the -M-OH groups. This gas phase results are in agreement with the XPS results collected in high vacuum. In other words, these results support the idea that deprotonation of M-OH sites at pH > pH_{iep} leads to a strong interaction between M-O^- groups and the less acidic propylammonium, which may actually "bend" onto the surface. The bending interaction is observed for both titania and silica surfaces. Figure 4.5 shows the initial and the optimized configurations for the silica model. If this bending could be controlled via the pH of the medium, this mechanism might be used to regulate the accessible volume of the pore. However, we will see below that this bending effect dissapears in the presence of water.

In the limit of high vacuum, simulation results show that -NH_3^+ groups in the vicinity of -M-O^- groups are unstable, leading to -NH_2 and -M-OH. Below pH_{iep}, the -M-O^- groups become -M-OH groups, which can coexist with -NH_3^+ functions. According to Figure 4.4, the concentration of -NH_2 on the silica surface is significantly above [-NH_3^+] for all the range of pH. This is also true for the titania surface, except for very low pH values. This predominance of the amino with respect to ammonium is possibly reflecting the vacuum conditions corresponding to the XPS measures, which favor the neutralization of the zwitterionic state. Even so, the curves in Figure 4.4 are sensitive to pH, and also to the nature of the M-OH groups, both of which seem to determine the state of charge of the surface (Figure 4.1). The fact that a dependence with pH and with the chemical composition of the surface is seen in XPS, indicates that the degree of protonation of the oxide in solution is partially preserved under the XPS chamber conditions.

Under the experimental conditions corresponding to the XPS measurements, we can

not rule out the possibility that a small amount of water, present during the preparation of the sample, remain attached to the surface, affecting to some extent the -NH_3^+/M-O^- equilibrium. To assess the feasibility of proton transfer in the presence of adsorbed solvent, molecular dynamics simulations including up to two water monolayers were performed at $\sim$300 K on the silica and titania surfaces. Two different runs starting from different (random) configurations were carried for both surfaces. In the case of silica, these simulations showed that the transfer still proceeds through a concerted pathway resembling the well-known Grotthus mechanism for proton transfer. The -NH_3^+ moiety yields a proton to a proximate water molecule, which in turn transfers a second proton to the -M-O^- surface group. This transfer is verified within a few picoseconds of simulation and leads to the formation of -NH_2 and M-OH, which now are not in direct contact. These calculations reinforce the proposed model, where the amino functions are prevalent, even in the presence of some water surface layers. This process is illustrated in Figure 4.6 for one of the simulations performed: the distances involving the transferred protons are plotted as a function of time. H_a, initially bonded to the ammonium group, is transferred to a water molecule. In turn, this water releases one of its protons, H_b, which is accepted by the -M-O^- moiety. This mechanism indicates that the effect is not necessarily local; that is, the proton exchange may occur between groups which are not next to each other on the surface.

This proton transfer reaction was not observed on the titania model during the elapsed simulation time of around 4 ps. The typical sampling times accessible to first-principles molecular dynamics are too short to observe processes with barriers over a few kT. We expect, however, that the proton transfer must be thermodinamically feasible, since the isoelectric point of this surface is higher than that of silica [30].

We stress that in this system the ammonium and the hydroxyl groups are only partially solvated, representing some intermediate situation in between the vacuum and the bulk limits. During the simulation time, the aminopropyl chain was not observed to bend toward the surface, as in the case of the gas phase relaxation. Longer simulations might be needed to assess the average state of the functional group in the presence of water monolayers, however, our results suggest that in the process of solvation of the -NH_2 and -M-OH functions, H-bonds established with water molecules diminish the chances that these two groups be in direct contact.

4.4.1 Counterions effect on the speciation of the amino group

It might be expected that ions present in the experimental conditions, remaining from the synthesis, may have a screening effect with respect to surface charged groups, contributing to stabilize the charges and inhibiting the proton transfer. In the following, we examine

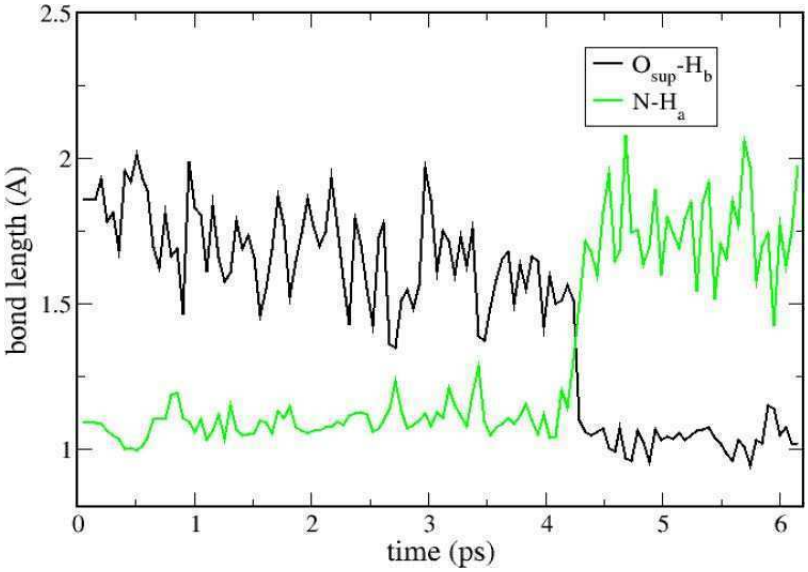

Figure 4.6. N-H_a and O_{sup}-H_b distances as a function of time according to a DFT molecular dynamics simulation on the functionalized silica surface, including two water monolayers. At zero time the system contains one -NH_3^+ group and one -M-O^- function. H_a is initially bonded to the ammonium group, while H_b belongs to one of the water molecules acting as an intermediate. A concerted proton transfer resembling the Grotthus mechanism takes places at around 4.2 ps, to produce -NH_2 and -M-OH groups.

this counterion effect on the ammonium group by including a pair of ions in the simulation: Na^+ and Cl^-, to preserve electroneutrality. Particularly, we placed the Cl^- anion near the -NH_3^+ group, in a configuration that would favor the electrostatic stabilization of the ammonium, minimizing the probability of a proton transfer event. Molecular dynamics simulations were performed under the same conditions as those adopted before, except for the incorporation of these ions. However, also in this case we found that the -NH_3^+ group turns out to be unstable in the presence of the -M-O^- function: a proton transfer from -NH_3^+ to -Si-O^- proceeds through the Grotthus mechanism, involving two water molecules in the pathway between the ammonium and the silanol. In Figure 4.7 it can be seen that the proton transfer is accomplished within the first 4.7 ps of dynamics. It is apparent that the counterions, at the conditions examined in the simulations, do not provide an additional stabilization to the ammonium group capable to inhibit the proton transfer. We note that the simulated conditions amount to a surface concentration of 1.3 ion pairs per nm^2, which is a quite high value presumably above the experimental concentration. Hence, according to these results, we can expect the counterions will not modify the acidic behavior significantly.

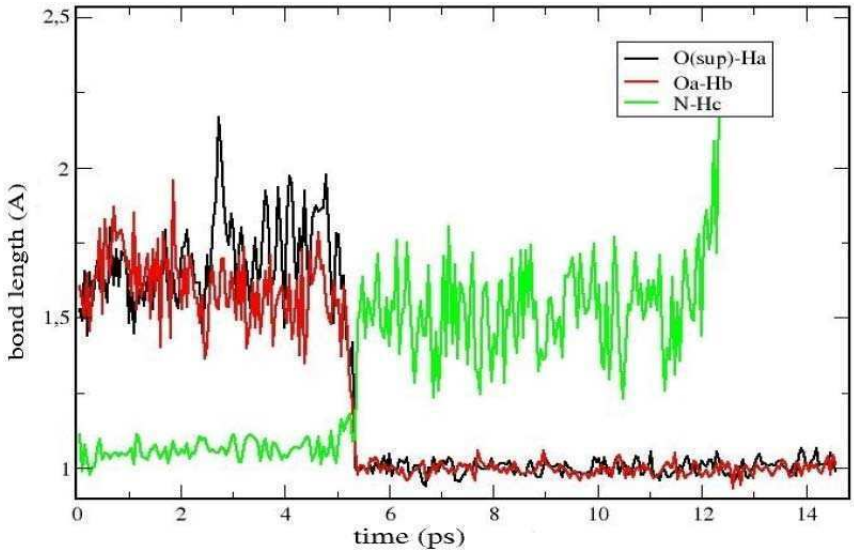

Figure 4.7. N-H_a and O_{sup}-H_b distances as a function of time according to a DFT molecular dynamics simulation on the functionalized silica surface, including two water monolayers and a pair of ions: Na^+ and Cl^-. At zero time the system contains one -NH_3^+ group and one -M-O^- function. H_c is initially bonded to the ammonium group, while H_b, H_a and O_a belong to water a and water b molecules that are acting as intermediates. A concerted proton transfer resembling the Grotthus mechanism takes places at around 4.7 ps, to produce -NH_2 and -M-OH groups.

4.5 Final remarks

These calculations have shown that charged propyl-ammonium is not stable in the presence of ionized hydroxil groups on silica and titania surfaces. This is observed in the gas phase, but also in the presence of a water bilayer for silica surface, and at high concentrations of counterions. These simulations have contributed to rationalize XPS measurements of the variation of the ratio $R = [-NH_3^+]/[-NH_2]$ with pH and with the nature of M. Combination of experiments and simulations have thus allowed for a complete model of the surface behavior.

From experimental measurements, it turns out that the ammonium/amino ratio decreases as pH increases. This is of course related to the acidity of the organic function, but this dependence is modulated by the nature of the inorganic oxide. In other words, the acidity (or the pH_{iep}) of the oxide dictates the degree of protonation of the surface -M-OH groups, which in turn determines the state of the aminopropyl functions. A high density of -M-O^- surface anions will promote the deprotonation of the ammonium groups, and for this reason the ratio R is shifted to lesser values with respect to aminopropyl in aqueous solution. In the same way, the lower the isoelectric point of the oxide, the smaller the concentration of ammonium at a given pH.

Experiments discussed in this chapter probe the combined effects of the pH of the solu-

tion and the surface charge on the ammonia-amino ratio. On the other hand, simulations can explore the second effect, but not the first one: while the surface charge may be easily set in a simulation, the pH of the medium is a macroscopic parameter, whose representation in an atomistic framework is far from straightforward. To consider the proton concentration explicitly, a huge simulation cell would be needed. For example, a solution at pH = 2 (neglecting activity coefficients) implies a concentration of nearly one proton in 200 nm^3. Simulation cells used in first-principles calculations are typically between one and two orders of magnitude below this size. Even if a cell of this size were affordable, a single H^+ in the system would possibly not be an accurate representation of an aqueous solution of pH = 2.

In any case, the discrimination of effects which can be attained by simulations, is not always possible in experiments. While in simulations we are usually examining simplifications of the real chemical system, such simplifications may at the same time be helpful to examine how every single factor affects the behavior. Of course, at the time of analyzing these results, it is important to recall that the whole is not always the sum of its parts.

References

[1] M. Davis, *Nature* 417, (2002), 813.

[2] G. J. de A. A. Soler-Illia, C. Sanchez, B. Lebeau, and J. Patarin, *Chem. Rev.* 102, (2002), 4093–4138.

[3] G. Férey, *Chem. Soc. Rev.* 37, (2008), 191.

[4] J. Lee, M. C. Orilall, S. C. Warren, M. Kamperman, F. J. Disalvo, and U. Wiesner, *Nat Mater* 7, (2008), 222.

[5] P. C. Angelomé and G. J. de A. A. Soler-Illia, *Chem. Mater. 2005, 17, 322-331* 17, (2005), 322–331.

[6] J. L. Shi, Z. L. Hua, and L. X. Zhang, *J. Mater. Chem.* 14, (2004), 795.

[7] G. J. A. A. Soler-Illia and P. Innocenzi, *Chem. Eur. J.* 12, (2006), 4478.

[8] M. Etienne, A. Quach, D. Grosso, L. Nicole, C. Sanchez, and A. Walcarius, *Chem. Mater.* 19, (2007), 844.

[9] S. L. Burkett, S. D. Sims, and S. Mann, *Chem. Commun.* page 1367.

[10] M. H. Lim, C. F. Blanford, and A. Stein, *J. Am. Chem. Soc.* 119, (1997), 4090–4091.

[11] A. Stein, B. J. Melde, and R. C. Schroden, *Adv. Mater.* 12, (2000), 1403.

[12] J. Liu, Y. Shin, Z. Nie, J. H. Chang, L.-Q. Wang, G. E. Fryxell, W. D. Samuels, and G. J. J. Exarhos, *Phys. Chem. A* 104, (2000), 8328.

[13] V. Dufaud and M. E. Davis, *J. Am. Chem. Soc.* 125, (2003), 9403.

[14] N. Liu, R. A. Assink, B. Smarsly, and C. J. Brinker, *Chem. Commun.* page 370.

[15] M. R. Newton, A. K. Bohaty, H. S. White, and I. Zharov, *J. Am. Chem. Soc.* 127, (2005), 7268.

[16] H. H. P. Yiu and P. A. Wright, *J. Mater. Chem.* 15, (2005), 3690.

[17] D. Fattakhova-Rohlfing, M. Wark, and J. Rathouský, *Chem. Mater.* 19, (2007), 2640.

[18] R. P. Bagwe, L. R. Hilliard, and W. Tan, *Langmuir* 22, (2006), 4357.

[19] J.-J. Shyue, M. R. D. Guire, T. Nakanishi, Y. Masuda, K. Koumoto, and C. N. Sukenik, *Langmuir* 20, (2004), 8693.

[20] J.-P. Jolivet, *Metal Oxide Chemistry and Synthesis*, John Wiley & Sons (**2000**).

[21] A. Calvo, P. C. Angelomé, V. M. Sánchez, D. A. Scherlis, F. J. Williams, and G. J. A. A. Soler-Illia, *Chem. Mater.* 20, (2008), 4661–4668.

[22] B. V. Zhmud and A. B. Pechenyi, *J. Colloid Interface Sci.* 173, (1995), 71.

[23] R. Car and M. Parrinello, *Phys. Rev. B* 55, (1985), 2471–2474.

[24] P. Giannozzi, S. Baroni, N. Bonini, M. Calandra, R. Car, C. Cavazzoni, D. Ceresoli, G. L. Chiarotti, M. Cococcioni, I. Dabo, A. D. Corso, S. de Gironcoli, S. Fabris, G. Fratesi, R. Gebauer, U. Gerstmann, C. Gougoussis, A. Kokalj, M. Lazzeri, L. Martin-Samos, N. Marzari, F. Mauri, R. Mazzarello, S. Paolini, A. Pasquarello, L. Paulatto, C. Sbraccia, S. Scandolo, G. Sclauzero, A. P. Seitsonen, A. Smogunov, P. Umari, and R. M. Wentzcovitch, *J. Phys.: Condens. Matter* 21, (2009), 395502.

[25] J. P. Perdew and Y. Wang, *Phys. Rev. B* 45, (1992), 13244.

[26] J. P. Perdew and et al, *Phys. Rev. B* 46, (1992), 6671.

[27] D. Vanderbilt, *Phys. Rev. B* 41, (1990), 7892–7895.

[28] J. C. Vickerman, *Surface Analysis - The principal Techniques*, John Wiley & Sons (**2005**).

[29] J. J. Shyue, M. R. De Guire, T. Nakanishi, Y. Masuda, K. Koumoto, and C. N. Sukenik, *Langmuir* 20, (2004), 8693.

[30] M. Kosmulski, *J. Colloid Interface Sci.* 253, (2002), 77.

Chapter 5

Continuum solvent model for first principles molecular dynamics at solid-liquid interfaces

Including the solvent in first-principles simulations Most chemical processes of basic and technological relevance, from acid-base equilibrium to enzymatic catalysis and electrochemistry, take place in a solvent environment. For this reason, inclusion of the solvation effects in the framework of different computational methodologies has been a very active line of research in the last two decades. To a first approximation, there are two ways to incorporate the solvent into the simulation scheme: (i) adding the solvent molecules explicitly, or (ii) representing them through a continuum dielectric medium.

In comparison to the second choice, the first one comes with the remarkable advantage that specific solute-solvent interactions are taken into consideration. This is specially important when strong, directional interactions such as hydrogen bonds are present. On the other hand, the obvious drawback about this approach is the increment of the computational cost. This rise in the cost has two major causes: on one hand, there is the increment of the number of atoms in the simulation. On the other, with this increment in degrees of freedom, a converged sampling of all the configurations associated with the liquid state is needed to represent the fluid phase. The liquid state involves an enormous number of local minima very close in energy, and therefore long molecular dynamics (MD) or extensive Monte Carlo (MC) simulations at finite temperature are required to get converged averages over a representative ensamble of configurations. A single optimized structure (or a limited number of them) will reflect the frozen phase rather than the liquid.

Quantum Mechanics-Molecular Mechanics methods (QM-MM) can be used to reduce the computational cost, still keeping an explicit solvation framework able to capture the specific solute-solvent interactions. Within the context of QM-MM hybrid schemes (see chpater 7) the solute and the solvent are treated with quantum and classical mechanics respectively. While this approach still requires long molecular dynamics or Monte Carlo

sampling, the major part of the system is represented with empirical potentials, which implies significant savings in terms of computer time.

The continuum solvent model, which is the approach we implement and discuss in this chapter, describes the polarization effect of the solvent in an averaged way. The solvent molecules are replaced by a continuum dielectric medium with a single permittivity (or dielectric constant), which is set equal to the value of the solvent in the bulk phase. One major advantage of this representation relays on keeping the same amount of atoms as in vacuum, and on the possibility of performing geometry optimizations that reflect equilibrium geometries in solution, since the dielectric represents the solvent effect in an average fashion. As a consequence of not considering the solvent structure, specific solute-solvent interactions are neglected. When needed, this problem can be in part avoided by the inclusion of an appropriate amount of solvent molecules around the QM system. Usually, this is done by annexing the first solvation shell explicitly, which in general has a well defined geometry as a result of the strong solute-solvent reciprocal action.

In particular, we are interested in the description of solid-liquid interfaces. For a broad range of applications, the relevant phenomena occur in the presence of a liquid phase, as is often the case in processes related to electrochemistry and catalysis. The realization of liquid phase DFT simulations is therefore a much pursued objective—especially when many of the standard x-ray techniques such as XPS or LEED are unsuited to provide atomic scale information in solution. It is possible to find in the literature a few number of studies in which one or several layers of water molecules are incorporated to represent the solvent (see for example ref. [1] or [2]), but the explicit inclusion of solvent molecules considerably increases the cost of first-principles calculations of periodic surfaces and is therefore a rather uncommon practice. In recent years a small number of implementations of the continuum model have been proposed in the context of DFT and periodic boundary conditions, based on plane-wave basis sets, and the Car–Parrinello method [3–6]. To the best of our knowledge, none of them have been employed in molecular dynamics simulations of periodic surfaces.[1] Along this chapter, we present a continuum model formulation designed for ab-initio molecular dynamics simulations at solid-liquid interfaces. In the first place, we outline the general ideas behind continuum solvent models. Secondly, we briefly introduce a previous scheme which has been considered as the starting point for the current implementation. Next, the model is presented in detail, including the numerical

[1] T. Arias and co-workers have devised a form of density functional theory for the self-consistent embedding of quantum-mechanical systems in a dielectric medium. This approach has been applied to investigate the atomic and electronic structure of the Cr_2O_3 surface in solution by means of static calculations. See [7,8]. Also zero temperature simulations were performed by Wang and Liu [9], who implemented a continuum solvation model based on the Fattebert and Gygi work [4] in the SIESTA package [10]. This approach was used to study the formic acid oxidation at Pt/H_2O interface [9] and the catalytic pathways of oxygen on anatase in an aqueous surroundings [11].

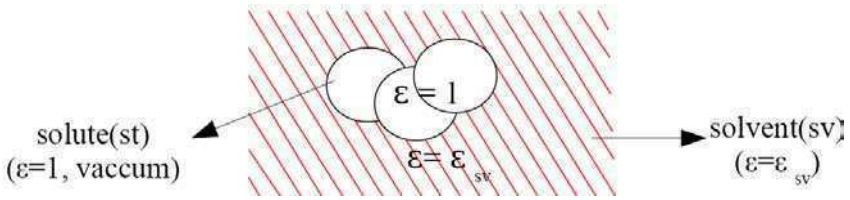

Figure 5.1. Contiuum solvent scheme: a boundary surface is defined around the solute to delimitate the space filled by the dielectric medium.

machinery used to address the electrostatic problem. To finish, the performance of the model is examined in the light of molecular dynamics on the TiO_2-anatase surface. [2]

5.1 The continuum solvent model: an overview and previous implementation

As it was already mentioned, the continuum model considers the polarization effect of the solvent in an average manner, by the embedding in dielectric medium. Within this framework, the dielectric fills the space outside a cavity where the solute is confined. This is schemed in Figure 5.1

In what follows we adopt the definition introduced by Ben-Naim [13] for the solvation free energy ΔG_{solv} as corresponding to the process of transferring the solute molecule from a fixed position in the gas phase to a fixed position in the solution at constant temperature, pressure, and chemical composition. In this context, the interaction between solvent and solute can be conceived as a sum of three different contributions:

$$\Delta G_{solv} = \Delta G_{el} + \Delta G_{cav} + \Delta G_{dis-rep} \tag{5.1}$$

The first term on the right hand side accounts for the electrostatic part of the solvation free energy, which considers the interaction between the dielectric and the charge distribution of the solute. This one constitutes the dominant contribution for polar and charged solutes. The second term is known as the cavitation energy and denotes the energy involved in creating a cavity inside the solvent, overcoming the surface tension. The last term gathers the dispersive London attraction and the quantum-mechanical repulsion between the solvent and solute molecules. This dispersion-repulsion energy may be important in the case of bulky and highly polarizable molecules, as hydrophobic and aromatic species. It is much smaller than the other two for the kind of solutes considered in this study, and so this

[2] Results in this chapter are reported in an article appeared in the Journal of Chemical Physics, reference [12].

term is neglected in our model. Moreover, since the model is parametrized to reproduce experimental solvation energies, the dispersive-repulsive effect is partly captured by the the electrostatic term. It should be noticed that since none of these terms can be directly measured in experiments, these contributions are constructions of the model. Only the sum of all of them, ΔG_{solv}, is a mensurable physical quantity.

5.1.1 Cavitation energy

It is defined as the work involved in creating the appropiate cavity inside the solution to contain the solute, in the absence of solute-solvent interactions [14]. Different approaches exist to calculate this contribution; the unavailability of experimental values makes it difficult to assess their accuracy. In principle, ΔG_{cav} depends only on the properties of the solvent and on the shape of the cavity. Macroscopic variables as temperature and pression will as well have an influence on the energy needed to create a cavity. There are two main pathways to compute ΔG_{cav}, depending on how the solvent is described, namely, based on the solvent cavity surface, or on a statistical mechanics approach for the liquid state. In the last situation the scaled particle theory (SPT) is generally used, which characterizes the solvent molecules as hard spheres, with radii suitably modified through a scaling procedure to satisfy some macroscopic experimental quantities. In this context, the cavitation energy is thought as the work involved in excluding the center of solvent molecules around a specific region. For nonspherical cavities the Pierotti-Claverie formula [15, 16], where every single sphere in the SPT term is weighted by its area exposed to the solvent, is expressed as:

$$\Delta G_{cav} = \sum_{k=1}^{N} \frac{A_k}{4\pi R_k^2} G_{cav}(R_k) \tag{5.2}$$

Equation 5.2 defines the cavity as the volumen occupied by N interlocked spheres centered on the atoms k. R_k and A_k are, respectively, the van der Waals radius and the area exposed to the solvent of atom k, and $G_{cav}(R_k)$ represents the cavitation free energy due to the creation of a spherical cavity of radius R_k according to Pierotti's definition. [17].

From a macroscopic perspective based on the solvent surface tension γ , Uhlig [18] defined the ΔG_{cav} as a product between γ and the area of the sphere, $\Delta G_{cav} = 4\pi R^2\gamma$. While this is strictly valid for macroscopic size spheres, the theory of Tolman for the surface tension of a droplet [19] demonstrates that the formula for γ does not change significantly with the cavity size. In fact, this "microscopic surface tension"equals the macroscopic γ minus a corrective term inversely proportional to the radius of the cavity. In the present model the cavitation energy is defined as the product of the surface tension and the area of the cavity, $S(\rho_0)$ [6]:

$$\Delta G_{cav} = \gamma S(\rho_0) \tag{5.3}$$

A practical way to define the boundaries of the cavity is by an isosurface of the charge density corresponding to a density threshold ρ_0. The choice of ρ_0 determines the extension of the cavity: since the charge density ρ decays away from the molecule, the lower ρ_0, the larger the cavity. Numerically, the cavity area can be calculated as the volume of a thin film delimited between two close values of ρ (slightly above and below ρ_0), divided by its thikness. This idea was proposed by Cococcioni et al [20] to define a "quantum surface" in the context of extended electronic-enthalpy functionals. The surface can be expressed as:

$$S(\rho_0) = \int d\mathbf{r}\{\upsilon_{\rho_{0-\Delta/2}}[\rho(\mathbf{r})] - \upsilon_{\rho_{0+\Delta/2}}[\rho(\mathbf{r})]\} \times \frac{|\nabla\rho(\mathbf{r})|}{\Delta} \tag{5.4}$$

where Δ determines the separation between the two isosurfaces, with $\rho_{0-\Delta/2}$ and $\rho_{0+\Delta/2}$ being the density thresholds associated with the external and internal isosurfaces, respectively. The ratio $\Delta/|\nabla\rho(\mathbf{r})|$ is the spatial separation between the isosurfaces. If υ is a smoothed step function,

$$\upsilon[\rho(\mathbf{r})] = \frac{1}{2}\left[\frac{(\rho(\mathbf{r})/\rho_0)^{2\beta} - 1}{(\rho(\mathbf{r})/\rho_0)^{2\beta} + 1} + 1\right] \tag{5.5}$$

then the volumen of the cavity can be formulated as the integral over the space of the step function:

$$V_c(\rho_0) = \int \upsilon_{\rho_0}[\rho(\mathbf{r})] \tag{5.6}$$

Due to the dependence of the ΔG_{cav} on the electronic density, a new term appears in the Kohn-Sham potential,

$$\frac{\delta\Delta G_{cav}}{\delta\rho}(\mathbf{r}) = \frac{\gamma}{\Delta} \times [\upsilon_{\rho_{0-\Delta/2}}[\rho(\mathbf{r})] - \upsilon_{\rho_{0+\Delta/2}}[\rho(\mathbf{r})]] \times \left[\sum_i \sum_j \frac{\delta_i\rho(\mathbf{r})\delta_j\rho(\mathbf{r})\delta_{ij}\rho(\mathbf{r})}{|\nabla\rho(\mathbf{r})|^3} - \sum_i \frac{\delta_i^2\rho(\mathbf{r})}{|\nabla\rho(\mathbf{r})|}\right] \tag{5.7}$$

where the indices i and j run over the x, y and z coordinates. Up to here, there are two adjustable parameters: ρ_0 and Δ. Whereas the former establishes the size of the cavity (eq. 5.4), the later can take any value provided it is large enough to minimize the numerical noise, but small enough to render an accurate measure of the surface. In reference [6] it is remarked, on one hand, that the cavity area is quite insensitive to the value of Δ within a large range, and on the other, that for a given Δ, the calculated areas change about 25% for an increment of 3 times in ρ_0. Figure 5.2, taken from that work, illustrates this behavior.

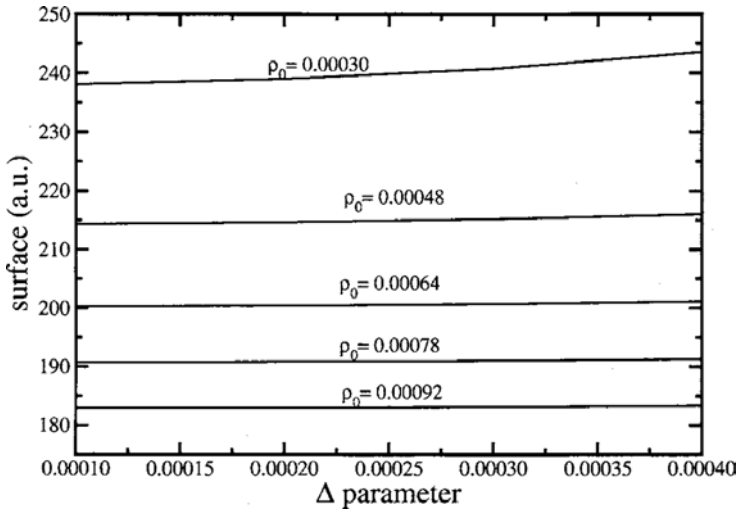

Figure 5.2. ΔG_{cav} dependence on Δ parameter for different ρ_0 values in a water molecule. Taken from Scherlis et al. [6].

5.1.2 Electrostatic energy: the dielectric constant as a function of the electronic density

The electrostatic interaction can be calculated as proposed by Fattebert and Gygi [4, 21], who defined the dielectric constant ϵ as a smooth function of the electronic density of the system. As exposed in chapter 2, the total DFT energy within a pseudopotential framework and in periodic boundary conditions can be written as:

$$E[\rho] = T[\rho] + E_{XC} + \frac{1}{2}\int \phi(\mathbf{r})\rho_{tot}(\mathbf{r})d\mathbf{r} + \sum_{I<J}\frac{Z_I Z_J}{R_{IJ}} erfc\left(\frac{R_{IJ}}{\sqrt{(R_I^c)^2+(R_J^c)^2}}\right)$$
$$-\frac{1}{\sqrt{2\pi}}\sum_I \frac{Z_I^2}{R_c^I} + E_{PS}[\rho] \tag{5.8}$$

where $T[\rho]$ denotes the electronic kinetic energy, and E_{XC} the exchange-correlation energy. The sum of the last four terms in the right hand side of the equation accounts for the total electrostatic energy in a crystal, considering the full interaction between nuclei and electrons.[3] The non-local part of the pseudopotential is omitted since it is does not need to be taken into consideration in the solvation effects.

The third term is called the Hartree energy:

[3]The last four terms on the right hand side of this equation are equivalent to the electrostatic energy in equation 2.99. The cutoff radius R_c^I is equal to $1/\sqrt{2}\eta$ in 2.99.

$$E_H = \frac{1}{2}\int \phi(\mathbf{r})\rho_{tot}(\mathbf{r})d\mathbf{r} \tag{5.9}$$

where ρ_{tot} represents the sum of electronic plus ionic charge densities [4], and the electrostatic potential ϕ is the solution to the Poisson equation in vacuum,

$$\nabla^2\phi(\mathbf{r}) = -4\pi\rho_{tot}(\mathbf{r}) \tag{5.10}$$

In the presence of a dielectric continuum with a permittivity $\epsilon[\rho]$, the Poisson equation becomes

$$\nabla\cdot(\epsilon[\rho]\nabla\phi(\mathbf{r})) = -4\pi\rho_{tot}(\mathbf{r})\ . \tag{5.11}$$

Using equation 5.11, the formula for the Hartree energy E_H, can be integrated by parts to yield:

$$E_H = \frac{1}{8\pi}\int \epsilon[\rho](\nabla\phi(\mathbf{r}))^2 d\mathbf{r}. \tag{5.12}$$

As a result of the dependence on the electronic density, an extra term, the functional derivative of E_H with respect to the charge density, has to be added to the Kohn-Sham potential $V^{KS}[\rho]$,

$$\frac{\delta E_H}{\delta\rho}(\mathbf{r}) = \phi(\mathbf{r}) + V_\epsilon(\mathbf{r}), \tag{5.13}$$

$$V_\epsilon(\mathbf{r}) = -\frac{1}{8\pi}(\nabla\phi(\mathbf{r}))^2\frac{\delta\epsilon}{\delta\rho}(\mathbf{r}). \tag{5.14}$$

The dielectric medium and the electronic density respond self-consistently to each other through the dependence of ϵ on ρ and vice versa.

In quantum chemistry continuum models as PCM [15], the dielectric constant ϵ is a step function taken to be 1 inside the cavity, and a fixed value outside. For molecular dynamics applications, such a discontinuity needs to be removed to calculate accurately the analytic derivatives of the potential with respect to the ionic positions. Besides, in the particular case of plane-waves implementations based on real space grids, a smoothly varying dielectric function is more appropriate for numerical reasons. Fattebert and Gygi proposed the following smoothed step function for the dielectric:

$$\epsilon(\rho(\mathbf{r})) = 1 + \frac{\epsilon_\infty - 1}{2}\left(1 + \frac{1-(\rho(\mathbf{r})/\rho_0)^{2\beta}}{1+(\rho(\mathbf{r})/\rho_0)^{2\beta}}\right). \tag{5.15}$$

This function asymptotically approaches ϵ_∞ (the permittivity of the bulk solvent) in

[4] This was outlined in chapter 2. This term is equivalent to Eq. 2.77.

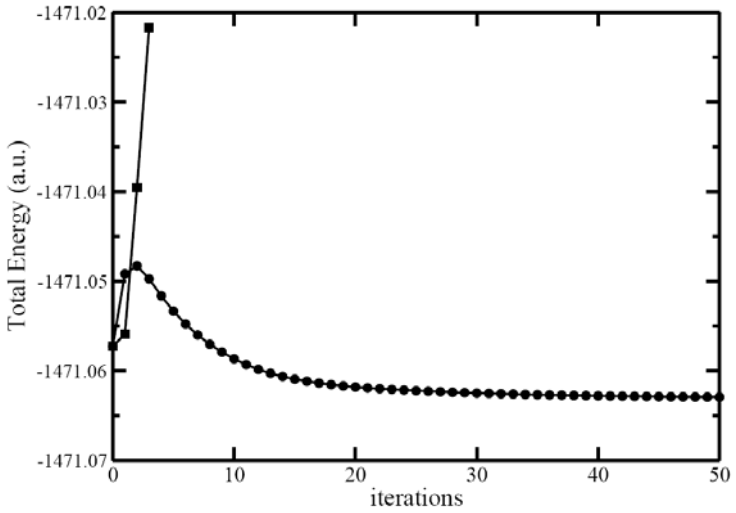

Figure 5.3. Total energy during two different Car-Parrinello electronic minimizations in a continuum solvent (the structure is the TiO2 slab in Figure 5.10). The squares indicate the results for a dielectric function depending on the charge density, whereas the circles correspond to the same computational experiment, but removing V_ϵ from the total potential (see text). Both runs used the same calculation parameters and were restarted from the wavefunction converged in vacuum.

regions of space where the electron density is low, and 1 in those regions where it is high (inside the solvation cavity). The parameter ρ_0 is the density threshold determining the cavity size, whereas β modulates the smoothness of the transition from ϵ_∞ to 1. This function described in equation 5.15 is in concordance with equation 5.5, where the step function υ was defined as a function of ρ.

5.2 The continuum solvent model for solid-liquid interfaces

When the scheme described above is applied on structures extended in two dimensions, it typically fails to achieve self-consistency, as shown in Figure 5.3. We found the electrons heat up during the Car-Parrinello relaxation of the wavefunction, causing the total energy to diverge. In other cases the kinetic energy of the electrons is observed to decrease at the beginning, but thereafter it experiences irregular oscillations without ever reaching zero.

The influence on the convergence of the calculation was examined for each term contributing to the Kohn-Sham potential. As a result, the source of the abnormal numerical behaviour was detected in the inclusion of the additional potential term V_ϵ. In other words, neglection of the V_ϵ term in the electronic minimization leads to a smooth convergence of the electron kinetic energy. Of course, omitting this term does not constitute an acceptable

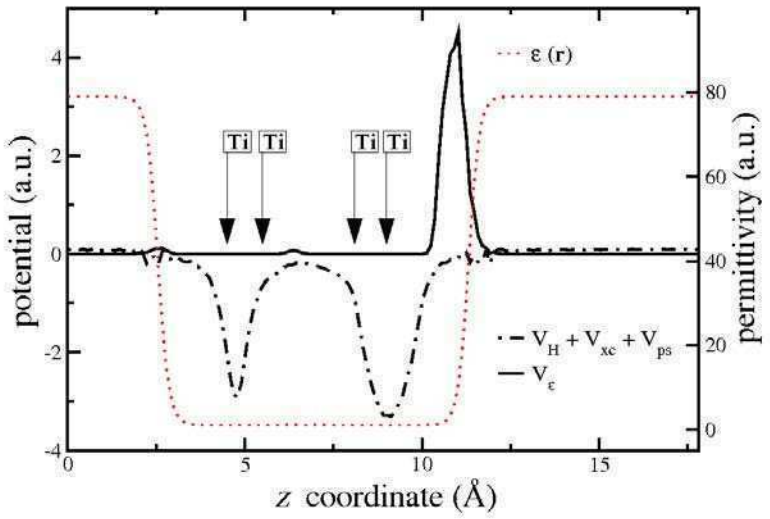

Figure 5.4. Variation of V_ϵ , the sum of all the other contributions to the KS potential and permitivitty as a function of cell position along z direction, keeping x and y fixed. [12]

solution to this problem, because energy conservation would be lost during molecular dynamics simulations. The reason for the instability associated with V_ϵ is evinced in Figure 5.4, where the dielectric contribution to the potential is plotted separately from the rest, as a function of the z-direction (perpendicular to the surface) at fixed x and y. The value of the permittivity is also shown along the same axis. In particular, these results correspond to a calculation in a slab of anatase which is described in detail in section 5.3, yet the behavior reported was similarly observed in different slabs. The x-y coordinates were selected to coincide with one of the Ti atom on the surface.

In Figure 5.4 it is possible to appreciate that V_ϵ does not represent a minor addition, but exhibits a sharp peak at the solid-liquid boundary, of a larger magnitude than all the other contributions combined. Since V_ϵ depends on $\partial\epsilon/\partial\rho$ (equation 5.14), the explosion is seen at the region where the charge density decays abruptly, producing a rapid variation in $\epsilon[\rho]$ from the value in the solid to the value in the solvent. Considering the dielectric model of equation 5.15, we have:

$$\frac{\partial\epsilon}{\partial\rho}(\mathbf{r}) = \frac{1-}{\rho_0}\frac{2\beta(\rho(\mathbf{r})/\rho_0)^{2\beta-1}}{(1+(\rho(\mathbf{r})/\rho_0)^{2\beta})^2}. \tag{5.16}$$

This expression goes to zero when $\rho(\mathbf{r}) \gg \rho_0$ or $\rho(\mathbf{r}) \ll \rho_0$, and is dominated by $1/\rho_0$ otherwise. Then the magnitude of V_ϵ ultimatly depends on the value of the density threshold ρ_0. Unfortunatly, this parameter can not be freely tuned to get rid of the blowup

in $\partial\epsilon/\partial\rho$, but is adjusted coupled with β to reproduce the experimental solvation free energies. Alternative models to describe the dielectric medium as a function of the electronic density were considered, such as gaussian or trigonometric functions of ρ. However, energy converge was not achieved in any case. None of these functions entailed any significant improvement, as far as all of them have in common a sudden change associated with the transition from 1 to ϵ_∞, which redounds in large values $\partial\epsilon/\partial\rho$ at the interface. The transition can be smoothed enough as to avoid the sharp peaks in V_ϵ, but in doing so the solvation effect is ruined. In other words, we found that a simple redefinition of the dielectric function does not suffice to recover numerical stability; we were unable to find a functional form for ϵ providing at the same time good convergence and a realistic solvation energy. The discussed behavior is a consequence of the dependence of ϵ on ρ, irrespective of the kind of function chosen to model the dielectric.

Understanding the divergence in the potential as a consequence of the dependence of the dielectric medium on the electronic density, we turned into a different strategy, i.e., to define the dielectric medium independently of the electron density. This have led to a different formulation, exposed in the next subsection 5.2.1.

5.2.1 Electrostatic energy: Dielectric constant as a function of atomic coordinates

It can be argued that convergence fails because the noise in the representation of the almost-divergent potential does not allow the system to make steps in the correct (minimum) direction. In such a case, the implementation of denser grids should bring some relief to the computational convergence. Trial runs with the number of mesh points increased up to 50% on each direction—meaning an increment of more than 3 times in the density of the real space grids—, however, didn't improve the situation in any noticeable way. This suggests exceedingly high energy cutoffs should be used to restore convergence.

In the absence of a dielectric, or for a dielectric defined independently of the charge density, the functional derivative of E_H with respect to ρ turns out to be equal to the electrostatic potential $\phi[\rho]$ (see reference [22]). The additional term V_ϵ emerges from the dependence of E_H on ϵ, which is a function of ρ, and thus, the instability of the model emanates from the self-consistency between the charge density and the dielectric. A possible alternative would be to use instead a non-self-consistent or "fake" density since the role of the charge density in this context is simply to shape the dielectric medium, omitting the dependence of the potential on the dielectric function. Such an approach, however, does not conserve the constant of motion in molecular dynamics simulations. Yet another path to relax the explicit dependence of the potential on the permittivity would be to define ϵ as a function of the atomic coordinates, which is the usual strategy in quantum

chemistry methods. The idea of a dielectric determined by the atomic positions may be less attractive from a physical viewpoint, because some advantages associated with the electronic density dependence are lost: the size and shape of the cavity depend on the identity of the atoms only, and are not longer modulated by the electronic structure or the environment; the polarization of the solvent is lost, and, on top of these, many more parameters are needed—at least one per atom.

Anyway, in practice it is possile to set up a suitable dielectric function depending on the atomic positions that reproduce the ρ-dependence solvation because the effect of the self-consistency and the polarization of the solvent on ΔG_{solv} are quite minor. In this way, we keep the expression for ϵ given in equation 5.15, but feed it with a dummy density $\gamma(\mathbf{r})$ determined by the ionic positions $\mathbf{R_I}$,

$$\gamma(\mathbf{r}) = \sum_I e^{-\left(|\mathbf{r}-\mathbf{R_I}|-R^I_{vdw}\right)}, \tag{5.17}$$

where R^I_{vdw} is the van der Waals radius for the corresponding species. Hence the dielectric function takes the following form:

$$\epsilon(\gamma(\mathbf{r})) = 1 + \frac{\epsilon_\infty - 1}{2}\left(1 + \frac{1-\gamma(\mathbf{r})^{2\beta}}{1+\gamma(\mathbf{r})^{2\beta}}\right). \tag{5.18}$$

Using this definition, the transition of $\epsilon(\gamma(\mathbf{r}))$ between 1 and ϵ_∞ is centered around the van der Waals radius. Aside from R^I_{vdw}, which values are tabulated, β is left as the only adjustable parameter to fit the experimental solvation energies. The aspect of the dielectric function around an oxygen atom for different β is shown in Figure 5.5. This parameter must be large enough to ensure most of the transition occurs within a small length window, but at the same time the numerical accuracy needs to be preserved, so there is an upper bound for β, which depends on the given grid size.

Within this framework, the electrostatic contribution to $V^{KS}[\rho]$ is simply the electrostatic potential $\phi[\rho]$, and the stability of Car-Parrinello dynamics in periodic slabs is recovered. Table 5.1 presents, for several neutral and charged solutes, a comparison between the values of ΔG_{sol} obtained with the dielectric functions of equations 5.15 and 5.18, respectively. The small differences proceed exclusively from ΔG_{el} since ΔG_{cav} is the same in both cases (ΔG_{sol} = ΔG_{el} + ΔG_{cav}). As mentioned above, with a proper choice of β the position-dependent dielectric is able to provide solvation energies in close agreement with the previous model and with experiments. The results shown correspond to β = 2.4.

The gas phase energies of the charged species in Table 5.1 (required to obtain the solvation energies) were calculated considering the Makov-Payne correction [27], which takes into account how the gas phase energy of charged systems is affected by its periodic

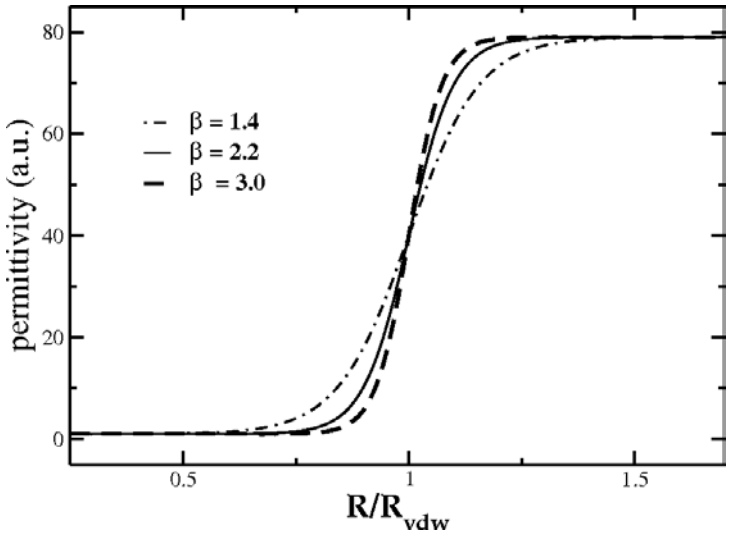

Figure 5.5. The permittivity around an oxygen atom as a function of the distance, for different values of the parameter β, according to the position-dependent dielectric defined in equations 5.17 and 5.18. The transition, centered around the van der Waals radius, becomes sharper as β is increased.

Table 5.1. Solvation free energies (kcal/mol) for selected molecules and ions in water, calculated with the solvation model based on a dielectric function $\epsilon = \epsilon(\rho)$ determined by the electron density,[a] and $\epsilon = \epsilon(\gamma(\mathbf{R_I}))$ determined by the atomic positions with β=2.4 (see text). Experimental values[b] and results from PCM[c] are also shown.

	Expt.	$\epsilon = \epsilon(\rho)$	$\epsilon = \epsilon(\gamma)$	PCM
H_2O	-6.3	-8.4	-8.8	-5.4
CH_3CONH_2	-9.7	-10.5	-8.0	-4.6
$CH_3NH_3^+$	-73	-81.0	-81.9	-65.1
NO_3^-	-65	-57.8	-60.6	-62.6
Cl^-	-75	-66.9	-68.6[d]	-72.6

[a] From reference [6]. [b] From references [23, 24]. [c] Obtained with the Polarizable Continuum Model as implemented in Gaussian 03. [15, 25] [d] The van der Waals radius for ionic chlorine was set equal to 2.059 Å, from reference [26].

images in supercell calculations,

$$E_{gas} = E_{PBC} + \frac{q^2\alpha}{2L} - \frac{2\pi qQ}{3L^3} + O[L^{-5}] \tag{5.19}$$

where E_{gas} and E_{PBC} are the isolated and the supercell energies, respectively, q is the charge of the system, Q is its quadrupole moment, L is the lattice parameter, and α is the Madelung constant. In practice, various single point calculations were performed for a given ion in cubic cells of different sizes, and the gas phase energy corresponding to an infinite cell was extrapolated using equation 5.19 to the leading order in L.

The explicit dependence of ϵ on the ionic positions involves a new contribution to the forces arising from the derivative of E_H with respect to $\mathbf{R_I}$, which must be taken into account to perform conservative molecular dynamics simulations. After some manipulation involving the use of equations 5.11 and 5.12, this derivative can be expressed as follows (the full derivation is given in the Appendix at the end of the chapter):

$$\frac{\partial E_H}{\partial \mathbf{R_I}} = -\frac{1}{8\pi}\int \frac{\partial \epsilon(\mathbf{R_I})}{\partial \mathbf{R_I}}(\nabla\phi(\mathbf{r}))^2 d\mathbf{r} + \int \phi(\mathbf{r})\frac{\partial \rho_{tot}(\mathbf{r})}{\partial \mathbf{R_I}} d\mathbf{r} \tag{5.20}$$

The computation of the first term on the right is straightforward since we know, from equations 5.17 and 5.18, the explicit dependence of ϵ on $\mathbf{R_I}$:

$$\frac{\partial \epsilon(\mathbf{R_I})}{\partial \tau_I}(\mathbf{r}) = 2\beta\left(\epsilon_\infty - 1\right)\left(\frac{\tau - \tau_0}{R}\right)\frac{e^{-(R-R^I_{vdw})}\left(\sum_I e^{-(R-R^I_{vdw})}\right)^{2\beta-1}}{\left[1+\left(\sum_I e^{-(R-R^I_{vdw})}\right)^{2\beta}\right]^2} \tag{5.21}$$

with τ a generic coordinate $x, y,$ or z, $\mathbf{R_I} = (x_0, y_0, z_0)$ and $R = |\mathbf{r} - \mathbf{R_I}|$.

On the other hand, if $\phi(\mathbf{r})$ is transformed to Fourier space so that $\phi(\mathbf{r}) = \sum_{\mathbf{G}} \tilde{\phi}(\mathbf{G})e^{i\mathbf{Gr}}$ (see next section), the second term in equation 5.20 can be evaluated as

$$\int \phi(\mathbf{r})\frac{\partial \rho_{tot}(\mathbf{r})}{\partial \mathbf{R_I}} d\mathbf{r} = -\Omega\sum_{\mathbf{G}} i\mathbf{G}\tilde{\phi}^*(\mathbf{G})\tilde{\rho}_I(\mathbf{G})e^{-i\mathbf{GR_I}} \tag{5.22}$$

with $\tilde{\rho}_I(\mathbf{G})$ the form factor of the ionic densities, $\rho_I(\mathbf{r} - \mathbf{R_I}) = \sum_G \tilde{\rho}_I(\mathbf{G})e^{-i\mathbf{Gr}}e^{-i\mathbf{GR_I}}$.

To ensure the conservation of the total energy during the molecular dynamics simulations, the contributions given in equations 5.21 and 5.22 must take the place of the derivative of the Hartree energy in the absence of the dielectric:

$$\frac{\partial E_H}{\partial \mathbf{R_I}} = -4\pi\Omega\sum_{\mathbf{G}} i\mathbf{G}\left(\frac{\tilde{\rho}^*(\mathbf{G})}{G^2}\right)\tilde{\rho}_I(\mathbf{G})e^{-i\mathbf{GR_I}}. \tag{5.23}$$

5.2.2 The multigrid scheme

In standard plane waves codes based on real space grids, the electrostatic potential $\phi(\mathbf{r})$ is obtained from the Poisson equation 5.10, which can be efficiently inverted with the use of fast Fourier transforms (FFT). Both the total charge density $\rho_{tot}(\mathbf{r})$ and $\phi(\mathbf{r})$ can be expanded in plane waves,

$$\rho_{tot}(\mathbf{r}) = \sum_{\mathbf{G}} \tilde{\rho}(\mathbf{G}) e^{i\mathbf{G}\mathbf{r}}, \qquad \phi(\mathbf{r}) = \sum_{\mathbf{G}} \tilde{\phi}(\mathbf{G}) e^{i\mathbf{G}\mathbf{r}}.$$

Replacing into the Poisson equation $\nabla^2\phi = -4\pi\rho_{tot}$, and equating coefficients:

$$\mathbf{G}^2\tilde{\phi}(\mathbf{G}) = 4\pi\tilde{\rho}(\mathbf{G}) \;\; , \quad \phi(\mathbf{r}) = \sum_{\mathbf{G}} \frac{4\pi}{\mathbf{G}^2}\tilde{\rho}(\mathbf{G}) e^{i\mathbf{G}\mathbf{r}} \tag{5.24}$$

Unfortunately, the Poisson equation in the presence of an arbitrary dielectric, equation 5.11, can not be addressed in the same way, and an alternative numerical scheme is required. To that end, we have implemented from scratch a sixth-order multigrid code, which solves in real space the Poisson equation with non-constant coefficients and periodic boundary conditions. Today, multigrid methods are possibly the most efficient, versatile, and general numerical schemes to address linear partial differential equations [28–30] In the following, we provide the essential concepts regarding linear multigrid algorithms.

Expansion of differential equations in finite differences and the Gauss-Seidel method

To make the following discussion simpler, we will consider for now the one-dimensional form of equation 5.11 with constant coefficients ($\epsilon = 1$), which reduces to the Poisson equation in the gas phase:

$$\frac{\partial^2\phi}{\partial x^2} = -4\pi\rho \tag{5.25}$$

This differential equation is written for continuous functions, but can be rewritten for discrete functions, defined by its value for each point in the grid: $\phi(x) \rightarrow \phi_i$, where i represent the grid point. In this way, equation 5.25 can be expressed using a finite differences expansion up to second order:

$$\frac{\partial^2\phi_i}{\partial i^2} = \frac{\phi_{i+1} + \phi_{i-1} - 2\phi_i}{h^2} = -4\pi\rho_i \tag{5.26}$$

where h represents the distance between two consecutive grid points. The larger this value, the lesser the accuracy of the discretization, in which case it is said that the grid is coarser. On the contrary, when the spacing is smaller, the accuracy is higher and the grid is finer

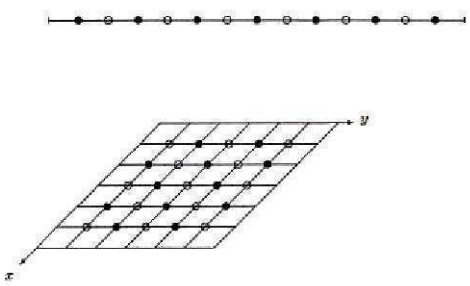

Figure 5.6. A one-dimensional grid (top) and a two-dimensional grid (bottom), showing the red points (○) and the black points (●) for red-black relaxation. Figure taken from reference [28].

(or denser).

The solution of equation 5.26 can be found numerically using an iterative procedure. This type of relaxation methods departs from an initial guess which is succesively improved along a series of updating steps: the simplest way to do this is to write ϕ_i as a function of all the other numerical components,

$$\phi_i^{j+1} \leftarrow \frac{1}{2}(\phi_{i-1}^j + \phi_{i+1}^j + h^2\rho_i) \quad , \quad 1 \leq j \leq n \tag{5.27}$$

where the arrow notation stands for replacement or overwritting, j for the iteration number, and n for the number of grid points. In the so called *Gauss-Seidel* algorithm, the components of ϕ are overwritten as soon as they are computed, so as to use updated values within the same iteration. Once all $\{\phi_i\}$ are calculated, a new iteration follows, until ϕ_i^{j+1} does not differ significantly from ϕ_i^j. In particular, the *red-black Gauss-Seidel* method updates all the even number first (equation 5.28) and then all the odd ones (equation 5.29).

$$\phi_{2i} \leftarrow \frac{1}{2}(\phi_{2i-1} + \phi_{2i+1} + h^2 f_i) \tag{5.28}$$

$$\phi_i \leftarrow \frac{1}{2}(\phi_{i-1} + \phi_{i+1} + h^2 f_{2i+1}) \tag{5.29}$$

This strategy is illustrated in Figure 5.6 for one and two dimensional systems. This method has a clear advantage in terms of parallel computing, where equations 5.29 and 5.28 might be easily distributed onto different processors.

While the Gauss-Seidel algorithm is quite robust, achieving convergence in most cases, it is at the same time extremely slow: it takes too many iterations to converge, becoming impractical for real applications. The reason behind this behavior can be understood if the

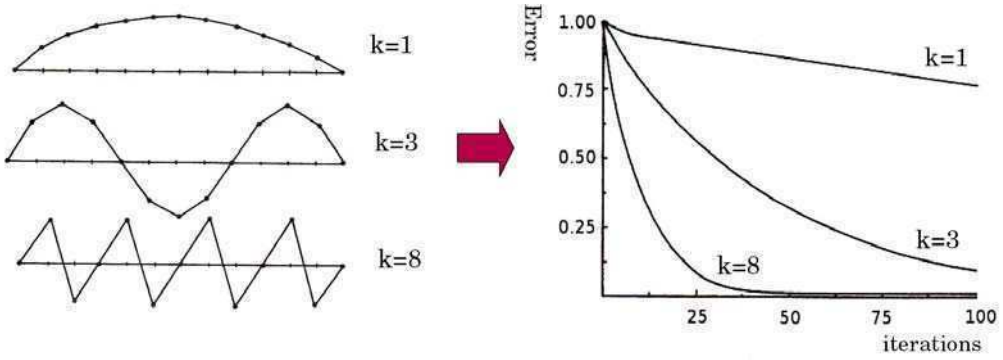

Figure 5.7. Some Fourier modes of different frequency (left) and their convergence rate (right). Data taken from reference [28].

function ϕ is expressed as a Fourier series (for simplicity let's consider only sine terms):

$$\phi_i = \sum_k c_k sin\left(\frac{2\pi k}{L}\frac{i}{n}\right) \quad , \quad 0 \leq i \leq n \quad , \quad 1 \leq k \leq n-1 \tag{5.30}$$

where i denotes a grid point, k is called the wavenumber (or frequency) of each Fourier mode, and L is the length of the domain where the function is being expanded. If each term of expansion 5.30 is analyzed separately, it turns out that the rate of convergence for each Fourier mode is strongly dependent on the wavenumber: the low frequency (or slow) modes require many more iterations than the high frequency components. Figure 5.7 illustrates this behavior.

The convenience of using a multigrid scheme

The error in the components of higher wavenumber decrease very fast, so that the cost of the relaxation scheme falls on the smooth modes. In general terms, there are two strategies to improve the relaxation technique: (1) depart from a better initial guess and (2) accelerate the convergence rate of the smooth modes. The multigrid scheme works in this last direction. The principle behind multigrid methods is depicted in Figure 5.8: representation of a given function in coarser grids increases the frequency of all modes, thus accelerating the general convergence rate.

In multigrid calculations, the Gauss-Seidel method is performed on different grid sizes. This requires to move all functions from one grid size to another. The procedure of expanding a numerical function in a finer grid is called an *interpolation* operation, while the movement to a coarser grid is a *restriction* operation. Convergence in coarser grids is faster but inaccurate (rapidly oscillating modes can not be accurately represented in coarser grids), so multigrid methods involve an alternation of relaxation steps back and forth in different grid levels. There are several multigrid schemes that can be used (Figure

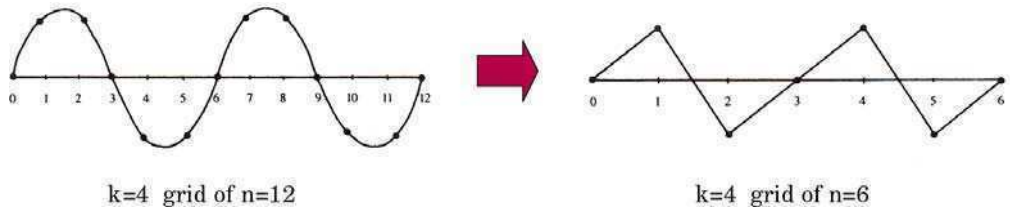

Figure 5.8. Representation of one Fourier mode in two different grids. Data taken from reference [28].

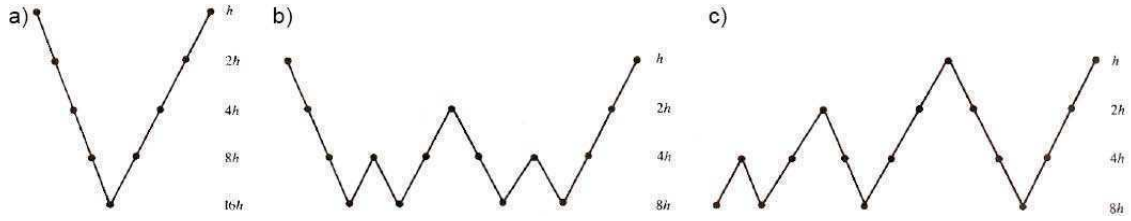

Figure 5.9. Restriction-interpolation grid schedules for a) V-cycle, b) W-cycle, and c) Full Multigrid scheme, allways on four levels. Figure taken from reference [28].

5.9). The *Full Multigrid* scheme is the one adopted in our implementation. Figure 5.9 displays multigrid schemes of up to four levels, but the number of levels can vary, depending on the system.

To understand how multigrid calculations proceed, it should be noted that equation 5.26 can be expressed in a generic matrix way:

$$\mathbf{A}.\mathbf{u} = \mathbf{f} \tag{5.31}$$

where **u** represents the exact solution and **f** is the rigth hand side, for example, in equation 5.25 **u** is the unknown function ϕ, **f** is $-4\pi\rho$, and **A** is the matrix representation of the Laplacian operator, ∇^2. **v** will be used to denote an approximation to the exact solution, which is given in the first step of the procedure as an initial guess. The *residual*, defined as $\mathbf{r} = \mathbf{f} - \mathbf{A}.\mathbf{v}$, is a measure of how well **v** approximates **u**. The error of this approximation is simply $\mathbf{e} = \mathbf{u} - \mathbf{v}$. Naturally, the error **e** is just as inaccessible as the exact solution itself.

By construction $\mathbf{e} = 0$ if $\mathbf{r} = 0$. However, a small norm of **r** does not guarantee a small norm of **e**. A *residual equation* can be obtained if 5.31 is rewritten in terms of **r** and **e**:

$$\mathbf{A}.\mathbf{e} = \mathbf{r} \tag{5.32}$$

In multigrid methods, equation 5.32 is relaxed employing the Gauss-Seidel scheme in the coarser grid to get an approximation to **e** from **r**. The error function is then interpolated to the next (finer) grid, where a new approximation to **v** is computed according to the

definition of the error:

$$\mathbf{v} = \mathbf{v} + \mathbf{e} \tag{5.33}$$

This idea of improving the approximation **v** is known as *residual correction*. A new series of Gauss-Seidel relaxation steps are performed at this level, and the procedure continues to complete a V-cycle (or wathever schedule is being used).

Multigrid implementation for the continuum solvent method

Eq. 5.11 can be rewritten as:

$$\frac{\partial\epsilon}{\partial x}\frac{\partial\phi}{\partial x} + \frac{\partial\epsilon}{\partial y}\frac{\partial\phi}{\partial y} + \frac{\partial\epsilon}{\partial z}\frac{\partial\phi}{\partial z} + \epsilon\left(\frac{\partial^2\epsilon}{\partial x^2} + \frac{\partial^2\epsilon}{\partial y^2} + \frac{\partial^2\epsilon}{\partial z^2}\right) = -4\pi\rho. \tag{5.34}$$

We developed equation 5.34 in finite differences, expanding the derivatives of ϕ and ϵ to sixth-order according to the following relations for the gradient and the Laplacian:

$$\frac{\partial f(\mathbf{r})}{\partial\tau} = \frac{1}{h}\sum_{n=-3}^{3}\alpha_n\, u_{i+n} + O(h^7) \tag{5.35}$$

$$\frac{\partial^2 f(\mathbf{r})}{\partial\tau^2} = \frac{1}{h^2}\sum_{n=-3}^{3}\beta_n\, u_{i+n} + O(h^7) \tag{5.36}$$

where τ is a generic coordinate $x, y,$ or z; h is the grid spacing in the direction τ; and u is the discretization of a continuous function $f(\mathbf{r})$, representing $\phi(\mathbf{r})$, $\rho(\mathbf{r})$, or $\epsilon(\mathbf{r})$. u_i refers to u evaluated at a mesh point associated with **r**, while u_{i+n} corresponds to a neighboring point n positions to the right in the direction τ (if $n < 0, u_{i+n}$ is located to the left of u_i) [5].

In the case of $\epsilon(\mathbf{r}) = 1$ for all **r**, this method provides a solution for $\phi(\mathbf{r})$ which is indistinguishable from the one obtained with FFT. It also demonstrated an excellent performance when tried on functions with non-constant coefficients and oscillation frequencies comparable to those of interest. For example, for $\phi = e^{-ar}$ and $\epsilon = e^{-br}$ $(0.5 < a, b < 2.0)$ the relative error in $\phi(\mathbf{r})$ was less than 10^{-4} in a mesh of 80×80×80 points.

At the initial steps of a molecular dynamics simulation, the convergence of the potential may require 15-30 multigrid cycles. Given the self-consistent nature of the procedure, however, after a few time steps the number of cycles necessary to reach convergence is typically decreased to less than five. Even so, the multigrid algorithm is still significantly more expensive than FFTs. Propitiously, multigrid methods can be adapted to any kind of boundary conditions, and this feature can be exploited to reduce the size of the mesh involved. To implement this idea, a region in the supercell—preferably the slab—must

[5] The coefficients α_n and β_n are given by: $\alpha_0 = 0,\ \alpha_1 = \frac{3}{4},\ \alpha_2 = -\frac{3}{20},\ \alpha_3 = \frac{1}{60},\ \alpha_{-n} = -\alpha_n, \beta_0 = -\frac{49}{18},\ \beta_1 = \frac{27}{18},\ \beta_2 = -\frac{27}{180},\ \beta_3 = \frac{2}{180},\ \beta_{-n} = \beta_n$.

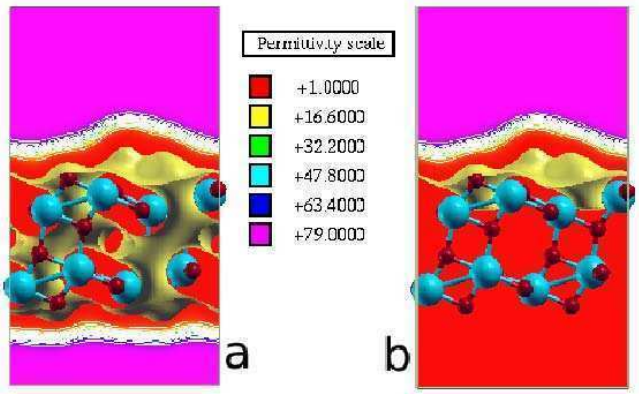

Figure 5.10. Contour plot of the dielectric function $\epsilon(\mathbf{r})$ in a supercell containing a four layers slab representing the anatase (101) face of TiO_2. An isosurface corresponding to $\epsilon(\mathbf{r})$=1.4 is displayed in yellow. In (a) the solvent percolates through the surface, whereas in (b) it is excluded from the slab by virtue of the artifact given in relation (19).

remain inaccessible to the solvent, so that $\epsilon(\mathbf{r}) = 1$ within it. In practice, the dielectric function of equations 5.15 or 5.18 is not diffuse enough as to encompass all the volume of the slab—if it were, the solvation effect would fade at the molecular boundaries—, so the solvent occupies the interstitial space left by the atomic structure (Figure 5.10a). This is inconvenient not only because it increases the numerical complexity of the problem, but also because it is not physical, i.e., the solvent does not penetrate the atomic structure of the surface. A simple device to exclude the solvent from the solid interspaces is to modify $\gamma(\mathbf{r})$ in the following way:

$$\gamma(\mathbf{r}) = \begin{cases} \sum_I e^{-\left(|\mathbf{r}-\mathbf{R_I}|-R^I_{vdw}\right)} & z_I > z_{lim} \\ \sum_I e^{-\frac{z-z_I}{|z-z_I|}\left(|\mathbf{r}-\mathbf{R_I}|-R^I_{vdw}\right)} & z_I \leq z_{lim} \end{cases} \tag{5.37}$$

where z_I is the z-component of $\mathbf{R_I}$ (we recall z is the coordinate perpendicular to the surface; it is zero at the bottom of the unit cell and maximum at the top). The factor $\frac{z-z_I}{|z-z_I|}$ produces a rapid increase in $\gamma(\mathbf{r})$ underneath the atom I, which saturates the value of $\epsilon(\mathbf{r})$ for all atoms I located below z_{lim}. Thus, only the upper face of the slab is in contact with the solution, the dielectric function becoming equal to 1 throughout the lower section of the supercell. Figure 5.10b depicts $\epsilon(\mathbf{r})$ when z_{lim} is chosen equal to the z coordinate of an ion belonging to the second layer.

5.3 Performance of the continuum solvent method

The performance of the method, i.e., its capability to recreate chemistry in solution, is going to be examined in the next subsections through the study of charge polarization and

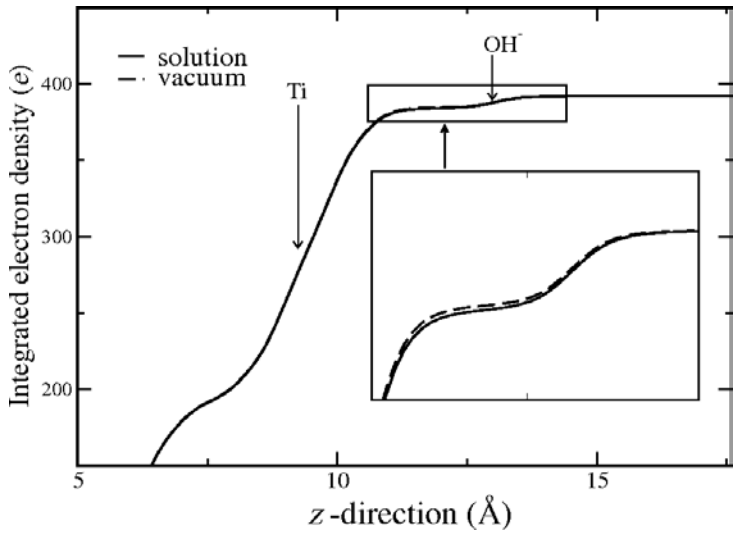

Figure 5.11. Electron density integrated on the xy plane, and displayed as a function of the z coordinate, for the hydroxyl anion situated 4 Å above the surface. The approximate positions of the upper Ti layer and of the OH^- ion are indicated with arrows. Enlargement of the interfacial region shows a depletion of the electron density in solution with respect to vacuum: there is an average charge difference of about 0.5 e between the two curves, originating in the stabilization of the negative charge of the hydroxyl surrounded by the dielectric. Both curves coincide beyond the position of the OH^- anion.

molecular dynamics at the TiO_2 solid-liquid interface.

5.3.1 Electron density distribution for OH^- anion

Replacement of explicit solvation by a dielectric continuum medium neglects the structural features of the solvation shell, but retains the basic polarization effect. This is manifested in the charge of the hydroxyl group: if an extra electron is added to a neutral system consisting of an anatase (101) slab plus a distant OH moiety situated 4 Å away from the surface in the gas phase, about one half (0.5 e) of the additional negative charge flows to the surface and the other half to the OH group. Noticeably, in the presence of the dielectric medium, the excess electron spontaneously localizes on the hydroxyl, as expected in solution. This result indicates that the polarization effect of the medium is able to stabilize isolated charges in solution, which are unstable in the gas phase. In Figure 5.11 the integrated total electron density along the z direction is plotted in vacuum and in the continuum solvent: differences between both curves are due to the charge redistribution induced by the medium.

5.3.2 Molecular Dynamics at the TiO_2 interface

It is well known that surface groups of most inorganic oxides ionize in solution, exhibiting the following equilibria:

$$\text{M-O}^z + \text{H}_3\text{O}^+ \Leftrightarrow \text{M-OH}^{z+1} + \text{H}_2\text{O} \Leftrightarrow \text{M-OH}_2^{z+2} + \text{HO}^-$$

with z the surface group charge, which can be negative, positive, or zero, depending on the nature of the oxide [31]. Understanding the acid-base behavior resulting from these equilibria is crucial in almost every application of these materials in solution. Isoelectric points of many oxides have been known for years [32], however, it is very difficult to probe the surface of bulk materials or nanoparticles in solution, and most of the data collected corresponds to the average behavior of the different surfaces exposed in a given experiment. More recently, researchers have sought to take advantage of density functional theory to establish the degree of dissociation and protonation at different titania-water interfaces with an explicit representation of the solvent [33–36]. For the reasons already discussed, such an approach is costly and has been employed only in a limited number of cases. In what follows, we apply our continuum solvent model to characterize the hydrated (101) surface of the anatase structure of TiO_2, which is possibly the most stable and abundant [37]. The adsorption of H_2O on perfect TiO_2 surfaces in the gas phase has been thoroughly investigated using both experimental and theoretical approaches [38–43]. In the case of the (101) face of anatase, there is consensus in the fact that molecular adsorption of water is thermodynamically the most stable. Electronic structure calculations suggest that the difference between the two possible adsorption modes—molecular versus dissociated—is of nearly 10 kcal/mol [41]. We have performed calculations in four layers slabs representing the (101) surface of the anatase structure. As previously reported, our own calculations in vacuum summarized in Table 5.2 show that at different water coverages, the molecular pathway is the most favored. The adsorption energies from the liquid phase, given in the same Table, indicate that molecular adsorption prevails also in the presence of the continuum solvent. It should be noted, though, that because of the dielectric embedding, the binding energy of H_2O can not be computed in a straightforward manner as in the gas phase: the values informed in Table 5.2 are energy differences between the explicit and implicit hydration of the interface. In other words, the slightly negative number (-3.0 kcal/mol) corresponding to molecular adsorption is just the difference between the interaction of the surface with a water monolayer and with the implicit solvent, and must not be misinterpreted in the sense that TiO_2 affinity for water is weakened in solution. Such a small energy is indeed a quite remarkable result, because it states that the continuum model retains the magnitude of the explicit water-oxide interaction. Moreover, the stabilization of up to 3 kcal/mol with respect to implicit hydration could be in part

Table 5.2. Adsorption energies for water on the anatase (101) surface in the gas phase and in solution, in both the molecular and dissociative configurations at different coverages. Note that data in solution represent the energetic cost of exchanging implicit for explicit water. Values are given in kcal per H_2O molecule.

	Molecular		Dissociative	
	$\theta = 0.25$	$\theta = 1$	$\theta = 0.25$	$\theta = 1$
Gas phase	-19.4	-17.8	-10.3	-7.4
Solution	-	-3.0	-	6.6

ascribed to the hydrogen bonding network arising within the monolayer, not accounted for in the continuum model. In the same way, the positive energy reported for dissociative adsorption does not imply that dissociation in solution is not exothermic, but it is just less exothermic than molecular hydration. The main result driven from these data is that the energy difference between the two kinds of adsorption mechanisms, of 9.6 kcal/mol, remains about the same as in the gas phase. In solution, however, dissociation is likely to occur, controlled by the pH of the medium (see below).

The quantitative effect of pH on the ionization of the surface is quite difficult to assess from first principles simulations, since a huge supercell would be needed to have a meaningful representation of the proton concentration in the system. In this preliminary study, we limit ourselves to examine the proton exchange between an adsorbed water molecule and a hydroxyl anion from the solution, using molecular dynamics at 300 K. This computational experiment is meant to provide a qualitative picture of the abstraction of a proton from the surface in the presence of OH^-, illustrating at the same time the performance of the continuum solvent method. Solvation of hydrophilic surfaces often give rise to structured contact layers in which the dielectric constant and other properties can significantly differ from those of bulk water, rendering unreliable the use of an implicit solvent model. In such cases, explicit consideration of a few water molecules belonging to the first solvation layers could be important. Recent molecular dynamics simulations at the TiO_2-water interface using classical potentials have shown that the properties of the interface converge very rapidly to those of the bulk phase beyond the second adsorbed layer [44, 45]. In light of this, we include in our system eight water molecules making up the first two solvation layers, which should be enough to retrieve a qualitatively correct representation of the interface within the scope of the present analysis. The inset of Figure 5.12 shows the initial and final structures corresponding to two molecular dynamics simulations, one in vacuum and the other in solution, started from the same geometry and with identical computational parameters. In the initial configuration an OH^- group exhibits an H-bond with a water molecule of the second hydration layer. Figure 5.12 presents the intramolec-

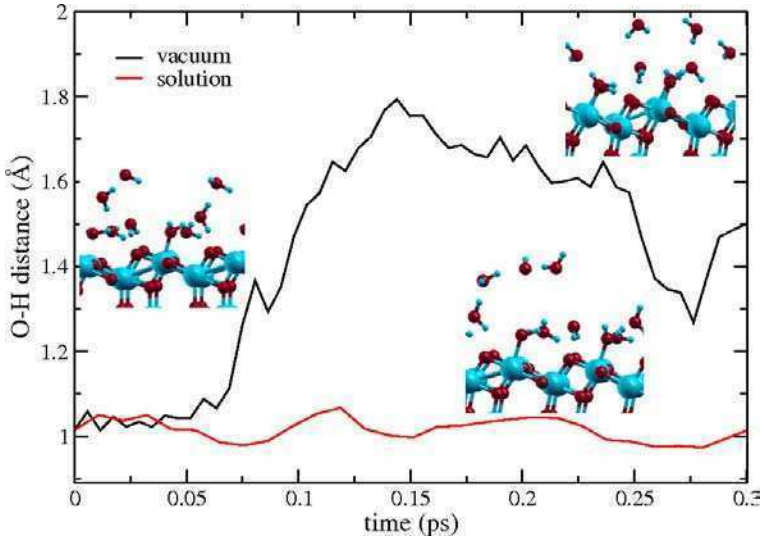

Figure 5.12. Interatomic O_a-H_a distance during molecular dynamics simulations of a water bilayer adsorbed on titania and in contact with an OH^- ion, in vacuum and in a continuum solvent. O_a and H_a are atoms of a water molecule H-bonded to the OH^- group at the beginning of the simulation. Proton transfer is seen in vacuum but not in solution. The starting geometry is shown on the left, while the upper and lower figures on the right depict the atomic structures in vacuum and in solution for the final time steps.

ular O_a-H_a distance, where H_a is the proton involved in the H-bond with the hydroxide. Early in the gas phase simulation, the covalent O_a-H_a bond in H_2O is disrupted and the H_a atom is transferred to the neighboring OH^- group, triggering a Grotthuss like exchange of protons to leave an hydroxyl function on the surface. This is not at all surprising, but is just reflecting the fact that a negative charge would rather localize on the oxide surface than on an hydroxide ion exposed to the gas phase. In the continuum solvent, this trend is reverted. The negatively charged hydroxide is stabilized in the polar environment and remains as part of the hydrogen-bonding network.

Had the simulation been started from a random configuration in the presence of the implicit solvent, the OH^- anion might have explored the supercell for several picoseconds without ever reacting with the water molecules of the contact layers. In the absence of the solvent, instead, the unscreened interaction between the hydroxide and the H_2O molecules leads to an immediate reaction, and the final result is the hydroxylation of the TiO_2 surface, as already commented. This distinctive behavior is displayed in Figure 5.13, which presents the O_b-H_a distances for two simulations in vacuum and in solution, departing from the same configuration, with O_b the oxygen atom of the hydroxide, and H_a the atom abstracted from the hydration layer in vacuum.

The observed contrast between the two dynamics evinces how the dielectric medium stabilizes the hydroxide in the liquid phase. Interestingly enough, dissociation of an ad-

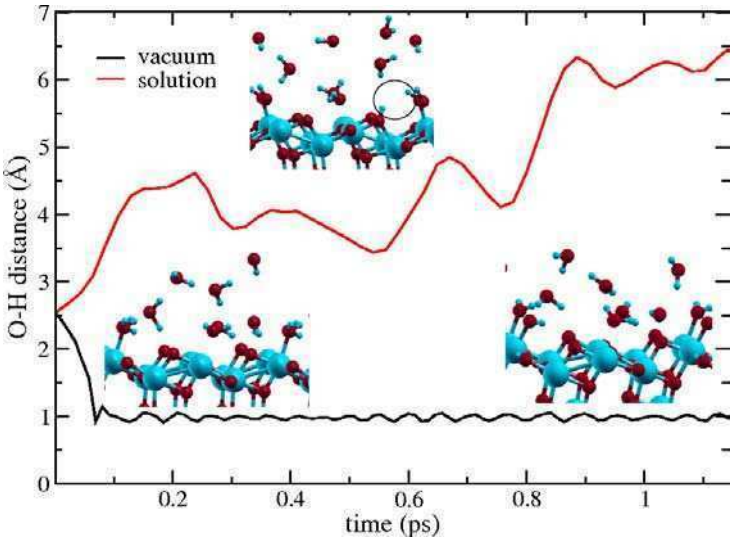

Figure 5.13. Interatomic distance O_b-H_a during the molecular dynamics simulations of a water bilayer adsorbed on titania in the presence of an hydroxide ion initially situated 2.5 Å away from the closest water molecule. O_b is the oxygen atom of the hydroxide and H_a is one of the nearest H_2O protons, which is rapidly exchanged during the gas phase dynamics. In solution, instead, the interaction between the OH^- ion and the interface is efficiently screened. The starting geometry is shown on the left, while the figures on the center and on the right depict the atomic structures after 1 ps of dynamics in vacuum and in solution, respectively. A spontaneously dissociated water, enclosed in a black trace, is observed in the continuum solvent.

sorbed water molecule takes place during the simulation in the implicit solvent (see inset, Figure 5.13). Spontaneous dissociation of water has never been observed in simulations of the stoichiometric (101) anatase surface with up to three hydration monolayers [1, 2, 34], suggesting that the continuum solvent may play a significant role even when several water layers are considered.

5.4 Closing remarks

We have shown that a dielectric medium defined as a function of the self-consistent charge density provokes a strong response in the effective potential, which in solid-liquid systems may spoil the convergence of the Car-Parrinello electronic dynamics. Such a response can be avoided with a dielectric based on a non self-consistent charge, preserving in this way the potential and allowing for conservative molecular dynamics simulations. This approach is equivalent to have a position-dependent permittivity, and therefore a new term in the ionic forces must be considered.

The methodology presented here is a powerful instrument to explore the thermodynamics and the reactivity of surfaces and nanoparticles in solution. Replacement of the solvent

molecules by a dielectric continuum may neglect the structural features of the liquid phase, but it does capture the essential polarization effect of the medium. This is apparent in the localization of entire negative charge on the solvated hydroxyl group. In the gas phase, instead, the additional charge splits between the OH^- and the slab.

A compelling application for this continuum solvent scheme, as well as a natural continuation of this work, would be the characterization of the adsorption energies and geometries of water and other species on the different surfaces of titanium dioxide. We deem especially worthwhile the calculation of the reaction energies for the kind of equilibria mentioned above, e.g., Ti-OH_2 + OH^- $\Leftrightarrow$ Ti-OH^- + H_2O, as a function of the surface structure. In particular, the adsorption of small molecules at the solid-liquid interface of titanium dioxide, is studied in the next chapter of this thesis.

At this point it should be noted that it would not be feasible to have an estimate of reaction energies involving charged species without the solvation model: in the absence of the dielectric, the interaction between the surface and the OH^- ion (or between the charged slab and the water molecule) is extremely dependent on the distance separating them, and therefore it is not possible to establish unequivocally the energies for reactants and products. When the dielectric is included, the long range interaction between charged and polar fragments is efficiently screened, and the total energy of the system becomes independent of the position of the molecule (or the ion) with respect to the slab. This property makes it possible to evaluate reaction energies on periodic surfaces in solution which could not be calculated by other means, except perhaps with extensive molecular dynamics simulations.

5.5 Future challenges

Two ample research horizons are envisioned following this work: (i) the assessment of the role of the solvent in a great diversity of problems in surface chemistry; (ii) the improvement and further development of the continuum solvent implemementation itself.

Along the first line, the influence of the solvent on structure, on surface polarization and equilibria, on vibrational frequencies, or on charge transfer phenomena, are all problems of the greatest relevance where the present approach can make a significant contribution. The use of this kind of methodology in combination with weighted importance sampling techniques (e.g., Umbrella sampling) [46] could provide estimates for the acid-base equilibrium constants corresponding to different oxide surfaces and phases. The Umbrella sampling technique has been already implemented in the Car-Parrinello approach within the Quantum Espresso package and used in this thesis to account for the activation energies of dissociative processes upon anatase (101) and rutile (110) in vacuum [47], as

explained in chapter 3.

Concering the second line of research, computational programming is still needed to improve the efficiency of the multigrid algorithm. Parallelization of the entire algorithm is in due course. A parallel implementation of the model would expand the sizes and time windows that can be explored with this method.

Ionic strenght effects can be considered through the linearized Poisson-Boltzmann equation [48]:

$$\nabla \cdot (\epsilon[\gamma(\mathbf{r})]\nabla\phi(\mathbf{r})) = -4\pi\rho_{tot}(\mathbf{r}) + \epsilon k^2\phi(\mathbf{r}) \tag{5.38}$$

where the additional term $\epsilon k^2\phi(\mathbf{r})$ represents the effect of the ionic atmosphere. $k^2 = \frac{8\pi e^2 I}{\epsilon k_B T}$, is the inverse of the Debye length square[6] and I represents the ionic strength of the solution. [7] The linearized Poisson-Boltzmann equation can be applied to describe systems of low salt concentrations, typically below 0.01 M for a monovalent ionic compound such as NaCl.

5.6 Appendix: derivative of E_H with respect to the ionic positions

In the absence of a dielectric ($\epsilon = 1$), equation 5.24 can be inserted in the expression for the Hartree energy to give

$$E_H = 2\pi\Omega \sum_{\mathbf{G}} \frac{|\tilde{\rho}(\mathbf{G})|^2}{G^2} \tag{5.39}$$

where $\tilde{\rho}(\mathbf{G})$ are the Fourier coefficients for the expansion of $\rho_{tot}(\mathbf{r})$, $\tilde{\rho}(\mathbf{G}) = \tilde{\rho}_e(\mathbf{G}) + \sum_I \tilde{\rho}_I(\mathbf{G})e^{-i\mathbf{G}\mathbf{R_I}}$. Since the only explicit dependence of $\tilde{\rho}(\mathbf{G})$ on $\{\mathbf{R_I}\}$ is through the structure factor ($e^{-i\mathbf{G}\mathbf{R_I}}$), the derivative of equation 5.39 with respect to the atomic positions is just

$$\frac{\partial E_H}{\partial \mathbf{R_I}} = -4\pi\Omega \sum_{\mathbf{G}} i\mathbf{G} \left(\frac{\tilde{\rho}^*(\mathbf{G})}{G^2}\right) \tilde{\rho}_I(\mathbf{G})e^{-i\mathbf{G}\mathbf{R_I}}. \tag{5.40}$$

In the presence of a dielectric medium determined by the ionic coordinates, equation 5.39 does not hold. To calculate $\partial E_H/\partial \mathbf{R_I}$ we replace $\epsilon[\rho]$ for $\epsilon(\mathbf{R_I})$ in equation 5.11 and derivate:

$$\frac{\partial E_H}{\partial \mathbf{R_I}} = \frac{1}{8\pi}\int \frac{\partial\epsilon(\mathbf{R_I})}{\partial \mathbf{R_I}}(\nabla\phi(\mathbf{r}))^2 d\mathbf{r} + \frac{1}{8\pi}\int \epsilon(\mathbf{R_I})\frac{\partial(\nabla\phi(\mathbf{r}))^2}{\partial \mathbf{R_I}} d\mathbf{r}. \tag{5.41}$$

[6] The Debye length is the scale over which mobile charge carriers, in this case electrolytes, screen out electric fields.

[7] $I = \frac{1}{2}\sum_{i=1}^{n} C_i Z_i^2$ is the ionic strenght of the solution and is a function of the molar concentration (C_i) of the ionic ions of charge Z_i.

The second term on the right member can be further developed as follows:

$$\frac{1}{8\pi}\int \epsilon(\mathbf{R_I})\frac{\partial(\nabla\phi(\mathbf{r}))^2}{\partial\mathbf{R_I}}d\mathbf{r} = \frac{2}{8\pi}\int \epsilon(\mathbf{R_I})\nabla\phi(\mathbf{r})\left(\nabla\frac{\partial\phi(\mathbf{r})}{\partial\mathbf{R_I}}\right)d\mathbf{r} =$$

$$-\frac{1}{4\pi}\int \nabla\cdot[\epsilon(\mathbf{R_I})\nabla\phi(\mathbf{r})]\frac{\partial\phi(\mathbf{r})}{\partial\mathbf{R_I}}d\mathbf{r} = \int \rho_{tot}(\mathbf{r})\frac{\partial\phi(\mathbf{r})}{\partial\mathbf{R_I}}d\mathbf{r} \tag{5.42}$$

where we have integrated by parts and used equation 5.11. Then, it is possible to rewrite equation 5.41:

$$\frac{\partial E_H}{\partial\mathbf{R_I}} = \frac{1}{8\pi}\int \frac{\partial\epsilon(\mathbf{R_I})}{\partial\mathbf{R_I}}(\nabla\phi(\mathbf{r}))^2 d\mathbf{r} + \int \rho_{tot}(\mathbf{r})\frac{\partial\phi(\mathbf{r})}{\partial\mathbf{R_I}}d\mathbf{r}. \tag{5.43}$$

On the other hand, the derivation of the general expression for the Hartree energy leads to:

$$\frac{\partial E_H}{\partial\mathbf{R_I}} = \frac{1}{2}\int \rho_{tot}(\mathbf{r})\frac{\partial\phi(\mathbf{r})}{\partial\mathbf{R_I}}d\mathbf{r} + \frac{1}{2}\int \phi(\mathbf{r})\frac{\partial\rho_{tot}(\mathbf{r})}{\partial\mathbf{R_I}}d\mathbf{r}. \tag{5.44}$$

Equating 5.43 and 5.44 we find the following relation:

$$\int \rho_{tot}(\mathbf{r})\frac{\partial\phi(\mathbf{r})}{\partial\mathbf{R_I}}d\mathbf{r} = -\frac{1}{4\pi}\int \frac{\partial\epsilon(\mathbf{R_I})}{\partial\mathbf{R_I}}(\nabla\phi(\mathbf{r}))^2 d\mathbf{r} + \int \phi(\mathbf{r})\frac{\partial\rho_{tot}(\mathbf{r})}{\partial\mathbf{R_I}}d\mathbf{r}. \tag{5.45}$$

Ultimately, replacing eq. 5.45 into eq. 5.43 we obtain the final result,

$$\frac{\partial E_H}{\partial\mathbf{R_I}} = -\frac{1}{8\pi}\int \frac{\partial\epsilon(\mathbf{R_I})}{\partial\mathbf{R_I}}(\nabla\phi(\mathbf{r}))^2 d\mathbf{r} + \int \phi(\mathbf{r})\frac{\partial\rho_{tot}(\mathbf{r})}{\partial\mathbf{R_I}}d\mathbf{r}. \tag{5.46}$$

References

[1] A. Tilocca and A. Selloni, *Langmuir* 20, (2004), 8379.

[2] A. B. Mukhopadhyay, C. B. Musgrave, and J. F. Sanz, *J. Am. Chem. Soc.* 130, (2008), 11996.

[3] F. D. Angelis, A. Sgamellotti, M. Cossi, N. Rega, and V. Barone, *Chem. Phys. Lett.* 328, (2000), 302.

[4] J.-L. Fattebert and F. Gygi, *Int. J. Quantum Chem.* 93, (2003), 139.

[5] H. M. Senn, P. M. Margi, R. Schmid, T. Ziegler, and P. Blöchl, *J. Chem. Phys.* 118, (2003), 1089.

[6] D. A. Scherlis, J.-L. Fattebert, F. Gygi, M. Cococcioni, and N. Marzari, *J. Chem. Phys.* 124, (2006), 074103.

[7] S. A. Petrosyan, A. A. Rigos, and T. A. Arias, *J. Phys. Chem. B* 109, (2005), 15436.

[8] S. A. Petrosyan, J.-F. Briere, D. Roundy, and T. A. Arias, *Phys. Rev. B* 75, (2007), 205105.

[9] H.-F. Wang and Z.-P. Liu, *J. Phys. Chem. C* 113, (2009), 17502–17508.

[10] J. M. Soler, E. Artacho, J. D. Gale, A. Garcia, J. Junquera, P. Ordejon, and D. Sanchez-Portal, *J. Phys.: Condens. Matter* 14, (2002), 2745.

[11] Y.-F. Li, Z.-P. Liu, L. Liu, and W. Gao, *J. Am. Chem. Soc.* 132, (2010), 13008–13015.

[12] V. M. Sánchez, M. Sued, and D. A. Scherlis, *J. Chem. Phys.* 131, (2009), 174108.

[13] A. Ben-Naim, *Solvation Thermodynamics*, Plenum (**1987**).

[14] J. Tomasi and M. Persico, *Chem. Rev.* 94, (1994), 2027.

[15] J. Tomasi, B. Mennucci, and R. Cammi, *Chem. Rev.* 105, (2005), 2999.

[16] J. Langlet, P. Claverie, J. Caillet, and A. Pullman, *J. Phys. Chem.* 92, (1988), 1617 1988, 92, 1617.

[17] R. A. Pierotti, *Chem. Rev.* 76, (1976), 717.

[18] H.H.Uhlig, *J. Phys. Chem.* 41, (1937), 125.

[19] R. C. Tolman, *J. Chem. Phys.* 17, (1949), 333.

[20] M. Cococcioni, F. Mauri, G. Ceder, and N. Marzari, *Phys. Rev. Lett.* 94, (2005), 145501.

[21] J.-L. Fattebert and F. Gygi, *J. Comput. Chem.* 23, (2002), 662.

[22] R. G. Parr and W. Yang, *Density-Functional Theory of atoms and molecules*, Oxford University Press (**1989**).

[23] C. J. Cramer and D. G. Truhlar, *J. Am. chem. Soc.* 113, (1991), 8305.

[24] G. D. Hawkins, C. J. Cramer, and D. G. Truhlar, *J. Phys. Chem. B* 102, (1998), 3257.

[25] M. Cossi, V. Barone, R. Cammi, and J. Tomasi, *Chem. Phys. Lett* 255, (1996), 327.

[26] J. K. Badenhoop and F. Weinhold, *J. Chem. Phys* 107, (1997), 5422.

[27] G. Makov and M. C. Payne, *Phys. Rev. B* 51, (1995), 4014.

[28] W. L. Briggs, V. E. Henson, and S. F. McCornick, *A Multigrid Tutorial*, Siam (**2000**).

[29] W. H. Press, S. A. Teukolsly, W. T. Vetterling, and B. P. Flannery, *Numerical Recipes in Fortran- The Art of Scientific Computing*, Cambridge University Press (**1192**).

[30] U. Trottenberg, C. Oosterlee, and A. Schüller, *Multigrid*, Elsevier Academic Press (**2007**).

[31] J.-P. Jolivet, *Metal Oxide Chemistry and Synthesis*, John Wiley & Sons (**2000**).

[32] G. A. Parks, *Chem. Rev.* 65, (1965), 177.

[33] A. V. Bandura, D. G. Sykes, V. Shapovalov, T. N. Troung, J. D. Kubicki, and R. A. Evarestov, *Langmuir* 108, (2004), 7844.

[34] A. Tilocca and A. Selloni, *J. Phys. Chem. B* 108, (2004), 4743.

[35] M. L. Machesky, M. Pedota, D. J. Wesolowski, L. Vlcek, P. T. Cummings, J. Rosenqvist, M. K. Ridley, J. D. Kubicki, A. V. Bandura, N. Kumar, and J. O. Sofo, *Langmuir* 24, (2008), 12331.

[36] J. Cheng and M. Sprik, *J. Chem. Theory Comput.* 6, (2010), 880–889.

[37] U. Diebold, *Surf. Sci. Rep.* 48, (2003), 53–229.

[38] M. A. Henderson, *Surf. Sci.* 355, (1996), 151.

[39] R. Schaub, P. Thostrup, N. Lopez, E. Lægsgaard, I. Stensgaard, J. K. Nørskov, and F. Besenbacher, *Phys. Rev. Lett.* 87, (2001), 266104.

[40] G. Li, L. Li, J. Boerio-Goates, and B. F. Woodfield, *J. Am. Chem. Soc.* 127, (2005), 8659.

[41] A. Vittadini, A. Selloni, F. Rotzinger, and M. Grätzel, *Phys. Rev. Lett.* 81, (1998), 2954.

[42] A. Tilocca and A. Selloni, *J. Chem. Phys.* 119, (2003), 7445.

[43] P. J. D. Lindan and C. Zhang, *Phys. Rev. B* 72, (2005), 075439.

[44] M. Předota, A. V. Bandura, P. T. Cummings, J. D. Kubicki, D. J. Wesolowski, A. A. Chialvo, and M. L. Machesky, *J. Phys. Chem. B* 108, (2004), 12049.

[45] A. Kornherr, D. Vogtenhuber, M. Ruckenbauer, R. Podloucky, and G. Zifferer, *J. Chem. Phys.* 121, (2004), 3722.

[46] J. P. Torrie, G.and Valleau, *J. Comput. Phys.* 23, (1977), 187.

[47] V. M. Sánchez, J. A. Cojuloun, and D. A. Scherlis, *J. Phys. Chem. C* 114, (2010), 11522–11526.

[48] M. Friedrichs, R. Zhou, S. R. Edinger, and R. A. Friesner, *J. Phys. Chem. B* 103, (1999), 3057–3061.

Chapter 6

Adsorption of R-OH molecules on TiO_2 surfaces at the solid-liquid interface

The basic surface processes of molecules in solution (as adsorption and dissociation) are not easy to probe experimentally with microscopic resolution. Consistently, available thermodynamic and structural information is significantly less than for the gas phase, even though the solid-liquid environment is the most relevant for many applications. As has been discussed in previous chapters, limitations arise also at the simulation level. Along this chapter, we apply the methodology developed in this thesis to treat chemical processes of simple molecules at the solid-liquid boundary. In this first application of the current methodology, we start by a systematic investigation of the structural and thermodynamical features characterizing the interaction of polar molecules in solution with the most stable TiO_2 surfaces, anatase (101) and rutile(110). In particular, we have selected four hydrophilic compounds, which together are representative of the family of R-OH small adsorbates: water, hydrogen peroxide, methanol and formic acid.

6.1 Introduction

A large amount of computational research based on density functional theory (DFT) has been conducted on periodic slabs of TiO_2 in the gas phase. On anatase (101), Selloni and co-authors have shown that water adsorbs molecularly either for 1 monolayer (ML), 2 ML or 3 ML in vacuum [1–3]. There is now a general agreement about the fact that water adsorbs molecularly on anatase (101), either from the theory as well as from experiments, as it was indicated by Temperature Programmed Desorption (TPD) data [4] and confirmed by XPS results [5]. In the previous chapter, we have shown that water adsorbs molecularly at the anatase(101)-water interface. We will go back to this result with more detail along this chapter. In the case of methanol, several adsorption configurations were also investigated, for which it was found, at less than 1 ML coverage, that the molecular state is the most favored, exhibiting a dissociated stable state about 6 kcal/mol above [6].

Mattioli et al. [7] examined the interaction of the H_2O_2 molecule on the anatase surface in the presence of a water bilayer, finding that it adsorbs molecularly on the anatase surface. Vittadini et al [8] studied the formic acid adsorption energies for several geometry configurations, including molecular and dissociative processes. Their calculations showed that a monodentate molecular adsorption was the most stable.

Regarding first principles calculation of water on rutile (110), a discussion arouse in the literature concerning the type of adsorption in vacuum [9–13]. Harris et al. [9] pointed out that the energetics of dissociative and molecular adsorption are comparable, so much so that the DFT predicted adsorption mode depends on the number of layers used to model the rutile (110) surface. For a sufficiently deep slab and coverages below 1 ML, it was concluded that the molecular state is more stable than the dissociated state. At higher surface coverages, the same calculations suggest the preeminence of either a mixed state (molecular and dissociated) or a molecular state, depending on the quantity of TiO_2 layers [9], separated in all cases by slight energy differences. Our own recent free-energy calculations have shown that both states of water would be likely to coexist on the surface at 300 K [14] (see Chapter 3). Water coverages of 2 ML and 3ML have been studied by Zhang et al. [15], who showed that increasing water layers favor molecular adsorption. Calculations by Kowalski and co-workers [16] suggested that water adsorbs molecularly in ambient conditions, in agreement with Zhang et al. [15] investigation. Experimental data as TPD spectra exhibited four different peaks [17–20]. The lowest three were ascribed to molecularly adsorbed H_2O in the first monolayers, whereas the highest temperature peak was assigned to dissociated water on bridging oxygen vacancies [13]. Overall, experiments and simulations support the idea of coexistence of the molecular and dissociative modes for water on rutile (110), the presence of multilayers further stabilizing the former with respect to the later.

Static DFT calculations have been employed as well to study adsorption of a few small molecules as methanol [10,21,22] and hydrogen peroxide [10,13] on rutile (110). In both cases, the molecular and dissociative states have exhibited similar adsorption energies: depending on the authors, either the dissociated or the molecular state of methanol was identified as the most stable by a few kcal/mol, [21, 22] while for H_2O_2 the dissociated state turned out to be the lowest by nearly 2 kcal/mol [10]. These results correspond to coverages of 1ML or less. Adsorption energies were also investigated for formic acid upon rutile (110) [10, 13], through the characterization of several geometry configurations. At variance with findings in anatase (101) [8, 23], the authors concluded that the bidentate dissociated state was the most stable adsorption configuration in vacuum conditions.

The adsorption phenomena from a solution has been much less explored from a microscopic perspective using either experimental or computational tools, mostly because of the

complexity arising in the presence of a liquid phase. On one hand, most surface techniques with atomic resolution like XPS or LEED are not yet suited to be operative in solution. At the same time, the explicit inclusion of the solvent in first-principles simulations is still a very expensive practice, because of the large number of molecules required in any reasonable representation of a liquid phase. Remarkable exceptions are the computational works of Köppen and Langel [24], of Cheng and Sprik [25, 26], and of Cheng and Selloni [27], who have applied molecular dynamics approaches in the context of DFT to investigate processes at the TiO_2-water interface. In the first case, the competitive adsorption between water and hydrocarbons was studied with metadynamics, assessing that the greater affinity of water for the oxide would displace the organics pollutants from the surface [24]. In reference [25], the same kind of sampling was used to estimate the protonation free-energies of the interface, to eventually obtain the PZC (point of zero charge) of the titania surface. Finally, in the article by Cheng and Selloni, Car-Parrinello molecular dynamics simulations were employed to characterize the chemistry of the hydroxide ions at the water-anatase interface [27].

These studies have involved demanding molecular dynamics simulations at finite temperature, which are necessary to reliably reproduce the behavior of the system with an explicit solvent model, since a static calculation provides an inaccurate representation of the liquid state. As it is explained in the previous chapter, our continuum solvent implementation represents the solvation effect in an average way, making it meaninful to perform geometry optimization calculations [28–31]. Even if the solvent structure is omitted, all or part of the first solvation shells can be included explicitly to recover the specific solute-solvent interactions.

This is the path we follow in the present work, to examine the heterogeneous adsorption of H_2O, CH_3OH, H_2O_2 and HCOOH on anatase (101) and rutile (110) from an aqueous solution, and to study the effect of the dielectric constant in the absorption of these species. We use our recent implementation of the continuum solvent model for the treatment of solid-liquid interfaces, recently devised in the framework of DFT and the Car-Parrinello method [32].

6.2 Computational Methods

Electronic structure calculations in vacuum were performed using DFT in periodic boundary conditions, as implemented in the *Quantum Espresso* package [33]. This simulation code employs plane wave basis sets and pseudopotentials to represent the ion-electron interactions. The Kohn-Sham orbitals and charge density were expanded in planewaves up to a kinetic energy cutoff of 25 and 200 Ry, respectively. *k*-sampling was restricted to the

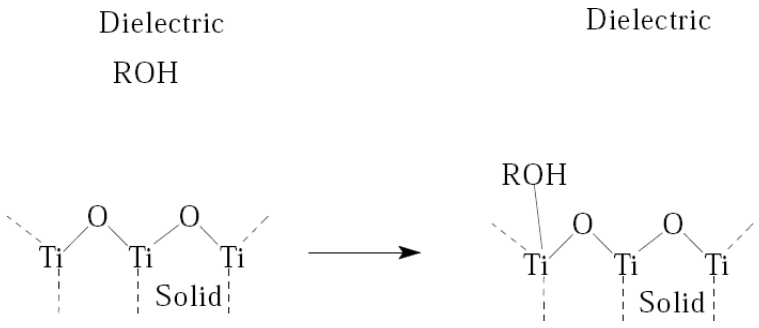

Figure 6.1. Representation of the adsorption process for ROH (H_2O, H_2O_2 or CH_3OH) in a continuum solvent.

Γ point. The Perdew-Wang approach (PW91) to the exchange-correlation energy [34, 35] and Vanderbilt [36] ultrasoft pseudopotentials were adopted to compute total energies and forces. The same standards and parameters were employed for the energy calculations and geometry optimizations in the presence of the solvent, for which we utilized the continuum model reported in Chapter 5. In this scheme the permittivity is defined as a function of the van der Waals radii, varying smoothly from 1.0 inside the surface up to the corresponding dielectric constant into the solvent region (set, in the case of water, to 79 in relative units) [32]. To represent the rutile (110) and anatase (101) surfaces, supercells of area (2x1) and (2x2) were respectively considered. In both cases, slabs were represented with four layers of TiO_2 units.

6.3 Results and Discussion

6.3.1 Water

In the first place, we calculated the energy involved in adsorbing one water molecule from the liquid phase: this process is sketched in Figure 6.1. We emphasize that the energy difference obtained from these calculations does not represent the adsorption energy of H_2O, but is the result of exchanging implicit and explicit water at the interface. In an optimal model, this energy difference should be equal to zero. In the present case, values of 0.28 and 0.14 kcal/mol were obtained, respectively, on anatase (101) and rutile (110) for a water molecule adsorbed molecularly. Such small values—compared to absolute adsorption energies, which are in the range of 20 kcal/mol—indicate that implicit solvation of the interface reproduces quite remarkably the energetics of explicit hydration. Figure 6.2 depicts the model structure of the slab with an adsorbed H_2O molecule, including a contour plot of the dielectric medium.

As it is the case for water, we note that also for any other molecule, the solvation

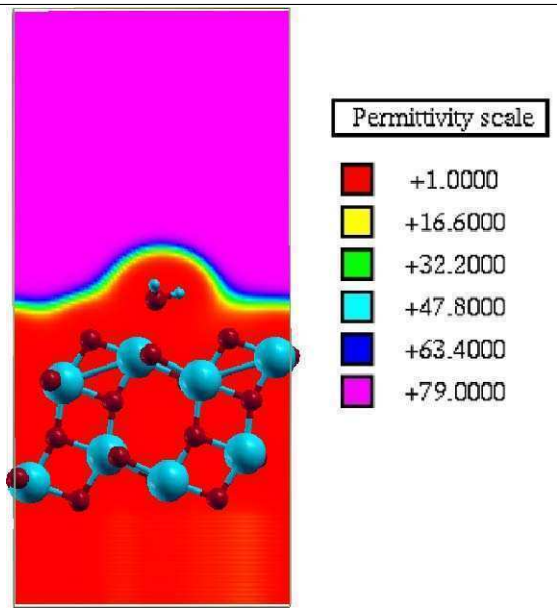

Figure 6.2. Slab model of the anatase (101) surface with an adsorbed water molecule, displaying a contour plot of the dielectric medium.

model employed here does not provide the absolute adsorption energy, but the relative energy associated with the replacement of continuum solvation by the given adsorbate. Alternatively, in a more elaborate treatment, specific interactions at the interface can be captured to a great extent by including explicitly a water monolayer. This approach is represented in Figure 6.3.

Whereas water on the anatase (101) surface has been characterized from first-principles at the gas interface in a series of studies [1–3], we are not aware of any equivalent effort addressing the adsorption in solution, aside from the work on hydroxide ions cited above [27]. According to our computations at low coverage, the gap between the molecular and dissociative modes is roughly 12 kcal/mol. Interactions in the monolayer tend to equalize the two adsorption modes: for a monolayer in the gas phase, the energy of the molecular state lies only 3.3 kcal/mol below the dissociative state (Table 6.1). In the presence of a continuum solvent this energy difference is barely modified, diminishing in just 0.3 kcal/mol. In general, it will be seen that the dielectric medium contributes to increase the hydrogen bond lengths in 10-20%. This is the consequence of the dielectric screening on the H-bonds, which are mostly electrostatic interactions. Geometry optimization of a water ML on the (101) face, shows that for the molecular mode the distance between O(2c)[1] and H-OH (the hydrogen belonging to the water molecule) is enlarged from 1.9 Å in vacuum to 2.5 Å in the solvent. This is displayed in Figure 6.4, where the

[1]From now on, we denote O(2c) to the bi-coordinated bridging oxygen atom on the surface, and Ti(5c) to the 5-fold coordinated titanium atom.

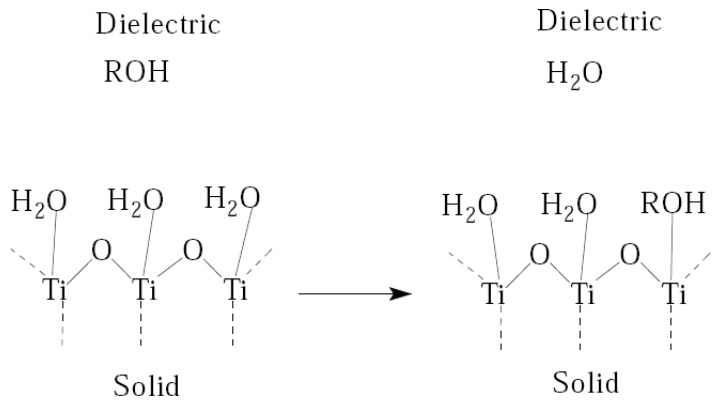

Figure 6.3. Representation of the adsorption process for ROH (H_2O_2 or CH_3OH) in a continuum solvent, considering the first hydration layer explicitly.

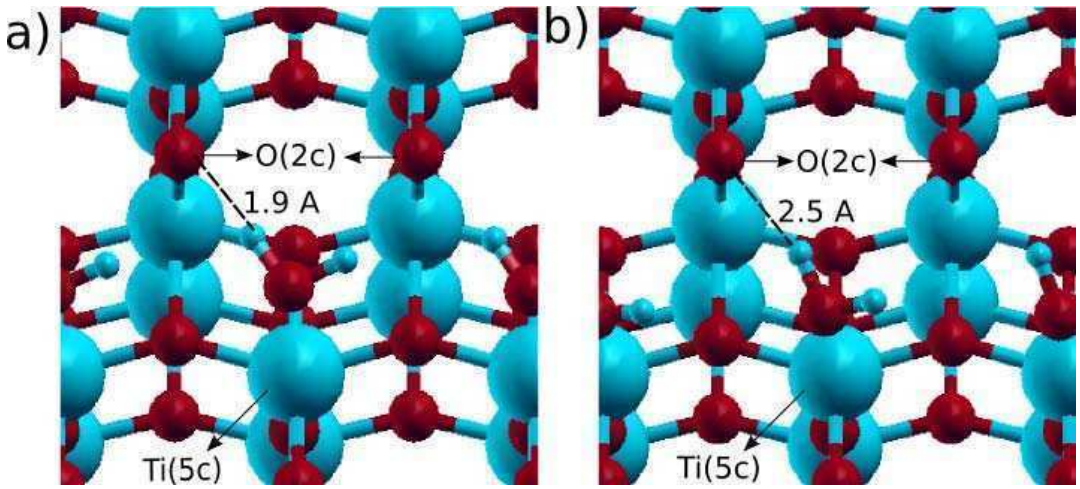

Figure 6.4. Optimized structures for a water monolayer molecularly adsorbed on anatase (101): (a) in vacuum; (b) in the continuum solvent.

water molecules are shown to rotate from their vacuum positions, to expose one hydrogen atom in the direction perpendicular to the surface. Interestingly, the dielectric is inducing the same kind of configuration as expectable in an explicit solvation framework, in which the adsorbed H_2O would be involved in hydrogen bonding with the bulk molecules. This reorientation was actually observed in molecular dynamics simulations including explicit water molecules [27].

A similar effect on bond lengths can be observed in the dissociated ML: the distance from the hydrogen H-O(2c) and the oxygen bound to Ti(5c) is increased from 2.8 Å in vacuum to 3.1 Å in the dielectric. It can be seen in Figure 6.5 how the hydrogen atoms adsorbed to O(2c) become perpendicular to the surface in the presence of the solvent. The weakening of the H-bonding network is similar in both the dissociated and the molecular

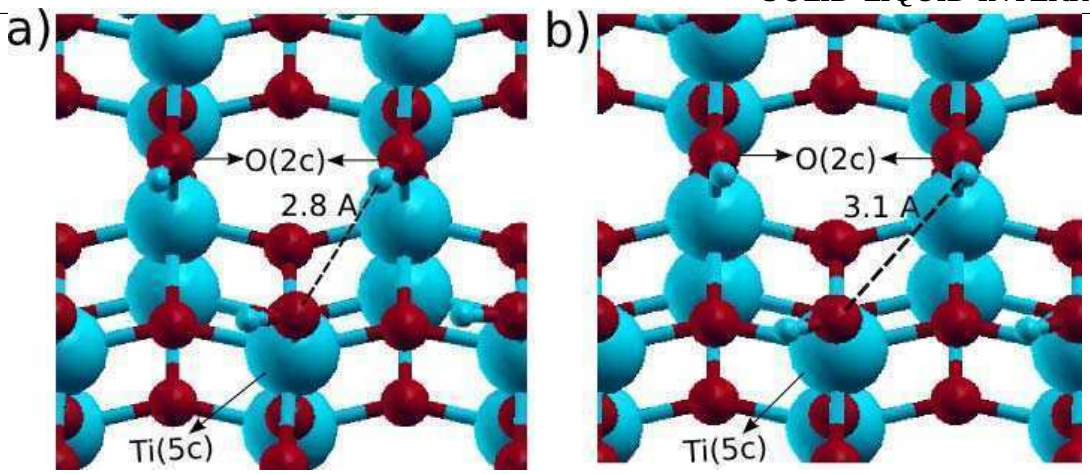

Figure 6.5. Optimized structures for a water monolayer dissociatively adsorbed on anatase (101): (a) in vacuum; (b) in the continuum solvent.

states, and as a consequence the energy difference is virtually not affected by the dielectric.

According to previous reports mentioned above [9–13], energy differences between the different adsorption modes in rutile (110) may be small. In view of this, the composition of a water monolayer at the heterogeneous interface was analyzed taking into account the possibility of mixed states. In vacuum, for slabs of four layers width or wider, water monolayers exhibit molecular adsorption. In our own gas phase calculations, mixed and dissociative modes turn out to be 2.0 and 6.1 kcal/mol higher in energy than the molecular adsorption. Incorporation of solvent effects does not alter this trend, predicting energy differences of 2.5 and 5.9 kcal/mol with respect to the mixed and dissociative pathways, respectively. Changes in bond lengths resulting from the dielectric medium in the monolayer of molecular adsorbed water indicate a strengthening of the Ti(5c)-water bond, and a strong screening of the hydrogen bonds existing between water and the surface and with itself. In the case of the dissociative adsorption, the major effect of the presence of the dielectric medium is on the hydrogen bonding network within the water monolayer. On one hand it produces some destabilization by elongating of the hydrogen bonds between adjacent water molecules, while on the other it provokes the shortening of the distance among the H-O(2c) and the oxygen of OH-Ti(5c). As a result, there is only a small difference between the vacuum and solution energetics, as indicated above.

Our results are consistent with previous simulations in the presence of multilayers, which found that the molecular adsorption will be the preferred path [2, 15]. In the literature, water adsorption at the TiO_2-liquid interface is often assumed to be dissociative and therefore represented with ionized OH^- groups. We note here that this qualitative and widespread conception of the interface, possibly correct for amorphous and defective sur-

Table 6.1. Adsorption energies of water in the different conditions examined, including the continuum solvent with and without an explicit water monolayer. Energies are given in kcal/mol and are relative to the molecular state, which is the most stable.

	anatase (101)	rutile (110)	
	dissociated	dissociated	mixed
Gas phase	12.2	3.7	—
Solvent	11.3	5.6	—
Gas phase/Water ML	3.3	6.1	2.0
Solvent/Water ML	3.0	5.9	2.5

faces, may not be accurate for anatase (101) and rutile (110), as shown by the DFT results in the presence of several water layers or in the continuum solvent. Instead, molecular adsorption will predominate on stoichiometric surfaces, with only a very small fraction of the sites occupied by ionized OH^- anions, in equilibrium with the dissociation of bulk water. Dissociation, on the other hand, can most likely occur at vacancies [1, 37].

The adsorption energies for water on anatase (101) and rutile (110) are summarized in Table 6.1. [2] Energies are given with respect to molecular adsorption, which is the most stable for all cases. In the following sections, results for methanol and hydrogen peroxide adsorption energies are presented and analyzed, in the absence and in the presence of a molecularly adsorbed water monolayer, which, as discussed in this section, is the stable form of water at the solid-liquid interface.

6.3.2 Methanol

For the methanol molecule, we have examined three different adsorption paths: molecular, dissociative via the C-O bond, and dissociative via the O-H bond. We will denote these mol, disCO, and disOH respectively. These different configurations are displayed in Figure 6.6, and the adsorption energies are shown in Table 6.2. In agreement with previous calculations [6, 23], we have found that in the gas phase methanol adsorbs molecularly on anatase (101).[3] On rutile, the dissociative (disOH) and the molecular adsorption modes are almost energetically degenerate, in line with the recent calculations by Sánchez and coworkers [22]. Besides, it can be seen that the relative stability of the three adsorp-

[2] As in the case of methanol, cited in the next footnote, for water dissociation process exist the same two different configurations. For this reason the adsorption energy value varies with respect to the one cited in the previous chapter 5, table 5.2. See reference [3].

[3] We note that upon dissociation of the C-O bond on anatase (101), two inequivalent oxygen surface sites are available to accommodate the CH_3 fragment. In particular, the adsorption energy reported in Table 6.2 for the disCO configuration differs from the value informed in reference [6] because they correspond to different configurations.

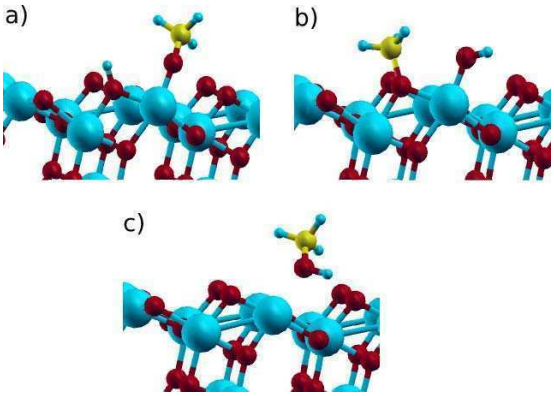

Figure 6.6. Adsorption modes examined for methanol: (a) disOH, (b) disCO, (c) mol, standing for, respectively, dissociation across the O-H bond, dissociation across the C-O bond, and molecular adsorption. The structures correspond to the anatase (101) surface.

Table 6.2. Adsorption energies of methanol (kcal/mol) in the different conditions examined, including the continuum solvent with and without an explicit water monolayer. The different adsorption modes disOH, disCO and mol, are depicted in Figure 6.6.

	anatase (101)			rutile (110)		
	mol	disOH	disCO	mol	disOH	disCO
Gas phase	-19.0	-15.6	-12.8	-19.2	-17.2	-13.9
Solvent	3.6	6.4	12.1	3.4	6.6	8.1
Solvent/Water ML	0.5	3.8	12.4	2.4	4.7	8.9

tion modes remains unaltered throughout the three distinct environments. However, the adsorption energies in the solvent are positive in all cases, meaning that methanol adsorption from an aqueous solution would be unfavored, having to compete against water. It is interesting to note that the surface larger affinity for water in a solvent environment is not always reflecting the trends in the gas phase. While water exhibits a higher adsorption energy than methanol on anatase (20.3 and 19.0 kcal/mol for H_2O and CH_3OH, respectively), the opposite is true on rutile (16.7 and 19.2 kcal/mol). The reason for this can be tracked in the hydrogen bond network arising within the water monolayer, which further stabilizes the adsorption with respect to the low coverage case.

A recurrent consequence of the dielectric screening is the disruption of hydrogen bonds. On the (101) face, an hydrogen bond between the molecularly adsorbed methanol and the bridging oxygen is present in vacuum. This bond is lost when immersed in the dielectric medium, but is recovered when the first water monolayer is included explicitly. In rutile (110), on the other hand, this hydrogen bond continues to exist when the dielectric effect is introduced. When covered by a water monolayer, in both interfaces an additional H-

bond is formed between methanol and one of the H_2O molecules. Hence, addition of the dielectric medium without considering the first water ML explicitly can affect the hydrogen bond network, depending on surface structure. For rutile(110), where the surface atoms Ti(5c) and O(2c) are nearer than in anatase (101), the hydrogen bonds between methanol and the surface do not disappear in the presence of the dielectric medium. This is not the case for anatase (101). When the first water ML is included explicitly, it has two main consequences for anatase (101): the formation of new hydrogen bonds with H_2O, and the restoration of the lost H-bonds with the surface. For rutile(110), only the first consequence is observed, and for this reason, the effect seen in Table 6.2 when the first solvation shell is included, is greater in anatase.

Turning now to the dissociated states, Table 6.2 shows that addition of explicit water has a stabilization effect in the disOH configuration on both surfaces, but not in disCO. While the dissociated CH_3O group may establish an extra hydrogen bond with one of the water molecules, this does not occur in the case of disCO in which the CH_3 moiety tenuously interact with the water monolayer.

These results support the idea that an aqueous phase promotes the desorption of methanol into the solution. Moreover, explicit consideration of the first solvation layer is important to account for specific interactions. In general it was observed that the dielectric screening tends to weaken the hydrogen-bonds between the surface and the adsorbate, and also the O-Ti adsorbate-surface interactions. Incorporation of explicit water molecules reverts this effect, by excluding the dielectric from the region adjacent to the surface. In a typical electrochemical model based on a continuum representation of the interface, the permittivity is taken to vary slowly from 1 to its value in bulk, several angstroms away from the surface. The reduced mobility of the molecules belonging to the first solvation layer restricts the ability of these molecules to align their dipoles in an electric field, which is a measure of the dielectric constant [38]. Inclusion of the first solvation layer reestablishes specific interactions and at the same time acts as a shield to the dielectric.

In Figure 6.7, we investigate the effect of the dielectric constant on the adsorption of methanol on anatase. For a solvent of intermediate or low permittivity, exhibiting no hydrogen bonds, the effect of an explicit monolayer would be less important than in water. The interaction energies in Figure 6.7 were computed in the absence of a solvation layer, and for this reason, we expect the lower the permittivity, the more reliable the estimates to the adsorption energies in solution. The graph suggests that methanol would not significantly adsorb from solutions with a dielectric constant larger than 45, and that molecular adsorption will be the most favored in any case.

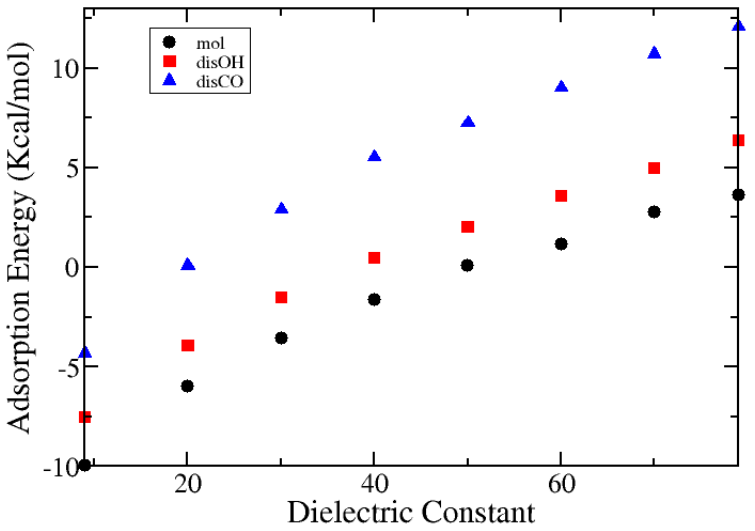

Figure 6.7. Influence of the dielectric constant on the adsorption energy of methanol on anatase (101)

6.3.3 Hydrogen peroxide

Adsorption energies for H_2O_2 in vacuum are reported in Table 6.3. In agreement with previous calculations [10], dissociative adsorption turns out to be the most stable on rutile (110). For anatase (101), instead, the molecular adsorption exhibits the lowest energy. Figure 6.8 depicts the relaxed configuration on the (101) face in solution. It can be seen in Table 6.3 that the solvent stabilizes the dissociated form on anatase: this effect is observed in the presence and in the absence of the water monolayer. The dissociative adsorption predicted here seems to be at variance with the results by Mattioli and collaborators [7], who examined the surface interaction of H_2O_2 embbeded in a water bilayer. Whether total energy calculations in a continuum solvent and an explicit monolayer are more reliable than in a water bilayer to represent the solid-liquid interface, remains an open question. Understanding the effect of a limited number of layers in comparison to the dielectric medium, would require an analysis involving a progressive increase of the number of water molecules in the simulation.

Adsorption energies are close to zero, implying that affinities of H_2O and H_2O_2 for the oxide surface are comparable in solution. In vacuum, hydrogen peroxide is around 4 kcal/mol less stable than water on the (101) surface. This difference decreases in the solvent, yet the water continues to exhibit the largest adsorption energy. For rutile (110), dissociative and molecular adsorption become energetically equivalent, and, as for the (101)

Table 6.3. Adsorption energies of hydrogen peroxide (kcal/mol) in the different conditions examined, including the continuum solvent with and without an explicit water monolayer.

	anatase (101)		rutile (110)	
	molecular	dissociated	molecular	dissociated
Gas phase	-16.5	-14.7	-16.3	-17.3
Solvent	4.9	3.9	5.3	2.5
Solvent/Water ML	2.2	0.9	0.1	0.3

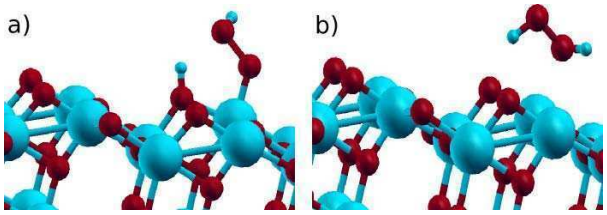

Figure 6.8. Adsorption modes examined for H_2O_2: (a) dissociated, (b) molecular. The structures correspond to the anatase (101) surface.

surface, also comparable with the adsorption of water. The adsorption energies when only the dielectric medium is considered, are more positive than the ones obtained by including water molecules explicitly. An inspection of the relaxed geometries in solution shows that, once again, this is a consequence of the dielectric environment in the immediacy of the surface, weakening specific interactions such as hydrogen bonds between the adsorbate and the surface.

6.3.4 Formic acid

The adsorption of the formic acid molecule exhibits a complex scenario due to two major causes: the possibility to adsorb via two inequivalent oxygen atoms belonging to the carboxylic group, and the particular molecular geometry. The inequivalent oxygen atoms allow for molecular monodentate adsorption in two different configurations, denoted as mono-O and mono-OH along this work (see Figure 6.9 (a) and (b)). Besides, the formic acid molecular dimensions admit a bidentate adsorption mode, through both oxygen atoms of the -COOH group. This is shown in Figure 6.9 (c) and (d), where (c) and (d) describe a dissociative and a molecular mode, respectively. Finally, a monodentate dissociative adsorption mode can be proposed as shown in Figure 6.9 (e). Other configurations could be conceived, nevertheless, given the large amount of accessible configurations, we restrict this charaterization to the five different modes shown in Figure 6.9.

Our simulations on anatase (101) as well as on rutile (110) in the gas phase (Table

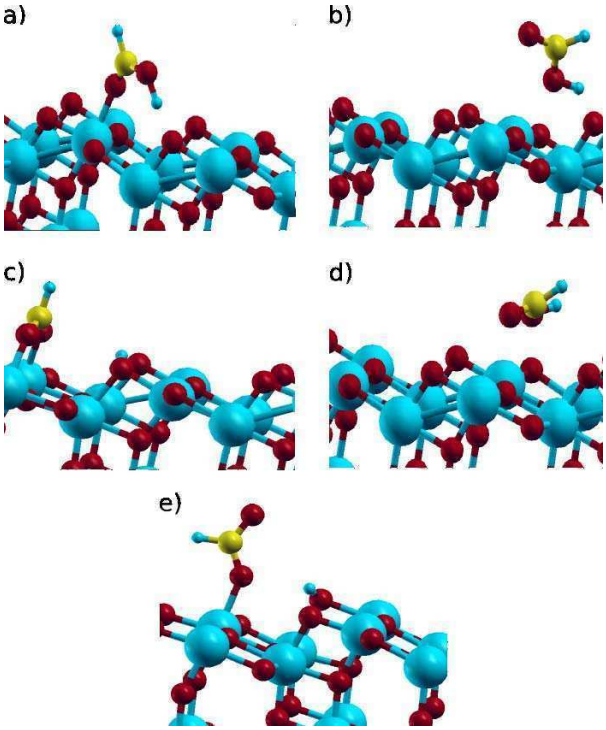

Figure 6.9. Adsorption modes examined for formic acid molecule: (a) mono-O, (b) mono-OH, (c) bi-d, (d) bi-m and (e) mono-d. Mono-O (a) and mono-OH (b) stand for the monodentate molecular adsorption through the inequivalent oxygen atoms belonging to the carboxyl group (-COOH). Bi-d (c) and bi-m (d) refer to the bidentate dissociative and molecular modes. Finally, mono-d (e) identifies the dissociative adsorption through one oxygen atom, which in the case of our gas phase simulations on anatase (101) converges to the mono-O (a) configuration. The shown structures correspond to the anatase (101) surface.

Table 6.4. Adsorption energies (kcal/mol) of formic acid in the different conditions examined, in the presence and in the absence of the continuum solvent and of an explicit water monolayer. The different adsorption modes (mono-O, mono-OH, mono-d, bi-m and bi-d) are depicted in Figure 6.9. Not stable indicates that no optimizations converged to that structure.

	anatase (101)				
	mono-O	mono-OH	bi-m	mono-d	bi-d
Gas phase	-26.7	-14.2	-7.2	not stable	-25.2
Solvent	4.5	7.9	7.2	7.6	12.6
Solvent/Water ML	-2.1	3.2	-2.7	-1.2	0.8
	rutile (110)				
	mono-O	mono-OH	bi-m	mono-d	bi-d
Gas phase	-14.2	-14.3	-23.9	-18.2	-29.4
Solvent	1.5	8.1	not stable	0.8	-0.7
Solvent/Water ML	0.5	0.9	not stable	1.5	-6.2

6.4) reproduce most of the adsorption energies published before [8, 10, 13, 23], finding agreement in both surfaces regarding the most stable geometry configurations. Some differences arise on the energies for configurations with intermediate affinities, such as the mono-d configuration on anatase (101). This last example converges to a stable adsorption geometry in a previous investigation [8], but we found it unstable in our present simulations, where it reverts to the mono-O configuration as a in the optimization procedure. We believe such a difference may be related to the initial configurations adopted to perform the calculations.

It can be observed from Table 6.4 that the adsorption energies in the gas phase for the bidentate modes depend on the surface. As mentioned before, adjacent bridge oxygen atoms in the rutile (110) surface are at a closer distance than in the anatase (101) surface. In general, however, the dissociated form of the bidentate interaction seems to predominate on both surfaces.

Results in Table 6.4 show that the dielectric medium plays a destabilizing role, originating in the competence against the implicit water for the surface sites. As in the case of methanol, inclusion of the dielectric induces a loss of the hydrogen bonds exhibited in vacuum, as those formed by the mono-OH configuration on both surfaces. Addition of the explicit water monolayer reverts this effect establishing an hydrogen-bond network. The mono-d mode constitutes an exception in the sense that implicit or explicit hydration stabilize its adsorption on anatase. On the other hand, the solvent modifies the preferred adsorption mode on anatase: it switches from a monodentate molecular configuration in vacuum to a molecular bidentate mode in solution. On rutile, instead, the bidentate dissociative mode is always the most favored. We note that for reasons related to the supercell

size, we have not considered the case of the bidentate species co-adsorbed with a water ML in rutile[4]. When the continuum solvent plus the first solvation shell are considered for anatase, negative adsorption values are obtained for the mono-O, bi-m, and the mono-d species. The first two appear to be the only capable to displace molecular water from the surface.

6.4 Conclusions

In general, in this study it was found that even though the solvent may marginally affect the energies of the different accessible absorption modes, its effect has never proved to be large enough as to revert the trend observed in vacuum, with the sole exceptions of H_2O_2 on the (101) surface, for which the solvent environment induces the dissociative adsorption, and of the bidentate mode of HCOOH, also on anatase (101), for which the solvent inverts the energetics and induces molecular adsorption. Our results support the idea that water adsorbs molecularly at the interface of anatase (101) and rutile (110). In the surface oxide literature, the TiO_2 interface is envisioned as consisting predominantly of ionized hydroxyl groups (—O^-) [39]. We think this representation is not accurate in the context of crystalline surfaces: most water molecules at the interface will be undissociated, in equilibrium with some amount of —O^- groups (the experimental PZC of rutile and anatase are around 7 and 4, respectively) [40]. In any case, we want to emphasize that the degree of hydroxylation of the interface will depend very much on the synthetic route: amorphous TiO_2 materials obtained from sol-gel processes involving hydrolysis and condensation [41] will be more likely to leave terminal, exposed Ti-OH functions, which will partially ionize and yield Ti-O^- groups in solution.

The neglect of the first solvation shell when using the continuum model, tends to debilitate the electrostatic interactions between the adsorbate and the surface, enhancing the intermolecular distances. For configurations exhibiting hydrogen bonds in vacuum, the presence of the dielectric medium will normally lead to a loss of stability. The explicit addition of the first water monolayer prevents the weakening of intermolecular interactions, allowing at the same time the formation of hydrogen bonds within the monolayer. The dielectric constant of a liquid represents accurately its electrostatic screening in bulk; as the interface is approached, the reduced mobility of the solvent layers will diminish their ability to respond to an external electric field, resulting in a smaller effective dielectric constant. For these reasons, we remark the importance of including the first water monolayer explicitly in solid oxides-liquid interfaces. Alternatively, a model with a distance-dependent

[4]The representation of explicit solvation in the case of rutile for bidentate species would have requested the expansion of the supercell, because the adopted (110) surface model exposes only two Ti(5c) sites.

permittivity could be implemented [38], but this will require a number of additional parameters.

The positive adsorption energies reported in Tables 6.2, 6.3 and 6.4 suggest that the adsorption process for methanol, hydrogen peroxide and formic acid on anatase (101) and rutile (110) will not be thermodynamically favored in aqueous solution. Yet, some of these values are small or slightly negative—within the accuracy of the method—, and therefore we can not rule out that at room temperature a small fraction of the molecules present in the solution might be adsorbed on the surface in those particular modes reflecting the most stable configurations.

References

[1] A. Tilocca and A. Selloni, *J. Phys. Chem. B* 108, (2004), 4743.

[2] A. Tilocca and A. Selloni, *Langmuir* 20, (2004), 8379.

[3] A. Vittadini, A. Selloni, F. Rotzinger, and M. Grätzel, *Phys. Rev. Lett.* 81, (1998), 2954.

[4] G. S. Herman, Z. Dohn´alek, N. Ruzycki, and U. Diebold, *J. Phys. Chem. B* 107, (2003), 2788–2795.

[5] U. Diebold, *Surf. Sci. Rep.* 48, (2003), 53–229.

[6] A. Tilocca and A. Selloni, *J. Phys. Chem. B* 108, (2004), 19314.

[7] G. Mattioli, F. Filippone, R. Caminiti, and A. A. Bonapasta, *J. Chem. Phys. C* 112, (2008), 13579.

[8] A. Vittadini, A. Selloni, F. Rotzinger, and M. Gratzel, *J. Phys. Chem. B* 104, (2000), 1300.

[9] L. A. Harris and A. A. Quong, *Phys. Rev. Lett.* 93, (2004), 086105.

[10] S. Bates, G. Kresse, and M. J. Gillan, *Surf. Sci.* 409, (1998), 336.

[11] P. J. D. Lindan and C. Zhang, *Phys. Rev. B* 72, (2005), 075439.

[12] J. Oviedo, R. S. de Armas, M. A. S. Miguel, and J. F. Sanz, *Phys. Chem. C Lett.* 112, (2008), 17737–17740.

[13] C. L. Pang, R. Lindsay, and G. Thornton, *Chem. Soc. Rev.* 37, (2008), 2328–2353.

[14] V. M. Sánchez, J. A. Cojuloun, and D. A. Scherlis, *J. Phys. Chem. C* 114, (2010), 11522–11526.

[15] C. Zhang and P. J. D. Lindan, *J. Chem. Phys.* 119, (2003), 9183.

[16] P. M. Kowalski, B. Meyer, and D. Marx, *Phys. Rev. B* 79, (2009), 115410.

[17] M. B. Hugenschmidt, L. Gamble, and C. T. Campbell, *Surf. Sci.* 302, (1994), 329.

[18] M. A. Henderson, *Surf. Sci.* 355, (1996), 151.

[19] M. A. Henderson, *Langmuir* 12, (1996), 5093.

[20] M. A. Henderson, *Surf. Sci.* 400, (1998), 203.

[21] S. Bates and M. J. Gillan, *J. Phys. Chem. B* 102, (1998), 2017.

[22] R. Sanchez de Armas, J. Oviedo, M. A. S. Miguel, and J. F. Sanz, *J. Phys. Chem. C* 111, (2007), 10023–10028.

[23] A. Vittadini, M. Casarin, and A. Selloni, *Theor Chem Acc* 117, (2007), 663–671.

[24] S. Köppen and W. Langel, *Phys. Chem. Chem. Phys.* 10, (2008), 1907.

[25] J. Cheng and M. Sprik, *J. Chem. Theory Comput.* 6, (2010), 880–889.

[26] J. Cheng and M. Sprik, *Phys. Rev. B* 82, (2010), 081406.

[27] H. Cheng and A. Selloni, *Langmuir* 26, (2010), 11518.

[28] I. N. Levine, *Química Cuántica*, Pearson Educación (**2001**).

[29] J. Tomasi, B. Mennucci, and R. Cammi, *Chem. Rev.* 105, (2005), 2999.

[30] C. J. Cramer and D. G. Truhlar, *Chem. Rev.* 99, (1999), 2161.

[31] T. Schlick, *Molecular Modeling and Simulation*, Springer-Verlag, New York (**2002**).

[32] V. M. Sánchez, M. Sued, and D. A. Scherlis, *J. Chem. Phys.* 131, (2009), 174108.

[33] P. Giannozzi, S. Baroni, N. Bonini, M. Calandra, R. Car, C. Cavazzoni, D. Ceresoli, G. L. Chiarotti, M. Cococcioni, I. Dabo, A. D. Corso, S. de Gironcoli, S. Fabris, G. Fratesi, R. Gebauer, U. Gerstmann, C. Gougoussis, A. Kokalj, M. Lazzeri, L. Martin-Samos, N. Marzari, F. Mauri, R. Mazzarello, S. Paolini, A. Pasquarello, L. Paulatto, C. Sbraccia, S. Scandolo, G. Sclauzero, A. P. Seitsonen, A. Smogunov, P. Umari, and R. M. Wentzcovitch, *J. Phys.: Condens. Matter* 21, (2009), 395502.

[34] J. P. Perdew and Y. Wang, *Phys. Rev. B* 45, (1992), 13244.

[35] J. P. Perdew and et al, *Phys. Rev. B* 46, (1992), 6671.

[36] D. Vanderbilt, *Phys. Rev. B* 41, (1990), 7892–7895.

[37] A. Tilocca and A. Selloni, *J. Chem. Phys.* 119, (2003), 7445.

[38] M. C. F. Wander and A. E. Clark, *J. Phys. Chem. C* 112, (2008), 19986.

[39] A. E. Regazzoni, P. Mandelbaum, M. Matsuyoshi, S. Schiller, S. Bilmes, and M. A. Blesa, *Langmuir* 14, (1998), 868.

[40] M. Kosmulski, *J. Colloid Interface Sci.* 253, (2002), 77.

[41] C. J. Brinker and G. W. Scherrer, *Sol-Gel Science, The Physics and Chemistry of Sol-Gel Processing*, Academic Press, San-Diego, CA (**1990**).

Chapter 7

A hybrid Quantum Mechanics Molecular Mechanics formulation for extended systems

7.1 Introduction

As it was pointed out in chapter 1, hybrid Quantum Mechanics-Molecular Mechanics (QM-MM) schemes consider the simulation system as a sum of two different subsystems: solute (QM fragment) and solvent (MM fragment) [1–6]. The particles are assigned to these two groups according to their role: atoms directly involved in bonds breaking or forming, or in polarization or charge transfer effects, must be considered in the QM region, whereas those atoms not participating in these processes can be part of the MM subsystem. These two groups are described at different levels with different Hamiltonians, but they interact with each other self-consistently.

This hybrid methodology has been applied exhaustively for finite chemical and biological systems. In particular, it was employed to describe chemical reactions inside the active site of proteins. In this type of simulations the solute described quantum-mechanically comprises the active site, while the rest of the protein plus hydration water molecules is called the solvent [6–10]. Hybrid QM-MM methodologies were also used to model proton transfer reactions in water clusters environments [3, 11]. Applications to solids included different type of interfaces, where the surface was modeled as a finite cluster: these works have addressed solid-liquid interfaces [12], metal-organic interfaces [13], and oxide interfaces [14]. On the other hand, the QM-MM methodology applied in periodic boundary conditions (PBC) has been rarely reported in the literature. A few examples in which periodicity was imposed to the MM region only to simulate dilute solutions can be found for semiempirical [2, 15, 16] or first-principles approaches [15, 16]. Laino et al. [1, 17] developed a QM-MM hybrid method in periodic boundary conditions based on Gaussian basis sets, which was tested on the simulation of surface defects present at the α-quartz phase

of silica. To the best of our knowledge only Yarne et al. [4] developed a hybrid QM/MM methodology imposing PBC to the whole system in a PPW-DFT framework. In this case electrons were confined to a smaller unit cell inside the supercell needed to describe the whole system, and periodicity was limited to 1 or 2-D.

QM approximations to solve the Schrödinger equation have been introduced in chapter 2. For the MM region, the potential energy of the system is computed from a force field, expressed as a sum of simple functions of the atomic coordinates and a series of parameters [18]. In the MM approach, atoms are typically treated as point charges of charge q_i interacting with each other through electrostatics, dispersive-repulsive and harmonic potentials, so that the molecular mechanics energy E_{MM} is the sum of three contributions:

$$E_{MM} = E_{ele} + E_{LJ} + E_{bond} \tag{7.1}$$

where E_{ele}, E_{LJ} and E_{bond} stand for the electrostatic, the Lennard-Jones, and the bonding energy respectively. In turn, these terms are normally computed as:

$$E_{ele} = \sum_{i=1}^{N} \sum_{j=i+1}^{N} \frac{q_i q_j}{4\pi\epsilon_0 R_{ij}} \tag{7.2}$$

$$E_{LJ} = \sum_{I} \sum_{J} 4\epsilon_{IJ} \left[\left(\frac{\sigma_{IJ}}{|\mathbf{R}_I - \mathbf{R}_J|} \right)^{12} - \left(\frac{\sigma_{IJ}}{|\mathbf{R}_I - \mathbf{R}_J|} \right)^{6} \right] \tag{7.3}$$

$$E_{bond} = \sum_{bonds} \frac{k_i}{2}(l_i - l_{i0})^2 + \sum_{angles} \frac{a_i}{2}(\theta_i - \theta_{i0})^2 + \sum_{dihedrals} \frac{v_n}{2}(1 + \cos(n\omega - \gamma)) \tag{7.4}$$

In the second of these three equations σ_{IJ} and ϵ_{IJ} are the Lennard-Jones radius and interaction energy between atoms I and J. In the last expression, k_i, a_i, and v_n, represent force constants for the harmonic potentials controlling bond lengths, angles and torsions, respectively.

In the QM-MM methodology the Hamiltonian and the energy of the system are written as:

$$\hat{H}_{tot} = \hat{H}_{QM} + \hat{H}_{MM} + \hat{H}_{QM-MM} \tag{7.5}$$

$$E_{tot} = E_{QM} + E_{MM} + E_{QM-MM} \tag{7.6}$$

where H_{QM-MM} (and the related energy E_{QM-MM}) is a coupling term describing the interaction between the two regions of the system. In this thesis we present the formu-

lation of a hybrid QM-MM method in a PPW framework, more specifically in the Car-Parrinello approach of the Quantum Espresso code [19]. We have implemented in the present setting the electrostatic and van der Waals interactions between QM and MM water molecules. The ultimate goal is to have available a hybrid QM-MM methodology in PBC to describe two phases at different levels, e.g., the solid quantum-mechanically and the solvent classically. This one is a very interesting approach to undertake molecular dynamics studies of surface reactivity on intefaces with high accuracy at an affordable computational cost. Before this methodology can be applied to the simulation of solid interfaces, though, the incorporation of potentials to describe the solid phase is still needed. Even so, we deemed important to include the fundamentals of this approach at the present stage, namely because—to the best of our knowledge—no other QM-MM model has been based on this framework, but also because its development has been a core subject of this thesis work.

7.2 Implementation of the hybrid QM-MM methodology in a PPW framework

7.2.1 The energy

Within a QM-MM hybrid methodology the energy can be calculated as a sum of three different contributions, as stated in Eq.7.6. In the Pseudopotential Plane Wave (PPW) approach (see section 2.2.4), used in the Quantum Espresso code, the QM energy can be cast as:

$$E_{QM} = E_{KS}[\rho] = T_e[\rho] + E_H[\rho] + E_{ii} + E_{PS}^{loc}[\rho] + E_{PS}^{nl} + E_{XC}[\rho] \tag{7.7}$$

On the right hand side of the above equation, from left to right, there is the kinetic energy of the electrons, the Hartree energy, the ion-ion repulsion, the local and non-local contributions to the pseudopotential energies, and the exchange-correlation functional. One of the key points in our hybrid approach is to conceive the MM atoms in the same way as the pseudoions of the QM region within the PPW framework. There are basically two differences between MM and QM ions in this case: (i) the MM atoms do not include a non-local pseudopotential term, and (ii) the MM ions can have a partial charge, which can be either negative or positive, according to the charge parameter in the force field.

In the PPW method, the electrostatic contribution comes from the sum of the second, third and fourth terms on the right hand side of equation 7.7:

$$E_{es,QM}[\rho] = E_H[\rho] + E_{PS}^{loc}[\rho] + E_{ii}$$

$$= \frac{1}{2}\iint \frac{\rho(\mathbf{r})\rho(\mathbf{r'})}{|\mathbf{r}-\mathbf{r'}|}d\mathbf{r}d\mathbf{r'} + \sum_{s=1}^{N_s}\sum_{l=1}^{P_s}\int \rho(\mathbf{r})v_{PS}^{loc,s}(|\mathbf{r}-\mathbf{R}_I|)d\mathbf{r} + \frac{1}{2}\sum_{I=1}^{P}\sum_{J=1,J\neq I}^{P}\frac{Z_I Z_J}{|\mathbf{R}_I-\mathbf{R}_J|} \quad (7.8)$$

where $\rho(\mathbf{r})$ is the electronic charge distribution, s indicates the atomic species, N_s is the number of different atomic species, and $v_{PS}^{loc,s}$ is the local pseudopotential for each species. Z_I is the ionic charge of the nuclei (which amounts to the atomic number minus the valence electrons) and $\mathbf{R}_I$ their positions. P stands for the number of ions and P_s for the number of ions corresponding to the atomic species s. In the computational code the electronic charge is taken as positive and the ionic charge as negative: in this chapter we will follow the same convention.

If we define the Hartree energy $\tilde{E}_H[\rho]$ as a function of the total charge density ρ_T[1] ($\rho_T = \rho_\alpha + \rho$, with ρ_α the total ionic density as defined in section 2.2.4 to be used in the Ewald sum), then equation 7.8 can be rewritten in the following way[2]:

$$E_{es,QM} = \tilde{E}_H[\rho] + \tilde{E}_{ii} + \tilde{E}_{PS}^{loc}[\rho] \quad (7.9)$$

where each term above is:

$$\tilde{E}_H[\rho] = \frac{1}{2}\iint \frac{\rho_T(\mathbf{r})\rho_T(\mathbf{r'})}{|\mathbf{r}-\mathbf{r'}|}d\mathbf{r}d\mathbf{r'} \quad (7.10)$$

$$\tilde{E}_{PS}^{loc}[\rho] = \int \rho(\mathbf{r})\left(\sum_{s=1}^{N_s}\sum_{l=1}^{P_s} v_{PS}^{loc,s}(|\mathbf{r}-\mathbf{R}_I|)d\mathbf{r} - \int \frac{\rho_\alpha(\mathbf{r'})}{|\mathbf{r}-\mathbf{r'}|}\right)d\mathbf{r} \quad (7.11)$$

$$\tilde{E}_{ii} = \frac{1}{2}\left(\sum_{I=1}^{P}\sum_{J=1,J\neq I}^{P}\frac{Z_I Z_J}{|\mathbf{R}_I-\mathbf{R}_J|} - \iint \frac{\rho_\alpha(\mathbf{r})\rho_\alpha(\mathbf{r'})}{|\mathbf{r}-\mathbf{r'}|}d\mathbf{r}d\mathbf{r'}\right) \quad (7.12)$$

To get these three expression from the previous ones, ρ_α is added to E_H and substracted from E_{PS}^{loc} and from E_{ii}, so that the sum of the three terms (the electrostatic energy) is conserved. In our QM-MM method, the electrostatic energy is expanded to include the MM atoms:

$$E_{es}[\rho] = \tilde{E}_H[\rho] + \tilde{E}_{PS}^{loc}[\rho] + \tilde{E}_{em}[\rho] + \tilde{E}_{im} \quad (7.13)$$

where the four terms on the right hand side represent, respectively from left to right, the Hartree energy, the interaction of the electron density with the local pseudopotential, with

[1] In Car-Parrinello implementations, the Hartree energy is usually expressed as $\tilde{E}_H[\rho_{tot}]$.

[2] As it is shown below, this reformulation is helpful to sum an infinite arrange of charges to compute the total electrostatic energy in periodic boundary conditions

the classical charges, and the Coulomb interaction involving all ions, both QM and MM. In particular, the last two terms of Eq. 7.13 can be written as:

$$\tilde{E}_{em}[\rho] = \int \rho(\mathbf{r}) \left(\sum_{m=1}^{N_m} v_{MM}^m(|\mathbf{r} - \mathbf{R}_I|) d\mathbf{r} - \int \frac{\rho_I(\mathbf{r'})}{|\mathbf{r} - \mathbf{r'}|} \right) d\mathbf{r} \tag{7.14}$$

$$\tilde{E}_{im} = \frac{1}{2} \left(\sum_{I=1}^{T} \sum_{J=1, J\neq I}^{T} \frac{Z_I Z_J}{|\mathbf{R}_I - \mathbf{R}_J|} - \iint \frac{\rho_I(\mathbf{r})\rho_I(\mathbf{r'})}{|\mathbf{r} - \mathbf{r'}|} d\mathbf{r} d\mathbf{r'} \right) \tag{7.15}$$

where m runs over the number of classical atomic species, while N_m and M_m are, respectively, the number of classical species and the number of atoms for the m species. The function v_{MM}^m is the pseudopotential associated with the classical species m, and is defined below. Z_I is the ionic charge of every atom (irrespective of being quantum or classical) and $\mathbf{R}_I$ its location. T denotes the total number of atoms in the system ($T = \sum_s^{N_s} P_s + \sum_m^{N_m} M_m$).

The pseudopotential of the classical atoms, v_{MM}^m, has to verify a few properties: has to be a smooth continuous function to be numerically tractable with Fast Fourier Transforms, has to decay as the inverse of the distance r at long ranges, and must avoid the divergence when $r \to 0$. We have adopted the functional form proposed by Laio et al. [5] for the representation of the QM atoms in a previous QM-MM implementation:

$$v_{MM}^m(|\mathbf{r} - \mathbf{R}_I|) = v_{MM}^m(r) = Z_m \frac{r_{cm}^4 - r^4}{r_{cm}^5 - r^5} \tag{7.16}$$

where m denotes the classical atom species, Z_m its charge, and r_{cm} a cutoff radius associated to every species. This function approaches Z_m/r for $r \gg r_{cm}$, and goes smoothly to Z_m/r_{cm} for $r = 0$. Even if the exact value of v_{MM} at short ranges is not critical, it has to be small enough not to become a trap for the electrons. In the case of plane-wave basis, sharp MM potentials of positive species may cause electronic charge localization on the classical atoms: this is called the *spill out* effect. The possibility of electron density flowing to the MM region can be minimized using a classical pseudopotential which varies softly and has a small magnitude at short distances. The function defined in 7.16 satisfies these conditions, providing at the same time an appropriate interaction between MM and QM atoms.

As discussed in section 2.2.3, the Coulomb energy of a periodic arrange of charges is conditionally convergent: to achieve convergence, the sum is decomposed in three contributions, one of which is computed in the reciprocal space. Analogously to the treatment in 2.2.4, all terms in equation 7.13 can be transformed to Fourier space, and the total electrostatic energy of the QM-MM system can be evaluated as a function of the **G**-vectors:

$$E_{es}[\rho] = \frac{\Omega}{2}\sum_{\mathbf{G}\neq 0}\frac{4\pi}{G^2}\tilde{\rho}_T(\mathbf{G})\tilde{\rho}_T(-\mathbf{G})$$

$$+\Omega\sum_{\mathbf{G}}\sum_{s=1}^{N_s}S_s(\mathbf{G})\tilde{u}_{PS}^{loc,s}(G)\tilde{\rho}(-\mathbf{G}) + \Omega\sum_{\mathbf{G}}\sum_{m=1}^{N_m}S_m(\mathbf{G})\tilde{u}_{MM}^{m}(G)\tilde{\rho}(-\mathbf{G})$$

$$+\frac{1}{2}\sum_{I=1}^{T}\sum_{J\neq 1}^{T}Z_I Z_J\left[\sum_{n=-n_{max}}^{n_{max}}\frac{erfc(|\mathbf{R}_I + nL - \mathbf{R}_J|\eta)}{|\mathbf{R}_I + nL - \mathbf{R}_J|}\right]$$

$$-\frac{\eta}{\sqrt{\pi}}\sum_{I=1}^{T}Z_I^2 \tag{7.17}$$

The first term on the right hand side in 7.17 is the Hartree energy. The second and third terms account for the interaction of quantum nuclei and classical atoms, respectively, with the electronic density. The fourth term represents the electrostatic interactions of all ions with themselves, in the MM and QM regions. The last term arises from the Ewald sum technique and is usually called E_{self}. The structure factors $S_s(\mathbf{G})$ and $S_m(\mathbf{G})$ correspond the QM and MM species, respectively. $\tilde{\rho}_T(\mathbf{G})$ and $\tilde{\rho}(\mathbf{G})$ are the Fourier transforms of the total and electronic densities. The functions $\tilde{u}_{PS}^{loc,s}(G)$ and $\tilde{u}_{MM}^{loc,s}(G)$ are the Fourier transforms of the corresponding pseudopotentials minus the ionic charge contribution: [3]

$$u_{PS}^{loc,s} = v_{PS}^{loc,s}(r) - \frac{Z_s}{r}erf\left(\sqrt{2\eta_s}r\right) \tag{7.18}$$

$$u_{MM}^{m} = v_{MM}^{m}(r) - \frac{Z_m}{r}erf\left(\sqrt{2\eta_m}r\right) \tag{7.19}$$

We note that equations 2.99 and 7.17 are similar, aside from the fact that in 2.99 the $\mathbf{G} = 0$ terms were singled out and written explicitly. In particular, the third term in equation 7.17 does not appear in 2.99, and the sums in the fourth and fifth terms obviously include the MM atoms. As mentioned in section 2.2.4, it turns out that the fast (gaussian) decay of ρ_α implies that the lattice sum running over periodic images up to n_{max}, can be truncated after a small number of terms. Normally, n_{max} does not need to be larger than 1.

Since in the present implementation the MM atoms receive a similar treatment as the QM nuclei, equation 7.6 is not the most natural way to split the total energy. With the exception of the second and third terms in equation 7.17, the rest of the terms included in the electrostatic energy E_{es} carry at the same time the contributions from MM atoms and QM nuclei.

[3] The parameters η_m or η_s determine the width of the Gaussians used to model the ionic charges ρ_α, see equation 2.90.

There is a non-electrostatic contribution to the QM-MM energy, which is represented with a Lennard-Jones potential:

$$E_{LJ,im} = \sum_I \sum_J 4\epsilon_{IJ} \left[\left(\frac{\sigma_{IJ}}{|\mathbf{R}_I - \mathbf{R}_J|} \right)^{12} - \left(\frac{\sigma_{IJ}}{|\mathbf{R}_I - \mathbf{R}_J|} \right)^{6} \right] \tag{7.20}$$

where ϵ_{IJ} and σ_{IJ} are the parameters for the Lennard-Jones interaction of the classical atom I with a quantum atom J. This energy is important to prevent the MM charges of negative sign to collapse on the positive QM nuclei. The Lennard-Jones parameters for the mixed QM-MM interaction is usually set equal to those employed for a pair of classical atoms of the corresponding species. In particular, in the present approach, the values of σ and ϵ for the oxygen-oxygen interaction are not dependent on the QM or MM identity of the oxygen atoms.

Finally, combining all the contributions together, we compute the total energy as:

$$E_{tot}[\rho] = E_{es}[\rho] + T_e[\rho] + E_{XC}[\rho] + E_{PS}^{nl} + E_{LJ,im} + E_{LJ,MM} + E_{b,MM} \tag{7.21}$$

where $E_{LJ,MM}$ considers the Lennard-Jones interactions within the MM region, and $E_{b,MM}$ the bonds between connected MM atoms.

7.2.2 The forces

The atomic forces can be calculated for the QM and for the MM atoms as the derivative of the total energy (equation 7.21) with respect to the ionic positions. In the case of the QM atoms, there is no explicit dependence of $T_e[\rho]$ and $E_{XC}[\rho]$ on R_I, and therefore only three terms survive in the derivative:

$$F_I = -\frac{dE_{tot}}{d\mathbf{R}_I} = -\frac{\partial E_{es}}{\partial \mathbf{R}_I} - \frac{\partial E_{LJ,im}}{\partial \mathbf{R}_I} - \frac{\partial E_{PS}^{nl}}{\partial \mathbf{R}_I} \tag{7.22}$$

The former of these terms on the right hand side above can be developed as:

$$-\frac{\partial E_{es}}{\partial \mathbf{R}_I} = \frac{Z_I}{2} \sum_{J \neq I}^{T} \sum_{n=-n_{max}}^{n_{max}} (\mathbf{R}_I + l - \mathbf{R}_J) \times \left[\frac{erfc(|\mathbf{R}_I + l - \mathbf{R}_J|\eta)}{|\mathbf{R}_I + l - \mathbf{R}_J|^3} + \frac{\eta e^{-\eta^2 |\mathbf{R}_I + l - \mathbf{R}_J|^2}}{|\mathbf{R}_I + l - \mathbf{R}_J|} \right]$$

$$+\Omega \sum_{G \neq 0} i\mathbf{G} e^{i\mathbf{G}\cdot\mathbf{R}_I} (\tilde{u}_{PS}^{loc,s}(G) + \tilde{u}_{MM}^{m}(G)) \tilde{\rho}(-\mathbf{G}) \tag{7.23}$$

where l denotes the cell dimension. On the other hand, the Lennard-Jones contribution to the force is simply:

$$-\frac{\partial E_{LJ}}{\partial \mathbf{R}_I} = 4\epsilon \left[\frac{12\sigma^{12}}{|\mathbf{R}_I - \mathbf{R}_J|^{13}} - \frac{6\sigma^6}{|\mathbf{R}_I - \mathbf{R}_J|^7} \right] \tag{7.24}$$

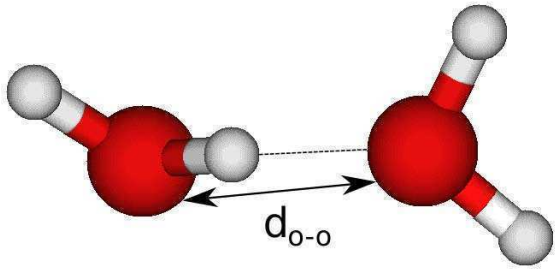

Figure 7.1. Structure of the water dimer close to its energy minimum. The distance between the oxygen atoms is denoted as d_{O-O}.

The contribution originating in the non local part of the pseudopotential energy is part of the standard QM implementation and will not be discussed in the context of this thesis. On the other hand, the expression for the forces on the MM atoms will be similar to that given in equation 7.25, but for the third term and for the derivatives of the pure MM contributions:

$$F_J = -\frac{\partial E_{es}}{\partial \mathbf{R}_J} - \frac{\partial E_{LJ,im}}{\partial \mathbf{R}_J} - \frac{\partial E_{LJ,MM}}{\partial \mathbf{R}_J}\frac{\partial E_{b,MM}}{\partial \mathbf{R}_J} \tag{7.25}$$

7.3 Tests in the water dimer

The potential energy curve of a water dimer, consisting of one water molecule in the QM domain and the other in the MM zone, was calculated to get an assessment of the hybrid QM-MM methodology. The geometry of the dimer was optimized using DFT, and then the binding energy was computed at different separations. It is important to note that there are two inequivalent configurations in which this curve can be obtained, depending on whether the MM molecule plays the role of donor or acceptor of the hydrogen bond. In the water dimer of Figure 7.1, the hydrogen bond donor is the molecule on the left and the acceptor is on the right. Therefore, two curves were obtained. Along these curves, the geometry of the QM water molecule was frozen to the optimized DFT structure, while the geometry of the MM molecule was the one given by the SHAKE algorithm. The energy was scanned along the O-H-O axis as a function of the H-bond distance, or the oxygen-oxygen separation, denoted d_{O-O} in the Figure. The geometry at the minimum is in fair agreement with both theoretical [3, 20, 21] and experimental studies [22, 23]. The curves are compared with those obtained using either the pure QM or the pure MM approaches.

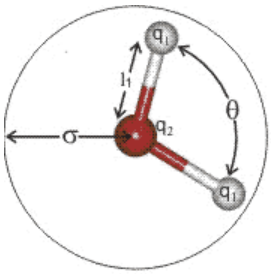

Figure 7.2. The parameters characterizing the SPC water model: the H-O-H angle θ, the O-H bond length I_1, the atomic charges q_1 and q_2, and the Lennard Jones radius σ. Values are given in Table 7.1. Figure taken from reference [27].

Table 7.1. Parameters used in the SPC water model. Data taken from reference [18].

ϵ (Å)	σ (KJ/mol)	I_1(Å)	q_1(e)	q_2(e)	θ°
3.166	0.650	1.000	+0.410	-0.820	109.47

7.3.1 Molecular Mechanics description of water

There are several water models which enable to characterize a water molecule from a classical description. Different models may vary in the functional form of the potentials, and in particular, in the number and the values of the required parameters [18]. Such parameters are adjusted to reproduce different thermodynamical and structural properties of water, typically in its liquid state: liquid density, heat capacity, or radial distribution functions[4] for O-O or O-H pairs [24–26]. Most atomistic force-fields for water have the form of equation 7.1, in which case the Lennard-Jones parameters (ϵ and σ) are needed to get E_{LJ} and the partial charges of hydrogen and oxygen (q_1 and q_2 respectively) are required to compute E_{ele}. Atomistic models for water may be flexible or rigid, and this dictates the form of E_{bond}. We will use a rigid model of water; in these type of models internal degrees of freedom are eliminated, and E_{bond} may be replaced by the specification of the O-H bond length and the H-O-H bond angle, which are kept frozen.

For this preliminary implementation of the QM-MM method we adopt the SPC [24] water model, which is one of the simplest and most used in classical molecular dynamics simulation of liquid H_2O. The parameters characterizing the SPC model are indicated in Figure 7.2 and their values are listed in Table 7.1.[5] The distance I_1 and the angle θ are kept

[4]The radial distribution function, conventionally denoted $g(r)$, represents the atomic density of one kind of atoms as a function of the distance to atoms of another kind.

[5]In our hybrid scheme charges q_1 and q_2 have the opposite sign due to the current convention in which electrons are positive entities.

fixed. To this end the SHAKE algorithm was added to the program [28]. In this procedure, interatomic distances and angles remain fixed along the dynamics through the application of a constraint force acting on top of the MM potential. For example, for the constraint on the bond length between atoms i and j, we have $\sigma_{ij} = (\mathbf{r}_i - \mathbf{r}_j)^2 - d_{ij}^2 = 0$. The associated constraint forces F_{ci} and F_{cj} are:

$$F_{ci} = \lambda \frac{\partial \sigma}{\partial \mathbf{r}_i} \qquad F_{cj} = \lambda \frac{\partial \sigma}{\partial \mathbf{r}_j} = -F_{ci}$$

The incorporation of these forces into the equations of motion perturbe the coordinates of atoms i and j, so that the distance between them remains a constant, without affecting the potential or kinetic energies. The Lagrange multiplier λ is determined from the integration algorithm and the constraint equation [28]. When there is more than one constraint, as in the case of rigid water, then more than one Lagrange multiplier has to be obtained self-consistently. The SHAKE algorithm solves the values of λ iteratively.

7.3.2 Quantum Mechanical setting

We provide here the computational parameters involved in the QM calculations. In order to perform the hybrid QM/MM calculation, some parameters regarding the QM part has to be settled. The O-H-O axis was oriented on the x direction. In principle, a large supercell was employed to minimize the interactions of the water dimer with their periodic images. The cell dimensions, 50×20×20 bohr, are longer on the x axis because this is the direction in which the potential energy is scanned.

The BLYP approach to the DFT exchange-correlation energy [29,30], and norm-conserving pseudopotentials [31] were adopted to compute total energies and forces. The Kohn-Sham orbitals and charge density were expanded in planewaves up to a kinetic energy cutoff of 80 and 360 Ry, respectively[6]. *k*-sampling was restricted to the Γ point.

7.3.3 Interaction energy curves

Before going into the QM-MM calculations, we compare the curves provided by the pure QM and MM methodologies for the water dimer. As already mentioned, the MM curve was calculated with the SPC model, and the QM curve was obtained with DFT using the computational parameters specified above. The results are plotted in Figure 7.3. The difference in the description is readily apparent: the QM curve is shifted to a weaker interaction and a longer distance at the minimum with respect to the MM curve. Reported experimental values of 5.4 ± 0.7 kcal/mol and 2.9 Å [23] for the oxygen-oxygen separation

[6]Notice that the energy cutoff values are more demanding for norm-conserving pseudopotentials than for ultrasoft, where cuttofs of 25 and 200 Ry are typically used.

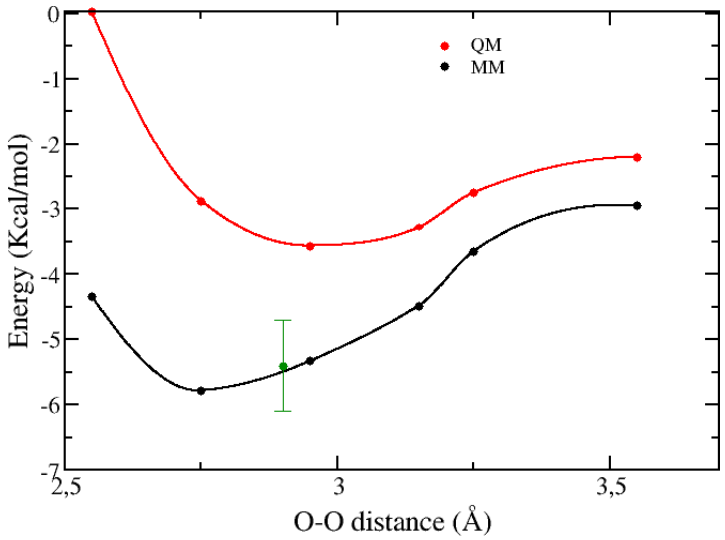

Figure 7.3. Interaction energy for a water dimer as a function of the O-O distance, according to DFT (QM) and SPC (MM) calculations. Experimental value at the minimun is shown in green with its error bar [23].

are better reproduced by the classical model, which provides an hydrogen bond energy of 5.8 kcal/mol at 2.8 Å. This better agreement stems from the fact that the SPC parameters are fitted to reproduce water H-bonding.

On the other hand, the quantum-mechanical water dimer interaction, of 3.6 kcal/mol, is underestimated with respect to experiments. This can be in part ascribed to the well known flaw of density functional theory to describe long-ranged interactions [32], though DFT calculations based on localized basis sets have provided results in better agreement with experimental data [20, 21, 33]. Convergence of the present plane waves calculations with respect to the basis set, pseudopotentials, supercell size,[7] and other computational parameters, has been thoroughly checked. On the other hand, plane waves calculations reported in the past are consistent with our results [34, 35], suggesting that the underestimation of the H-bond energy is somehow related to the PW setting. Together with a weaker interaction, a slightly longer equilibrium distance of around 3.0 Å is obtained.

Since we are tied to the PPW energies, we are limited in the accuracy of the QM-MM description, which will reflect the behavior of the QM and MM Hamiltonians. In fact, the QM-MM potential energy curves, shown in Figure 7.4, turn out to be quite interesting. As discussed above, two configurations can be considered for the hybrid model, depending on the identity of the donor of the H-bond: these curves are depicted together with the results corresponding to the pure SPC and DFT calculations. Examination of the curves leads to

[7] The energy of the system was insensitive to further enlargement of the cell dimensions. We note that the zero energy, corresponding to a non-interacting dimer, was defined at the point of maximum O-O separation, of 25 bohr or 13.23 Å, i.e., one half of the unit cell constant on x.

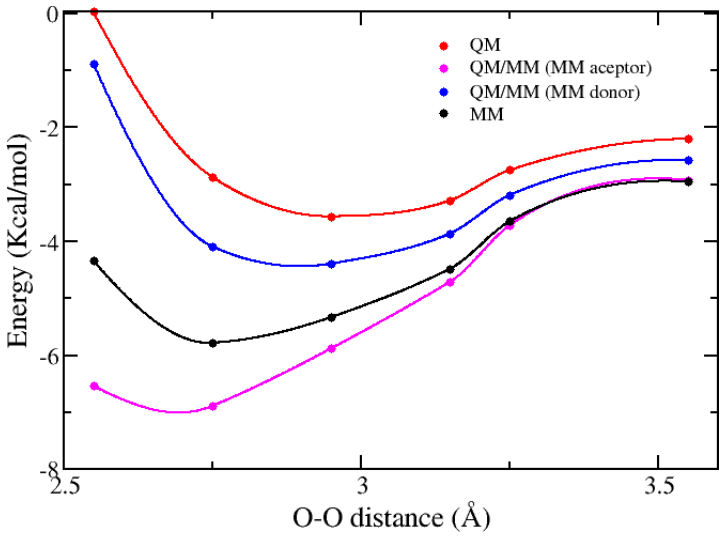

Figure 7.4. Interaction energy for a water dimer as a function of the O-O distance, according to DFT (QM), SPC (MM), and hybrid QM-MM calculations. The QM-MM curves correspond to the MM molecule in the role of H-bond donor and H-bond acceptor.

the following observation: the QM-MM curve in which the acceptor is the MM molecule, roughly reproduces the SPC curve, whereas the QM-MM curve with this molecule in the place of the H-bond donor, is closer to the DFT results. In other words, we conclude that the curves are essentially reflecting the identity of the acceptor. This is a meaningful result, understandable when we recall that most of the charge density involved in the bond, and therefore the polarization effect, corresponds to the oxygen atom. The electron density associated with the H atom is much lower, and there is not a major effect if this electron density is replaced by a bare pseudopotential.

The reason why the hybrid curves have a stronger binding character than their parents QM and MM curves, respectively, is more difficult to explain. In the case of the MM acceptor, both the hybrid and the SPC curves overlap at long distances, but for smaller separations the hybrid dimer is more strongly bound. The polarization of the charge density around the H atom can explain this enhancement of the interaction with respect to the purely classical binding with non-polarizable charges. On the other hand, the second hybrid curve—where the QM water plays the acceptor—follows closely the DFT behavior, but is shifted to more negative energies. The cause for this shift is not evident to us, but might be related to the way the reference energies defining the non-interacting dimers were calculated. Anyway, a fine adjustment of the QM-MM curves can be made through the cutoff radii r_{cm} in equation 7.16. The values employed for the present results are 0.5 bohr and 0.4 bohr for oxygen and hydrogen respectively. A decrease in these radii provokes a weakening of the interaction.

Table 7.2. Atomic forces calculated analytically (F^a) and through finite differences (F^fd), for an atomic displacement on the i-coordinate of 0.01 bohr between the initial and final states. The index i denotes at the same time the component of the force and the direction of the displacement.

Atom type	*r*	Initial F_a	Final F_a	F_n
O_{QM}	x	5.97E-002	5.58E-002	5.8E-002
O_{QM}	y	3.96E-004	-3.71E-003	-1.0E-003
H_{QM}	x	-2.95E-002	-3.12E-002	-3.0E-002
O_{MM}	x	3.71E-002	3.73E-002	3.7E-002
O_{MM}	y	8.87E-002	8.91E-002	8.9E-002
H_{MM}	x	-6.97E-002	-6.88E-002	-6.9E-002

7.3.4 Atomic forces

To test the computation of the forces, we compare the analytical forces implemented in equations 7.23 and 7.24 with the forces F^{fd} obtained from finite differences as:

$$F_{i,I}^{fd} = -\frac{\partial E}{\partial i(I)} = -\frac{E(\mathbf{R}_I + \Delta i) - E(\mathbf{R}_I)}{\Delta i} \tag{7.26}$$

where i refers to any of the three directions, x, y or z, $F_{i,I}^{fd}$ denotes the i-component of the force on atom I, E is the total energy, and Δi is an atomic displacement applied to the i-coordinate of atom I. The agreement between the finite difference approximation and the values coming from the analytical expressions 7.23 and 7.24 prove the consistency between energy and forces. The results of these tests are included in Table 7.2, where the value of $F_{i,I}^{fd}$ is shown together with the forces analytically obtained at $\mathbf{R}_I$ (initial state) and at $\mathbf{R}_I + \Delta i$ (final state).

As expected, the finite difference forces always fall in between the two analytical results F^a. The values of the last column in Table 7.2 were calculated as differences between two close energies and were treated with a lower numerical precision. The apparent disagreement in the values of the second row (y-component of the force on O_{QM}) is simply because of their very low magnitudes, close to zero. Yet, F^fd is comprised between the forces obtained for the initial and final states. The z-components of the forces were also of a low magnitude and are not shown.

This preliminarly analysis supports the consistency of energies and forces. A more stringent test would require to monitor the total energy conservation during long enough molecular dynamics simulations in the microcanonical ensemble, for which the Verlet algorithm needs to be implemented. This remains for the next stage of this development.

7.4 Final comments

Evidently, the disagreement between the two QM-MM curves in Figure 7.4 is not a desirable effect. However, we can not expect a much better agreement given the current discrepancy between the DFT and SPC energies. This exceeds the domains of the QM-MM formulation, however, the exploration of alternative forces-fields with behaviors closer to the one exhibited by DFT must lead to a partial reconciliation between the two QM-MM curves. Water models with more than three centers to represent the electrostatic interactions (e.g. TIP4P [18] or TIP5P [26]), in which the charges are spatially less localized, are candidates to be better partners of the quantum-mechanical potential. The possibility of reparametrizing any of these existing models is also envisioned.

One of the central conclusions we draw from this study is that the simple idea of representing the classical atoms in the same way as the pseudoions of the PPW approach, turns out to be a viable strategy toward a QM-MM model. The empirical pseudopotentials of equation 7.16 are another ingredient which could be tuned to fit the experimental curves. In any case, the present pseudopotential functions have proved appropriate to reproduce the MM or the QM behavior in each hybrid configuration, exhibiting no evidence of spill-out effect (this was confirmed through the integration of the electron charge density around the classical hydrogen atoms).

This implementation of the QM-MM hybrid methodology inside the Quantum Espresso code, allows us to combine both levels of atomic description with the purpose of accelerating future PBC calculations and extending the size of the affordable systems. In particular, our objective is the representation of solid-liquid interfaces through an all-atom technique computationally less demanding than pure DFT treatments. Yet another interesting range of applications would involve chemical connectivity between the QM and the MM subsystems. In this case the frontier between the QM and MM regions would be inside the material, allowing for example a QM description of the surface atoms (interacting with an adsorbate) and a molecular mechanics treatment of the rest of the slab. The same kind of approach would be also useful to address amorphous materials in periodic boundary conditions. To this end, a model to represent a covalent bond between a classical and a quantum atom should be implemented. The link-atom method [36, 37] is typically used to represent QM-MM bonds in molecular systems. To the best of our knowledge, however, no equivalent approach has been developed for bonds in solids, and is therefore a future challenge to be addressed at an advanced stage of the present development.

References

[1] T. Laino, F. Mohamed, A. Laio, and M. Parrinello, *J. Chem. Theory Comput.* 1, (2005), 1176–1184.

[2] J. Gao and C. Alhambra, *J. Chem. Phys.* 107, (1997), 1212.

[3] M. D. Elola, D. A. Estrin, and D. Laria, *J. Phys. Chem. A* 103, (1999), 5105.

[4] D. A. Yarne, M. E. Tuckerman, and G. J. Martyna, *J. Chem. Phys.* 115, (2001), 3531.

[5] A. Laio, J. VandeVondele, and U. Rothlisberger, *J. Chem. Phys.* 116, (2002), 6941.

[6] A. Crespo, D. A. Scherlis, M. A. Marti, P. Ordejón, A. E. Roitberg, and D. A. Estrin, *J. Phys. Chem. B* 107, (2003), 13728.

[7] V. M. Sánchez, A. Crespo, J. S. Gutkind, and A. G. Turjanski, *J. Phys. Chem. B* 110, (2006), 18052.

[8] D. Rinaldo, D. M. Philipp, S. J. Lippard, , and R. A. Friesner, *J. Am. Chem. Soc.* 129, (2007), 3135–3147.

[9] L. Capece, D. A. Estrin, and M. A. Marti, *Biochemistry* 47, (2008), 9416–9427.

[10] C. Bongards and W. Gärtner, *Acc. Chem. Res.* 43, (2010), 485–495.

[11] H. Lin and D. G. Truhlar, *J. Phys. Chem. A* 109, (2005), 3991–4004.

[12] M.-H. Du, A. Kolchin, and H.-P. Cheng, *J. Chem. Phys.* 119, (2003), 6418.

[13] M. L. Sushko, P. V. Sushko, I. V. Abarenkov, and A. L. Shluger, *J Comput Chem* in press.

[14] D. Ellis and O. Warschkow, *Coord. Chem. Rev.* 238-239, (2003), 31–53.

[15] M. C. G. Lebrero, L. L. Perissinotti, and D. A. Estrin, *J. Phys. Chem. A,* 109, (2005), 9598–9604.

[16] M. C. G. Lebrero and D. A. Estrin, *J. Chem. Theory Comput.* 3, (2007), 1405–1411.

[17] T. Laino, F. Mohamed, A. Laio, and M. Parrinello, *J. Chem. Theory Comput.* 2, (2006), 1370–1378.

[18] A. Leach, *Molecular Modelling: Principles and Applications*, Pearson Education Limited (**1999**).

[19] P. Giannozzi, S. Baroni, N. Bonini, M. Calandra, R. Car, C. Cavazzoni, D. Ceresoli, G. L. Chiarotti, M. Cococcioni, I. Dabo, A. D. Corso, S. de Gironcoli, S. Fabris, G. Fratesi, R. Gebauer, U. Gerstmann, C. Gougoussis, A. Kokalj, M. Lazzeri, L. Martin-Samos, N. Marzari, F. Mauri, R. Mazzarello, S. Paolini, A. Pasquarello, L. Paulatto, C. Sbraccia, S. Scandolo, G. Sclauzero, A. P. Seitsonen, A. Smogunov, P. Umari, and R. M. Wentzcovitch, *J. Phys.: Condens. Matter* 21, (2009), 395502.

[20] A. Famulari, M. Raimondi, M. Sironi, and E. Gianinetti, *Chem. Phys.* 232, (1998), 275.

[21] P. Haynes, C.-K. Skylaris, A. A. Mostofi, and M. C. Payne, *Chem. Phys. Lett.* 422, (2006), 345.

[22] T. R. Dyke, K. M. Mack, and J. S. Muenter, *J. Chem. Phys.* 66, (1977), 498.

[23] J. A. Odutola and T. R. Dyke, *J. Chem. Phys.* 72, (1980), 5062.

[24] Berendsen, h. j. c.; postma, j. p. m.; van gunsteren, w. f.; hermans, j. in intermolecular forces; pullmann, b., ed.; reidel: Dordrecht, 1981; p 331.

[25] H. J. C. Berendsen, J. R. Grigera, and T. P. Straatsma, *J. Phys. Chem.* 91, (1987), 6269.

[26] M. W. Mahoney and W. L. Jorgensen, *J. Chem. Phys.* 112, (2000), 8910.

[27] www.lsbu.ac.uk/water/models.html.

[28] J. P. C. Ryckaert and H. J. C. Berendsen, *J. Comput. Phys.* 23, (1977), 327–341.

[29] A. D. Becke, *Phys. Rev. B* 38, (1988), 3098.

[30] C. Lee, W. Yang, and R. G. Parr, *Phys. Rev. B* 37, (1988), 785.

[31] N. Troullier and J. L. Martins, *Phys. Rev. B* 43, (1991), 1993–2006.

[32] J. Kohanoff, *Electronic Structure Calculations for Solids and Molecules - Theory and computational methods*, Cambridge University Press (**2006**).

[33] M. W. Feyereisen, D. Feller, and D. A. Dixon, *J. Phys. Chem.* 100, (1996), 2993.

[34] P. H.-L. Sit and N. Marzari, *J. Chem. Phys.* 122, (2005), 204510.

[35] T. Todorova, A. P. Seitsonen, J. Hutter, W. I.-F. Kuo, and C. J. Mundy, *J. Phys. Chem. B.* 110, (2006), 3685.

[36] G. M. Monard and J. K. M. Merz, *Jr., Acc. Chem. Res.* 32, (1999), 904.

[37] M. Eichinger, P. Tavan, J. Hutter, and M. Parrinello, *J. Chem. Phys.* 110, (1999), 10452.

Chapter 8

Conclusions and Prospects

Along this thesis we have studied both the solid-gas and solid-liquid interfaces of inorganic oxides. In the former case, combination of the Umbrella Sampling technique with Car-Parrinello molecular dynamics simulation enabled to determine the dissociation free energy profiles for small molecules upon titanium dioxide clean surfaces. To the best of our knowledge, this is the first example of the application of a biased statistical sampling method to study the dissociation on surfaces at finite temperatures. Reaction and activation free energies are the most relevant thermodynamic variables involved in chemical processes at constant temperature, because they determine the equilibrium and the kinetic parameters ruling the reaction. At the same time, they are not trivially accessible by computer simulation, nor by experiments, and so they are seldom reported in the literature. Our calculations do not only provide an estimate for the values of the kinetic barriers and the reaction free energies for key processes in TiO_2 surface chemistry: they also tell us, thanks to the computation of the dissociation entropies, to what extent the energies obtained at 0 K are a measure of the stability at room temperature, which is a widespread assumption in computational surface chemistry.

One of the main drawbacks of the Umbrella Sampling method is the need to provide the reaction coordinate in advance, which could be a difficult task for processes of greater complexity than those studied here. In those cases, the employment of this technique in combination with the NEB method [1] could be an interesting strategy to investigate catalytic reactions. In this framework, the NEB method could be used to determine the most suitable reaction coordinates before performing the statistical sampling, extracting at the same time the internal and free energy profiles for a given reaction. In particular, among the possible processes that could be investigated with this scheme, a very appealing direction would be the determination of the PZC (point of zero charge) of oxide surfaces, by studying the dissociation of water at the solid-liquid interface. To realize this at a feasible computational cost, we envision the combination of Umbrella Sampling with either

[1] NEB denotes the Nudgest Elastic Band method, an algorithm to explore the pathways between products and reactants in order to compute internal energy profiles [1, 2]

the hybrid QM-MM methodology or the continuum solvent model devised in this thesis to represent the solution.

A successfull collaboration with an experimental group has shown how simulations can complement and allow for the interpretation of spectroscopic data. While in this case the data came from XPS measurements, the results from gas phase PPW-DFT calculations often admit direct comparison against surface microscopies and spectroscopies providing atomistic detail, such as STM, AFM, EXAFS or NEXAFS [3]. On the other hand, the development of a continuun solvent model in periodic boundary conditions based on DFT and the Car-Parrinello scheme, brings closer the possibility of studying reactivity at solid-liquid interfaces. Using this method, we examined the adsorption of small molecules on titania surfaces through total energy calculations. Our results were in close agreement with more expensive calculations in which the solvent was explicitly included, every time these calculations were available, as in the work by Langel et al. on the adsorption of organic species [4], or by Cheng and Selloni about the chemistry of the hydroxide ions at the water-anatase interface [5].

One of the most interesting features of the continuum solvent model developed in this thesis is the possibility of performing molecular dynamics simulations at the solid-liquid interface. This possibility has not been fully explored in this thesis mainly because of the unavailability of a parallel version of the multigrid computer code implemented to solve the Poisson equation. Today, most state of the art simulations from first-principles in materials science are carried out in multiprocessor architectures which allow for the treatment of larger system over longer times. Work is in progress in this direction to have a paralell multigrid algorithm. In particular, as mentioned above, the potential to perform long molecular dynamics within the continuum solvent model would allow, in combination with the Umbrella Sampling technique, to determine in an accurate way the PZC of oxide surfaces: in the last two or three years, a small number of studies attempting to recover this important property from ab-initio calculations have been reported [6, 7]. PZC values can be measured experimentally in a variety of ways such as potentiometric titration, or through electrokinetic and electroacustic methods [8]. All these provide results which are averages on the different exposed faces of the material; in contrast, simulations can provide information concerning a specific surface. Empirical models exist for the estimation of the PZC of oxides, the MUSIC [2] model [9, 10] being among the most employed in materials chemistry. The applicability of this and other models relies on a large amount of parameters. Different studies have sought to use DFT calculations to improve the MUSIC parameters [11–14], but the possibility of realizing calculations in contact with the liquid phase opens the way to PZC estimations based fully on first-principles [7], without the aid

[2]MUSIC denotes MULtiSIte Complexation empirical model

of empirical models. In this line, we have already started a study of the PZC of silica and titania surfaces, based on the computation of dissociation energies in the presence of the continuum solvent.

Finally, we have invested a lot of effort in the first stage toward the implementation of a hybrid QM-MM technique for extended systems. For now, only the MM-parameters corresponding to water have been incorporated. For this methodology to be used in surface chemistry simulations, a second stage of parametrization must be carried out to include the water-surface interaction potentials. Even though not in its final stage, the model presented so far is, to the best of our knlowledge, the first QM-MM scheme implemented with Ewald sums in periodic boundary conditions. Our hope is this methodology will open the path to study the surface chemistry of defects as well as nanostructured surfaces exhibing terraces and hinks. Moreover, the same method can be adapted to include discrete or continuous distributions of charge which could be used to represent an electric field in the simulations, with the ultimate goal of describing an electrode embedded in an MM liquid phase. This would allow for molecular dynamics simulations of electrochemical processes, which is today one of the most appealing challenges in the field of first-principles simulations in chemistry and materials science.

Above all, one of the main objectives of this thesis—which we believe was accomplished—was to set up the basis for the computational study of solid-liquid interfaces, as the starting point from where to continue working.

References

[1] G. Mills, H. Jnsson, and G. K. Schenter, *Surf. Sci.* 324, (1995), 305.

[2] G. Henkelman, B. P. Uberuaga, and H. Jnsson, *J. Chem. Phys.* 113, (2000), 9901.

[3] J. C. Vickerman, *Surface Analysis - The principal Techniques*, John Wiley & Sons (**2005**).

[4] S. Köppen and W. Langel, *Phys. Chem. Chem. Phys.* 10, (2008), 1907.

[5] H. Cheng and A. Selloni, *Langmuir* 26, (2010), 11518.

[6] M. L. Machesky, M. Pedota, D. J. Wesolowski, L. Vlcek, P. T. Cummings, J. Rosenqvist, M. K. Ridley, J. D. Kubicki, A. V. Bandura, N. Kumar, and J. O. Sofo, *Langmuir* 24, (2008), 12331.

[7] J. Cheng and M. Sprik, *J. Chem. Theory Comput.* 6, (2010), 880–889.

[8] M. Kosmulski, *J. Colloid Interface Sci.* 253, (2002), 77.

[9] T. Hiemstra, P. Venema, and W. H. Van Riemsdijk, *J. Colloid Interface Sci.* 184, (1996), 680.

[10] J.-P. Jolivet, *Metal Oxide Chemistry and Synthesis*, John Wiley & Sons (**2000**).

[11] P. Zarzycki, *J. Phys. Chem. C* 111, (2007), 7692–7703.

[12] Z. Zhang, P. Fenter, L. Cheng, N. C. Sturchio, M. J. Bedzyk, M. Předota, A. V. Bandura, J. D. Kubicki, S. N. Lvov, P. T. Cummings, A. A. Chialvo, M. K. Ridley, P. Benezeth, L. Anovitz, D. A. Palmer, and M. L. Machesky, *Langmuir* 20, (2004), 4954–4969.

[13] J. P. Fitts, M. L. Machesky, D. J. Wesolowski, X. Shang, J. D. Kubicki, G. W. Flynn, T. F. Heinz, and K. B. Eisenthal, *Chem. Phys. Lett.* 411, (2005), 399–403.

[14] P. Nortier, A. P. Borosky, and M. Allavena, *J. Phys. Chem. B* 101, (1997), 1347–1354.

Acknowledgments/Agradecimientos

Agradezco primeramente al CONICET por haberme otorgado la beca doctoral con la que he podido hacer esta tesis, al INQUIMAE y DQIAyQF-FCEN-UBA por haberme dado el lugar de trabajo y en el último caso también la formación de posgrado y brindarme la posibilidad de dar clases. Quiero agradecer a los profesores que han contribuido a mi formación académica proveyendo no sólo las asignaturas impartidas sino tamién un carácter crítico que hizo posible que me presentara al doctorado en primer lugar y luego que lo haya podido terminar.

Dentro de ellos quiero agradecer y manifestar mi profundo aprecio por Dr. Darío Estrín que desde 2003 a esta parte ha sido siempre un buen apoyo y consejero. Al Dr. Ernesto Marceca por tener el placer de haber dado clases en su turno teórico y seguir aprendiendo en el proceso de dar clases, en esto último quiero también agradecer a los alumnos que han transitado todos estos años y que enseñandoles he aprendido mucho. A los ayudantes y jefes con los que he compartido turnos y he pasado buenos momentos.

A Adrián Turjansky y Ale Crespo, con quienes he hecho mis primeros pasos en lo que entendemos como ciencia.

A Damián Scherlis quien ha hecho que esto fuera posible, con su tenecidad y confianza ha logrado confiar en mi en momentos en que yo no lo lo habría hecho. Por enseñarme todo lo que aprendí en este doctorado, y por ser un buen consejero, quisiera manifestar mi mayor agradecimiento y aprecio hacia él.

A Julie, Nano, Mariela, Galo, Aleka, Williams que con su colaboración han hecho posible que varios temas de esta tesis fueran resueltos o hasta propuestos. A Galo le agredezco también haber sido mi consejero de estudios durante estos años.

A Carlos Sanz y Pablo Ordejón por darme la posibilidad de aprender sobre implementación de metodología en el tiempo que he podido compartir en el ICMAB.

A Ezequiel, quien a participado de parte de cálculos de esta tesis y ha sido un compañero de tesis excepcional, dando siempre su apoyo y tranquilidad.

A las personas del grupo de simulación de la facultad: Marce, Santi, Leo, Lula, Tefi, Pau, Diego M., Charly, Diego G., Damián Bikiel, Laura, Pablo y otras personas que han transitado por el grupo en todos estos años. En especial a Damián B. con quien he compartido muy buenas charlas, a Pau quien nos ha cocinado paellas inolvidables y a Tefi con quien he tenido el gusto de estudiar y compartir muchas cosas. Y muy en especial a Lula, con quien he empezado a estudiar en la universidad y que ha estado siempre desde entonces conmigo, en las buenas y en las malas; va a ser muy raro ahora empezar en otro lado y no poder contar con ella.

A Matias quien siendo el system manager del grupo ha contribuido a que esto pudiera suceder.

A mis amigas de la facultad: a Vero por su eterna alegría, a Estefi por su gran caracter, a Paula por sus pilas, a Jori por su buen ánimo y su incondicional compañía, a Bren con quien hemos “chocado”varias veces haciendo de ésto siempre una aún más fuerte amistad. A Viky, con quien compartimos muchos sueños y miedos, y con la que siempre he podido contar...aunque ahora se este volviendo a Neuquén.

A Juan y a Cari por los momentos compartidos.

A la gente de tango, por los bailes compartidos, en especial a Martín y Edu.

Muy en especial a mis amigos del secundario que han estado siempre conmigo y han hecho que los momentos más difíciles de mi vida hayan pasado como “algo más ”: Ale, Leo, Jime, Palo, Pablo, Flor y Andrés. A Jime particularmente, que siendo mi “compañera de aventuras”ha sido una gran compañera todos estos años. A Ale, Leo y Palo que en estos últimos años han sido de mucha ayuda.

A mis profes de gimnasia que durante todos estos años me han demostrado que los límites no son tales: Marijó, Silvana y Andrea. En especial a Marijó, a quien la conozco desde la infancia y gracias a su tenacidad he alcanzado logros inesperados.

A mi familia por haber estado siempre, dandome ánimos y apoyando todo lo que he hecho en mi vida. A mi padre por enseñarme a aceptar ciertas cosas de la vida y a mi madre por enseñarme a luchar porque algunas otras cosas cambien. A mi hermano por haberme defendido siempre, ser mi confesor en muchas oportunidades y saber que puedo contar con él.

En fin, a todos los que de una forma u otra han contribuido a mi persona haciendo posible este momento. ¡¡¡Gracias!!!